

DEVELOPMENT OF ZNTE:CU CONTACTED CDTE SOLAR CELLS

by

Jiaojiao Li

Copyright by Jiaojiao Li 2016
All Rights Reserved

A thesis submitted to the Faculty and the Board of Trustees of the Colorado School of Mines in partial fulfillment of the requirements for the degree of Doctor of Philosophy (Materials Science).

Golden, Colorado

Date _____

Signed: _____
Jiaojiao Li

Signed: _____
Dr. Colin A. Wolden
Thesis Advisor

Golden, Colorado

Date _____

Signed: _____
Dr. Ryan O'Hayre
Professor and Head
Materials Science Program

ABSTRACT

With an ideal band gap about 1.45 eV and a large absorption coefficient ($>10^4 \text{ cm}^{-1}$) CdTe has emerged as the leading thin film photovoltaic (PV) technology. However an ongoing challenge is forming a high quality ohmic contact with CdTe, which reflects its low carrier concentration and high work function (5.7 eV). To overcome this problem, ZnTe is used as the buffer layer because it has good valence band alignment with CdTe and can be easily doped to form a quasi-ohmic contact. Copper is commonly used to degenerately dope this layer, which narrows the barrier width and permits electron tunneling, creating a quasi-ohmic contact. But excessive copper causes recombination and degradation. With copper having both positive and deleterious effects it is critical to precisely control both its amount and spatial distribution in order to obtain high efficiency.

To achieve that, we developed a rapid thermal processing-based process for back contact preparation that de-couples Cu deposition from its re-distribution. The ZnTe:Cu back contact is co-evaporated at low temperature, with little or no interdiffusion. The sample is then subjected to short RTP treatments to activate the junction. RTP was demonstrated as a highly effective approach for reducing back contact barriers in CdTe solar cells contacted with ZnTe:Cu buffer layers, substantially improving both FF ($>73\%$) and V_{OC} ($>850\text{mV}$). It was also successfully deployed on many platforms. We applied our back contact on the CdTe provided by different groups and made by different methods and got an NREL-certified 16.4% flexible CdTe solar cell (current world record for flexible devices). This process has been demonstrated to be beneficial on multiple device structures, as the low thermal budget of RTP facilitates its adoption without impacting the optimization of upstream processing.

Further characterizations including the high resolution transmission electron microscopy (HR-TEM) and atom probe tomography (APT) were used to study the evolution of the back contact region during RTP treatment. After activation, the ZnTe layer, initially nanocrystalline and homogenous, transforms into a bilayer structure. Copper, co-evaporated uniformly within ZnTe, is found to dramatically segregate and aggregate after RTP. Analysis of TEM images revealed that Zn accumulates at the edge of these clusters, and three-dimensional APT images

confirmed that these are core-shell nanostructures consisting of $\text{Cu}_{1.4}\text{Te}$ clusters encased in Zn. These changes in morphology and composition are related to cell performance and stability.

Au is commonly used as the metallization layer in research labs because of its high work function (5.2 eV), stability in air and, ease of deposition. But Au is not compatible with industrial manufacturing because of its high price so in this work we explore chromium and titanium as practical alternatives. It was found that comparable performance could be obtained with each metal, but that the optimal Cu loading scaled as one would expect based on solubility. Comparisons of J-V and QE behavior among devices produced with insufficient, optimal, and excess Cu dosing are used to provide insight into the role(s) of this critical impurity for device performance. Reliability tests were taken under different stressing conditions to further understand the role of the metallization layers.

In addition to the back contact, front contact is also very important to CdTe solar cells. CdS is widely used as the n-type heterojunction partner for CdTe because of their compatibility. However, CdS is not an ideal window layer for CdTe solar cells. Oxygenated cadmium sulfide ($\text{CdS}:\text{O}$) is found delivering improved blue response relative to CdS. Our recent study revealed that $\text{CdS}:\text{O}$ completely transforms into a layer containing cadmium sulfate clusters interspersed among $\text{CdS}_{1-y}\text{Te}_y$ nanocrystals during device fabrication. This motivated us to study CdTe solar cells employing pre-formed $\text{CdS}_{1-y}\text{Te}_y$ alloy windows without sulfate present. The intrinsic properties of alloys deposited by co-evaporation are evaluated and then used in place of CdS in standard device fabrication. Interestingly we find that device efficiency is nominally unchanged, but there are significant tradeoffs between current collection, fill factor, and open circuit voltage with alloy composition.

TABLE OF CONTENTS

ABSTRACT.....	iii
LIST OF FIGURES	ix
LIST OF TABLES	xii
LIST OF SYMBOLS	xiii
ACKNOWLEDGEMENTS.....	xv
CHAPTER 1 INTRODUCTION	1
1.1 Renewable Energy	1
1.2 CdTe Solar Cell Structure	3
1.3 J-V Parameters.....	10
1.4 Current State of CdTe Solar Cells	11
1.5 Outline of Thesis Goals	13
CHAPTER 2 MATERIALS AND METHODS	16
2.1 Thin Film Deposition Systems	16
2.1.1 Thermal Evaporation	16
2.1.2 Vapor Transport Deposition.....	19
2.1.3 Radio Frequency Magnetron Sputtering.....	20
2.1.4 Tube Furnace vs Rapid Thermal Processing.....	22
2.2 Baseline Solar Cell Fabrication	24
2.3 Thin-Film Characterization Methods	25
2.3.1 Current-Voltage Measurement.....	25
2.3.2 External Quantum Efficiency (EQE).....	27
2.3.3 Time Resolved Photoluminescence	29
2.3.4 Secondary Ion Mass Spectrometry	30
2.3.5 Atom Probe Tomography	31
2.3.6 Ultraviolet-Visible-Near Infrared spectroscopy	32
2.3.7 X-Ray Diffraction.....	34
2.3.8 Scanning Electron Microscope.....	36
CHAPTER 3 RAPID THERMAL PROCESSING OF ZNTE:CU CONTACTED CDTE	

	SOLAR CELLS	39
3.1	Introduction.....	39
3.2	Experimental.....	41
3.3	Results and Discussion	43
3.4	Conclusion	48
CHAPTER 4	HIGH-EFFICIENCY, FLEXIBLE CDTE SOLAR CELLS ON ULTRA-THIN GLASS SUBSTRATE	49
4.1	Introduction.....	49
4.2	Materials and Methods	50
4.3	Results and Discussion	51
4.4	Summary and Conclusions	56
CHAPTER 5	CONTROLLED ACTIVATION OF ZNTE:CU CONTACTED CDTE SOLAR CELLS USING RAPID THERMAL PROCESSING	57
5.1	Introduction.....	57
5.2	Materials and Methods	59
	5.2.1 Device Fabrication.....	59
	5.2.2 Device Characterization	59
5.3	Results	60
	5.3.1 Opto-electronic Properties	60
	5.3.2 Copper Distribution	64
	5.3.2.1 Secondary Ion Mass Spectrometry.....	64
	5.3.2.2 Atom Probe Tomography	66
5.4	Discussion.....	69
5.5	Conclusions	70
CHAPTER 6	THE ROLES OF ZNTE BUFFER LAYERS ON CDTE SOLAR CELL PERFORMANCE.....	72
6.1	Introduction.....	72
6.2	Materials and Methods	73
	6.2.1 Device Fabrication.....	73
	6.2.2 Device Performance	74
	6.2.3 Nanoscale Characterization	76

6.3	Results	76
6.3.1	High Resolution Transmission Electron Microscopy	76
6.3.1.1	Microstructure and Morphology	76
6.3.1.2	Back Contact Composition.....	78
6.3.2	Atom Probe Tomography	82
6.4	Discussion.....	84
6.5	Conclusions	85
CHAPTER 7	THE IMPACT OF DIFFERENT METALLIZATION LAYERS ON CDTE SOLAR CELLS CONTACTED WITH ZNTE:CU BUFFER LAYERS	87
7.1	Introduction.....	87
7.2	Materials and Methods	88
7.3	Results	89
7.3.1	Device Performance Analysis.....	89
7.3.2	Reliability Tests	93
7.4	Summary and Conclusions	97
CHAPTER 8	CDTE SOLAR CELLS EMPLOYING $CdS_{1-y}Te_y$ WINDOW LAYERS..	98
8.1	Introduction.....	98
8.2	Materials and Methods	99
8.3	Results and Discussion	100
8.4	Summary and Conclusions	105
CHAPTER 9	SUMMARY OF RESULTS AND RECOMMENDATIONS FOR FUTURE WORK.....	106
9.1	Summary of Results.....	106
9.1.1	Development of the RTP Treatments.....	106
9.1.2	Study of the Back Contact	107
9.1.3	Metallization Materials and Reliability Tests	107
9.1.4	$CdS_{1-y}Te_y$ Alloy Window Layers	108
9.2	Recommendations for Future Work.....	108
9.2.1	HRT with Alloy Window Layers	109
9.2.2	MgZnO as the Window Layer	109

9.2.3	Ternary Alloys as the Absorber.....	110
9.2.4	Back Contact without Cu.....	110
REFERENCES CITED.....		112
APPENDIX A	SECONDARY AUTHOR CONTRIBUTIONS.....	127
APPENDIX B	PERMISSIONS	128
B.1	Permission from Elsevier	128
B.2	Permission from Elsevier	129
B.3	Permission from IEEE	130

LIST OF FIGURES

Figure 1-1	NREL best research-cell efficiencies	2
Figure 1-2	Shockley–Queisser limit	3
Figure 1-3	The configuration of superstrate CdTe solar cells.....	4
Figure 1-4	a) A configuration of the VTD system b) CSS deposition system	6
Figure 1-5	A photograph of our CdCl ₂ treatment geometry	7
Figure 1-6	A representative J-V curve of a CdTe solar cell.....	10
Figure 2-1	The configuration of the thermal evaporation system.....	17
Figure 2-2	The configuration of the diffusion pump	19
Figure 2-3	A photo of the VTD system	20
Figure 2-4	Sputtering process.	21
Figure 2-5	Magnetron sputtering.	21
Figure 2-6	a) A photograph of the tube furnace b) A photograph of the RTP furnace while heating.	23
Figure 2-7	Configuration of RTP treatment and the baseline device architecture.....	24
Figure 2-8	Spectrum of the radiation outside the earth’s atmosphere compared to spectrum of a 5800 K blackbody	25
Figure 2-9	An equivalent circuit model of a solar cell	26
Figure 2-10	Eternal quantum efficiency system setup.....	27
Figure 2-11	Optical configuration of a monochromator	28
Figure 2-12	QE curves of our samples	29
Figure 2-13	Schematic view of the TRPL setup	30
Figure 2-14	Schematic view of SIMS setup	31
Figure 2-15	Schematic diagram of APT	32
Figure 2-16	Schematic diagram of UV-VIS-NIR.....	33
Figure 2-17	Bragg’s law	35
Figure 2-18	Geometry of the X-ray diffractometer	36
Figure 2-19	Basic SEM setup and its electron path.....	37
Figure 3-1	Configuration of RTP treatment and device architecture.....	41
Figure 3-2	Calibration plot of glass temperature recorded from devices deposited both TEC15 and Corning 7059 after 30 s RTP treatments at the thermocouple temperature.....	42
Figure 3-3	Post-RTP device efficiency as a function of Cu thickness.....	43

Figure 3-4	Device efficiency before and after RTP for 3 different ZnTe:Cu buffer layer configurations.....	44
Figure 3-5	Device efficiency before and after RTP as a function of ZnTe:Cu buffer layer thickness	44
Figure 3-6	Device efficiency during sequential RTP treatments with different temperature steps. (a) 200 - 450 °C using 50 °C increments; (b) 300 - 360 °C using 20 °C increments; (c) 320 - 350 °C using 10 °C increments.....	46
Figure 3-7	J-V curves of devices with different RTP treatments	47
Figure 4-1	NREL-certified 16.4% flexible CdTe solar cell on Willow glass	51
Figure 4-2	Comparison of absolute QE measurements of the 14.05% device and the 16.4% device	52
Figure 4-3	Acceptor density profiles extracted from the C-V data for the devices with evaporated ZnTe:Cu and sputtered ZnTe:Cu back contacts	53
Figure 4-4	a) Simulation of J-V curves with increased carrier density. b) Comparison of certified devices with SCAPS simulations	55
Figure 5-1	Influence of RTP treatment on a) device efficiency as shown in a box plots based on 8-10 devices at each condition; b) J-V curves representative of ZnTe:Cu contacted devices in the as-deposited state, after optimal RTP treatment, and overheated	61
Figure 5-2	Comparison of external quantum efficiency spectra for the 3 representative devices.....	62
Figure 5-3	a) Net acceptor density, NA vs. depletion width, W, as derived from C-V measurements for the as-deposited device and after optimal RTP treatment; b) Comparison of TRPL measurements of minority carrier lifetime from three representative devices	63
Figure 5-4	Quantified SIMS depth profiles of Cu concentration from the Au/ZnTe:Cu/CdTe/CdS devices considered in this work	65
Figure 5-5	TEM images of samples before APT processing, 2D images of the resulting elemental reconstruction, and 1D volume averaged concentration profiles of the back contact region obtained from a) the as-deposited; b) optimally-processed and c) the overheated samples	67
Figure 5-6	Postulated band diagrams of the back contact region for these devices in the a) as-deposited state; b) after application of an optimized RTP treatment.....	70
Figure 6-1	Schematic cross-section of the device structures considered in this work. NREL absorbers were deposited by CSS at 600 °C while CSM absorbers were deposited by VTD at 450 °C	74
Figure 6-2	Evolution of J-V performance as a function of RTP treatment temperature for devices employing a) CSM VTD CdTe and b) NREL CSS CdTe.....	75
Figure 6-3	HAADF image (left) and a bright field TEM image (right) of the back contact region before (left) and after (right) RTP treatment	77

Figure 6-4	High resolution TEM of the CdTe ZnTe interfacial region after RTP activation and selected area diffraction images taken from both layers.....	78
Figure 6-5	TEM images and elemental mapping of the back contact region before and after optimal RTP treatment	79
Figure 6-6	a) TEM image of the back contact region after RTP and 1D elemental profiles through the highlighted regions that include b) a defect-free region, c) a region with a defect in the ZnTe layer, and d) a region that passes through a Cu _x Te inclusion in the CdTe layer	80
Figure 6-7	Elemental composition profile across CdTe grain boundaries at the positions indicated in Figure 6-3. Profile a) crosses the small Cu _x Te inclusion and b) crosses the clean grain boundary located 150nm away.....	82
Figure 6-8	3D isocontours of a Cu _{1.4} Te cluster provided by APT showing the a) Cu and b) both Cu and Zn with the concentration threshold set at 25 and 6 at.% respectively	83
Figure 6-9	2-D contour plots obtained from the center of a Cu _{1.4} Te cluster confirming the core-shell structure with a Zn-enriched layer completely encasing a Cu _{1.4} Te cluster	83
Figure 7-1	Device efficiency as a function of copper loading in the ZnTe buffer for different metallization materials.....	90
Figure 7-2	J-V curves from devices with varying Cu content using a) gold, b) titanium and c) chrome metallization layers	91
Figure 7-3	QE spectra from devices with varying Cu content using gold, titanium and chrome.....	92
Figure 7-4	Changes in device efficiency during 300 hours of accelerated lifetime testing of a) in the dark and b) under illumination for the three metallization materials	94
Figure 7-5	J-V curves at selected times during dark ALT testing of devices with a) gold, b) titanium and c) chrome	95
Figure 7-6	J-V curves at selected times during dark ALT testing of devices contacted with a) gold, b) titanium, and c) chrome.....	96
Figure 8-1	Photographs of as-deposited CdS _{1-y} Te _y alloys	100
Figure 8-2	The transmission of CdS _{1-y} Te _y films with different y values	101
Figure 8-3	Parity plot comparing CdS _{1-y} Te _y alloy composition derived from QCM measurements with those based on measurement of the optical band gap	102
Figure 8-4	XRD analysis of the as-deposited alloy films	102
Figure 8-5	Box plots of J-V parameters and QE spectra of devices made with CdS _{1-y} Te _y alloys.....	103
Figure 8-6	Liftoff method and XRD of liftoff samples	104

LIST OF TABLES

Table 1-1	The performance of recent champion cells.....	12
Table 3-1	Summary of the J-V curves from Figure 3-7	47
Table 4-1	Comparison of the device parameters for both certified devices.....	52
Table 4-2	Parameters used in the SCAPS model	55
Table 5-1	Summary of device parameters in the three states.....	62

LIST OF SYMBOLS

CdCl ₂	cadmium chloride
CdS.....	cadmium sulfide
CdS:O.....	oxygenated cadmium sulfide
ZnTe.....	zinc telluride
ZnTe:Cu.....	copper doped zinc telluride
CdTe.....	cadmium telluride
E _g	band gap
TCO.....	transparent conductive oxide
HRT.....	highly resistive and transparent
FTO.....	fluorine-doped tin oxide
J _{sc}	short-circuit current density
V _{oc}	open-circuit voltage
FF.....	fill factor
η.....	efficiency
NREL.....	National Renewable Energy Laboratory
PV.....	photovoltaics
rf.....	radio frequency
R _s	series resistance
R _{sh}	shunt resistance
SEM.....	scanning electron microscopy
SIMS.....	secondary ion mass spectrometry
TEM.....	transmission electron microscopy
UV-Vis-NIR.....	ultraviolet-visible-near-infrared
XRD.....	X-ray diffraction
RTP.....	Rapid thermal processing
VTD.....	Vapor transport deposition
PEVTD.....	Plasma enhanced vapor transport deposition
QE.....	Quantum efficiency

APT Atom probe tomography
T Minority carrier lifetime

ACKNOWLEDGEMENTS

I cannot express enough thanks to my committee for their continued support and encouragement: Prof. Colin Wolden, my advisor; Prof. Tim Ohno, my committee chair; Prof. Brain Gorman and Prof. Sumit Agarwal. In addition, I really want to thank Dr. Joe Beach for his patient mentoring and careful guidance. I am truly grateful for the help and suggestions provided by them.

My advisor, Prof. Colin Wolden has spent a lot of time and effort not only in improving the work but also in helping me to become a good Ph.D. student. Prof. Tim Ohno and Dr. Joe Beach provided solutions, professional suggestions and comments on papers/presentations. The remaining committee members, including Prof. Sumit Agarwal and Prof. Brain Gorman, provided valuable advice and enforced realistic thinking in setting research goals.

My completion of this project could not have been accomplished without the support of my colleagues, Dr. Daniel Meysing, Abdulaziz Hussain, Jason Trevithick and Yegor Samoilenko.

The members of my family have been very important to me in the pursuit of this project. I would like to thank my parents, whose love and support are with me in whatever I pursue. I also wish to thank my loving and supportive boyfriend, who provides unending inspiration.

CHAPTER 1

INTRODUCTION

1.1 Renewable Energy

Energy is one of the most important things to human society. From food to clean water, from cars to houses, from lamps to computers, all the things rely on energy. Moreover, energy is a major source of the economic development for any country. Today, over 80% of the world energy comes from fossil fuels [1] including coal, petroleum (oil), and natural gas, which are not sustainable. When fossil fuels run out is only a matter of time. Globally, we currently consume the equivalent of over 11 billion tons of oil in fossil fuels every year [2]. If we carry on at this rate without any increase for our growing population or aspirations, our known oil deposits will be gone by 2052. We'll still have gas left, and coal too. But if we increase gas and coal production to fill the energy gap left by oil, then those reserves will only take us to 2088 without considering the world's population increases [3]. The other disadvantage of fossil fuels is the environmental concerns. The burning of fossil fuels is overloading our atmosphere with carbon dioxide and other global warming emissions, which irreversibly changes our climate [4]. So, today the focus is on both long-term adequacy supply of energy and also the environmental implications of particular sources.

Renewable energy, including wind, solar, geothermal, hydroelectric, and biomass, provides substantial benefits for our climate, our health, and our economy. Among them, solar represents the greatest untapped source of renewable energy available today. One hand, the sun provides energy for practically all living creatures on earth through the process of photosynthesis. On the other hand, people today are seeking to utilize solar radiation directly by converting it into useful heat or electricity. Solar or photovoltaic cells are devices that can convert solar radiation directly to electricity. The first generation solar cells are silicon based solar cells including single crystal silicon and polycrystalline silicon solar cells. These types of solar cells dominate the market and are mainly those seen on rooftops. Single crystal silicon solar cells have a quite high efficiency, but very pure silicon is needed, and due to the

energy-requiring process, the price is high compared to the power output [5]. Second generation solar cells are thin film solar cells including copper indium gallium selenide (CIGS) and cadmium telluride (CdTe). Only a few micrometers of these films are able to absorb most of the incident light. The Third generation solar cells include some innovative techniques like quantum dots, nano materials and organic materials. Although theoretically interesting, practical third generation devices have been disappointing [6].

Figure 1-1 shows the record research efficiencies of different kinds of solar cells. From this figure, we can see that over the last 15 years, there has been no efficiency increase of the crystalline Si cells. Also considering their high production price, people are paying more and more attention on thin film solar cells. CdTe, with an ideal band gap about 1.45 eV and a large absorption coefficient ($>10^4 \text{ cm}^{-1}$), has emerged as the leading thin film photovoltaic (PV) technology. The record efficiency of CdTe solar cells has increased sharply over the last few years to the current record of 22.1% reported by First Solar in 2016 [7]. More importantly, the record module efficiency now exceeds polycrystalline silicon, the leading technology in the market today.

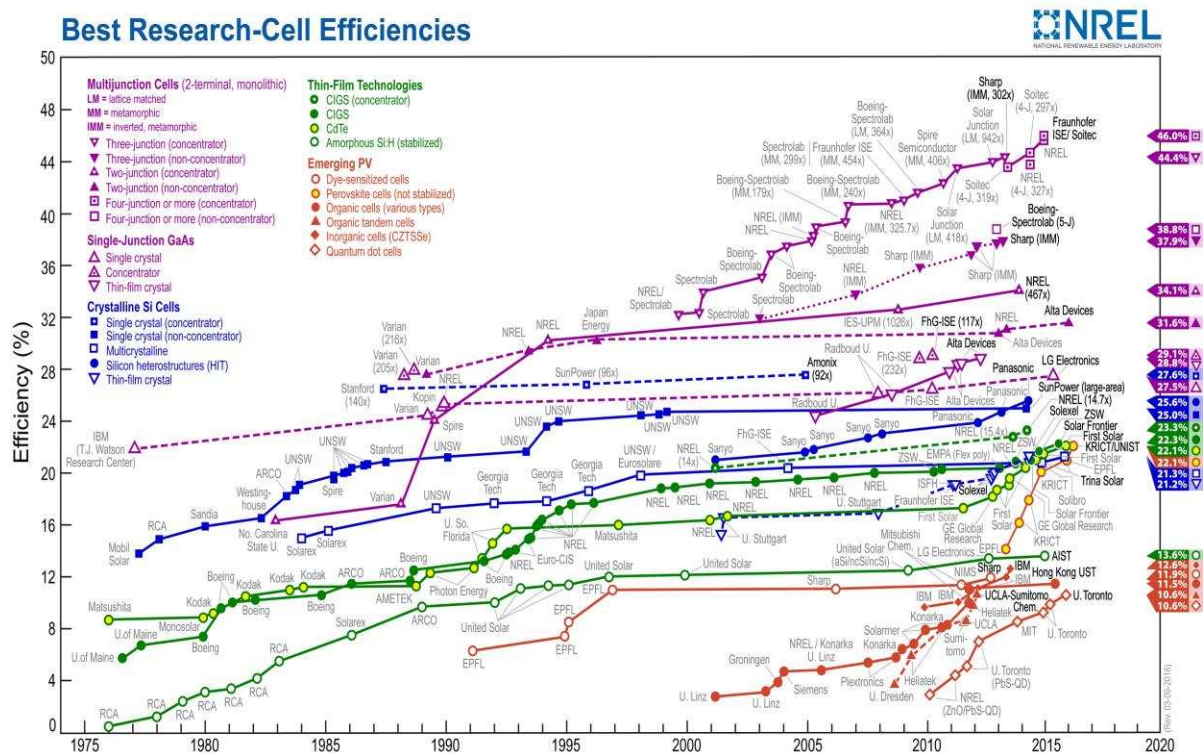


Figure 1-1: NREL best research-cell efficiencies. Adapted from [8].

1.2 CdTe Solar Cell Structure

Cadmium telluride is a direct band gap semiconductor with a band gap of 1.45eV, which is ideal for terrestrial PV. The theoretical maximum efficiency (Shockley–Queisser limit) under AM1.5 illumination versus band gap is shown in Figure 1-2. From this curve, we can see that CdTe is nearly optimally matched to the solar spectrum for photovoltaic energy conversion. It also has a high absorption coefficient which is greater than 10^4 /cm, which allows 99.9% of visible light to be absorbed by just 2 microns of material. These properties make CdTe an attractive absorber-layer material for thin-film solar cells.

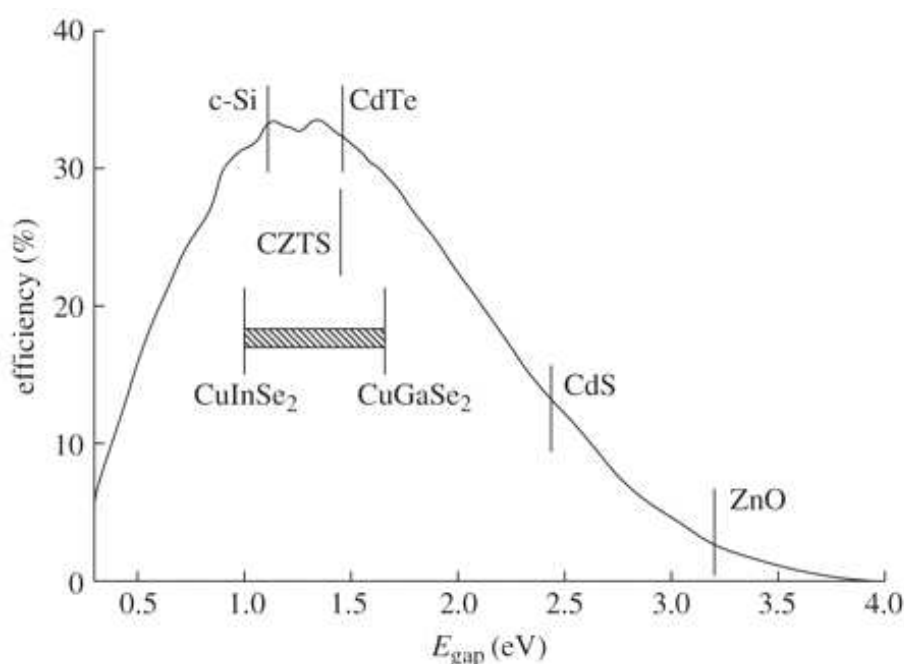


Figure 1-2: Shockley–Queisser limit. Adapted from [9].

The majority of CdTe based solar cells employ the so called “superstrate” configuration (Figure 1-3). In this arrangement, the light is incident on a glass sheet which serves as the substrate. Firstly a transparent conductive oxide (TCO) is deposited, and this acts as a conductive contact for the n-CdS of the p-n junction. The CdS is usually known as the “window layer” since most of the light transmitted through it will be absorbed by the “absorber”, i.e. the CdTe itself. The uppermost part of the structure is the back contact to the CdTe.

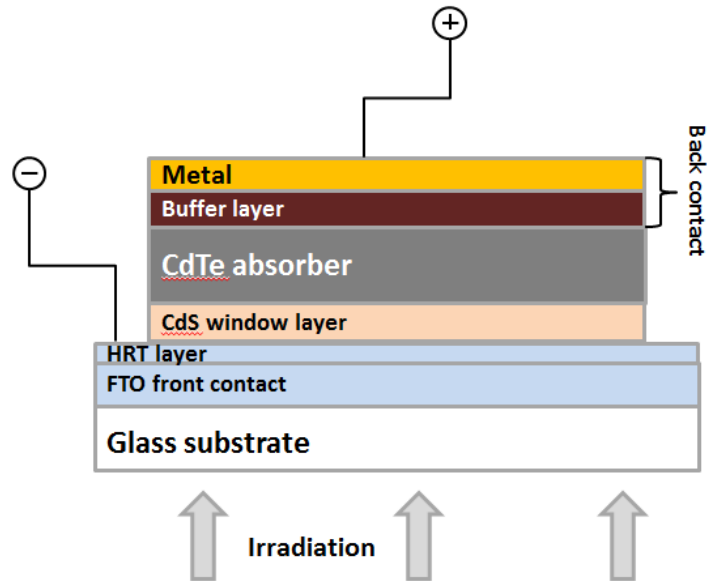


Figure 1-3: The configuration of superstrate CdTe solar cells.

Soda-lime glass and borosilicate glass are commonly used as the glass substrate. Soda-lime glass consists of 71 to 75% sand (SiO_2), 12 to 16% natron (Na_2O) and 10 to 15% CaO. Borosilicate glass consists of 70 to 80% sand, 7 to 13% boron trioxide, 4 to 8% sodium oxide and potassium oxide and 2 to 7% aluminum oxide [10]. Borosilicate glass has higher resistance to heat and temperature changes and higher annealing point, while soda-lime glass is cheaper. Because the glass transition temperature of soda-lime glass is only about 550°C , it is not suitable for processes with temperatures higher than that, so higher price borosilicate glass is used instead in some groups. We used soda-lime glass in all CSM made devices since the highest temperature we use was 420°C .

The main purpose of the TCO is to serve as a transparent electrode. So, it should be highly transparent to visible light, it should have low resistivity to make sure that electrons can be extracted efficiently, and it should have good stability at the maximum temperature at which other layers are prepared [11]. To make good ohmic contact, its electron affinity should be lower than that of the CdS. Moreover, its bandgap should be greater than 3eV to avoid absorption of light over most of the solar spectra [12]. Fluorine doped tin oxide (FTO) is the most widely used transparent conducting oxides for CdTe solar cells because of its electrical conductivity, optical transparency, low cost and thermal stability [13]. The sheet resistance of FTO can be managed by changing the thickness. The commonly used sheet resistance of FTO

coated glass for solar cells is 7 to 15 Ω/sq . and the thickness is 200 to 300 nm. The lower the sheet resistance, the thicker the FTO film, so the lower the transparency. Another high performance TCO for CdTe solar cells is cadmium stannite (CTO) [14]. It has better conductivity and transparency than FTO but it is not commercially available [15]. A high resistivity transparent (HRT) layer is typically added on TCO to make CdS layer as thin as possible. HRT layers can avoid the formation of localized CdTe/TCO junctions, which is due to the decrease of CdS thickness [16]. Intrinsic SnO_2 is used as the HRT layer with FTO, while zinc stannite (ZTO) is always used with CTO [17]. In most of our experiments, we used commercial TEC 15 from Pilkington; this is glass coated with FTO and a sheet resistance of 15 Ω/sq and it does not have an HRT layer.

CdS is an n-type semiconductor which is used to form the heterojunction with the p type CdTe. CdS creates a good heterojunction, but it generates no useful photocurrent. With a band gap of 2.4 eV, it absorbs blue light. CdS thin films are deposited by various methods including chemical bath deposition (CBD) [18], sputter deposition [19], and thermal evaporation [20]. Typical thickness ranges from 50-150 nm [21-23], and it is generally desirable to keep the CdS layer as thin as possible to allow a high fraction of the photons with energy above its band gap to reach the CdTe absorber and hence produce a high photocurrent. But thinner CdS will cause non-uniformity which will result in the formation of TCO/CdTe weak diodes [24], so the V_{OC} and FF will be impaired when the photocurrent flows back into these weak diodes. An alternative strategy is to use CdS:O, which has higher optical bandgap and relaxes thickness constraints [25]. Groups using CdS:O as the window layer also use an HRT layer to get good cell performance [26, 27]. HRT is always used to prevent shunts and/or weak TCO/CdTe diodes which are formed because the CdS layer is too thin and not uniform. Theoretical calculation showed that an inhomogeneous device modeled by a parallel connection of solar cells with a distribution of diode parameters can benefit from an additional series resistance [28]. But the recent work of our colleague showed that CdS:O window layer completely transformed into $\text{CdS}_{1-y}\text{Te}_y$ alloy and sulfate crystals during device fabrication. So instead of relying on interdiffusion and to avoid the formation of sulfate crystals, we explored using pre-formed $\text{CdS}_{1-y}\text{Te}_y$ alloys as the window layer. It is well known that during the device fabrication $\text{CdS}_{1-y}\text{Te}_y$ alloy will be formed because of the

interdiffusion of CdS and CdTe which causes a reduction in the lattice mismatch at CdS/CdTe junction [29] and a reduction of recombination current [30]. Radojicic *et al.* proposed that CdS_{1-y}Te_y could be used to replace CdTe to get negligible change in the spectral response of the device but improved fill factor because smaller lattice mismatch between CdS and CdS_{1-y}Te_y which provided a method to fabricate high-efficiency graded bandgap CdS_{1-y}Te_y thin film solar cells [31]. So we hope the usage of CdS_{1-y}Te_y as the window layer can avoid the formation of sulfate crystals from CdS:O, provide smaller lattice mismatch and fabricate new CdTe architectures through judicious use of preformed alloys and composition gradients.

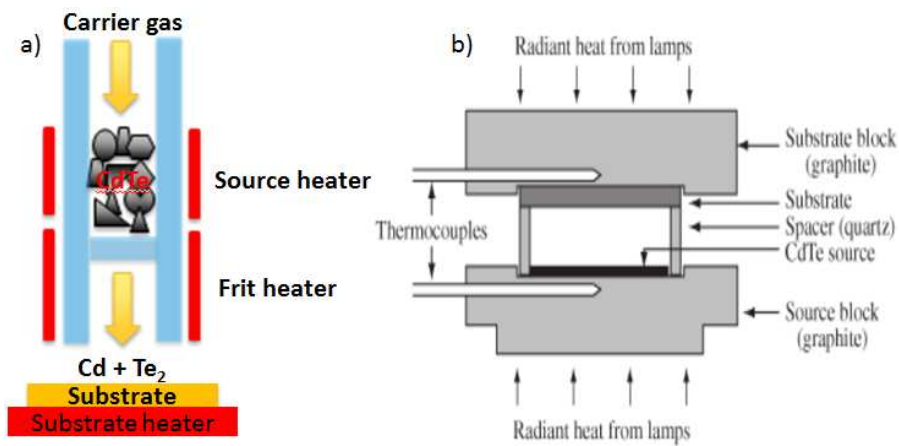


Figure 1-4: a) A configuration of the VTD system b) CSS deposition system. Adapted from [32].

CdTe can be deposited using many methods including sputtering [19], close space sublimation (CSS) [33], vapor transport deposition (VTD) [34] and electrodeposition [35]. VTD uses two heaters to heat the source and the frit as shown in Figure 1-4 a). VTD works by convective transfer of a vapor stream saturated with Cd and Te₂ to the substrate. CdTe in the source heater area is sublimated, releasing Cd atoms and Te₂ dimers. The temperature of the frit heater is higher than the source heater to prevent condensation, so the carrier gas will flow through the tube and carry Cd and Te₂ to the substrate where they will combine as CdTe at the substrate. The geometrical configuration of the source influences the uniformity and utilization of the vapors in the carrier gas. The close space sublimation method is used in CdTe depositions by a lot of research groups. In this method, the substrate is placed a few millimeters above a CdTe source plate and they are separated by a spacer as shown in Figure

1-4 b). During deposition, both the substrate and the CdTe source are heated, but the temperature of the substrate is about 50 °C lower than the temperature of CdTe source. During the process CdTe decomposes and sublimates from the source plate, and then Cd and Te₂vapors are transported from source to substrate by diffusion where they recombine to form a film. CdTe growth methods are classified by the temperature. Methods such as CSS or VTD with temperature above 500 °C are classified as high-temperature processes, while methods such as electrodeposition and sputtering with deposition temperature below 300 °C are classified as low-temperature processes [36]. Layers deposited by high-temperature processes exhibit large grain size of up to 1-5 μm owing to the enhanced mobility of atoms at the growth surface.

CdCl₂ treatment of CdTe is one of the critical steps of device fabrication and is essential in the production of high efficiency cells. CdCl₂ treatment has several advantages. Firstly, it helps the interdiffusion of S and Te to reduce the interfacial stress caused by lattice mismatch. Moreover, it facilitates recrystallization and grain growth. CdCl₂ is generally considered to be a fluxing agent that decreases the required treatment temperature at which physical changes occur in CdTe films [37]. At last, it is also found CdCl₂ treatment can passivate defects of CdTe films [38]. In our experiment, the samples were exposed to CdCl₂ in a close space sublimation geometry in a tube furnace at 400 °C for 30 min using a 50%-50% O₂/N₂ ambient which is shown in Figure 1-5.

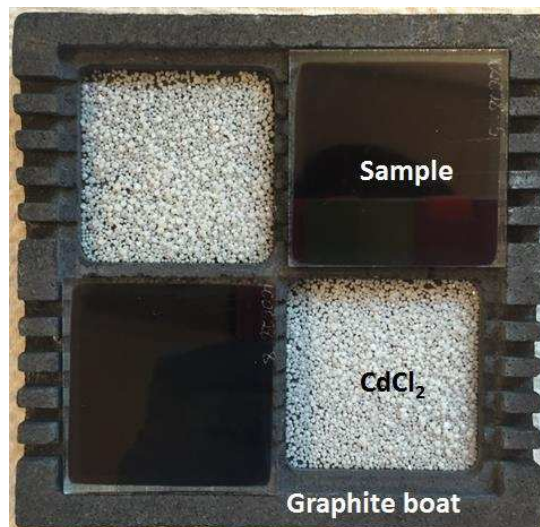


Figure 1-5: A photograph of our CdCl₂ treatment geometry.

It is notoriously difficult to make good ohmic contact with CdTe using conventional metals, because this requires a work function of greater than 5.7 eV [36]. Normally, there are two ways to form an ohmic contact with CdTe. Before applying back contact, it is typical to perform an etch to remove residual impurities from the CdCl₂ process and make the surface Te-rich. First, a thin (2-10 nm) layer of Cu is deposited on samples before metallization [39]. During heat treatment, Cu can react with Te to form Cu_xTe which acts as a highly doped layer between CdTe and metal and increases current flow by tunneling. The second method is introducing a high-work-function compound on CdTe, such as HgTe, Sb₂Te₃ [40] and ZnTe. This will decrease the barrier height and create a quasi-ohmic contact [41]. Copper-doped zinc telluride (ZnTe:Cu) is one of the most commonly employed buffer layers [42]. ZnTe was identified due to its valence band alignment and compatibility with CdTe [43, 44]. Copper is commonly used to degenerately dope this layer, which narrows the barrier width and permits electron tunneling, creating a quasi-ohmic contact [45]. But excess copper in the CdTe leads to the formation of recombination centers, so it is critical to precisely control both its amount and spatial distribution in order to obtain high efficiency. ZnTe:Cu film can be deposited by r.f. sputter deposition [42], vacuum co-evaporation [46], close spaced sublimation technique [47], and electrochemical deposition [43]. Its thickness ranges from 50 nm to 500 nm and Cu contents varies from 2 to 10 at.%. The substrate temperature during deposition is typically between 200 °C to 400 °C and a post-deposition anneal to activate the back contact is always carried out at 150 °C to 260 °C for 10 to 30 min. [42, 43, 47-50] The whole back contact process typically takes several hours. But the diffusion of Cu is not desirable during this process. It is well known that Cu is related to defects and degradations of CdTe solar cells [51-53]. The diffusion of Cu into CdTe results in the formation of Cu-related defects. Cu can exist as interstitial ions (Cu_i⁺) which is a deep donor state, substitutional deep acceptors in Cd site [54, 55], and neutral complexes like Cu_i-V_{Cd} and Cu_i-Cu_{Cd} [56]. Substitutional Cu (Cu_{Cd}) dopes the CdTe more p-type, but interstitial Cu (Cu_i) compensates the p-CdTe. Trap levels due to deep donors caused by formation of Cu complexes in p-CdTe have been reported [57, 58]. Demtsu *et al.* showed that carrier lifetime decreased with increased Cu concentration which is associated with increased recombination center density introduced by Cu in the CdTe layer [52]. Moreover, the diffusion of Cu to CdTe/CdS interface forms recombination

centers and shunts paths and degrades the cell performance [51, 59, 60]. So the diffusion of Cu into CdTe layer is detrimental. But the adding of Cu to ZnTe back contact increases device performance by degenerately doping ZnTe and creating a quasi-ohmic back contact [61]. So, Cu has dual roles: on one side, it helps increase the doping level of ZnTe and form an ohmic back contact, while on the other side, the diffusion of Cu to CdTe and CdTe/CdS interface causes defects and degradation. So, it is critical to control the diffusion and distribution of Cu. But conventionally, this layer is deposited at elevated temperatures, which makes the deposition and diffusion occur simultaneously and the control of the diffusion a big concern. To solve that problem, we developed the rapid thermal processing (RTP) technique which decouples the deposition and diffusion and significantly decreases the process time compared to conventional anneal methods. We evaporate ZnTe:Cu films at low temperature and apply short RTP treatments after the device is completed.

Reliability is one of the most important concerns of solar cells. A variety of degradation mechanisms may be occurring in CdS/CdTe solar cells. A common culprit for cell instability is the diffusion of Cu from the back contact into the CdS region [53]. The diffusion of the metallization materials from the contact metallization layer into the CdTe was also observed and may be related to the degradation mechanism [62][63]. Moreover, it is shown that the oxidation of Te and of CdTe beneath back contacts is a degradation mechanism of unencapsulated CdS/CdTe cells [64]. Some researchers have suggested that oxygen migration through the back contact might play a role in back contact degradation. This could result in the formation of an insulating oxide layer on the CdTe surface [64]. At last, an electric field is expected to affect degradation processes such as electro migration (drift) or ionic diffusion. In summary, the degradation of CdTe solar cells may be caused by the diffusion of metal atoms, the oxidation the films and the electric field. Among them, the diffusion of Cu from the back contact to CdS is the most probable mechanism. So, we want to decrease the amount of Cu we use as much as possible. From the SIMS profile of our optimal device [65], we found that over 80% of Cu supplied in ZnTe:Cu diffused into Au because Cu and Au are completely miscible. But the release of Cu from the Au into the device could cause degradation over time. Au is commonly used as the metallization layer in research labs because of its high work function (5.2 eV), stability in air, and ease of deposition. But Au is

not compatible with industrial manufacturing because of its high price. So researchers are looking for alternative materials such as Ag [66], Ni [67], Mo [68], Ti [69] etc. To replace the expensive Au and avoid the release of a lot of Cu from Au in the future, we explored Cr and Ti, which are less soluble with Cu, as the metallization materials. We optimized Cu loading with each metal and found that it is related to the solubility of Cu in different metals. Stability tests under dark and light stressing were carried out with different Cu loadings and metallization materials and the degradation mechanisms related to the diffusion of metal atoms were explained.

1.3 J-V Parameters

The most common method to evaluate solar cell performance is through is by looking at the J-V curve, which is shown in Figure 1-6. Six important cell parameters may be extracted from the J-V curve, which are efficiency (η), fill factor (FF), open circuit voltage (V_{OC}), short circuit current (J_{SC}), series resistance (R_S) and shunt resistance (R_{SH}).

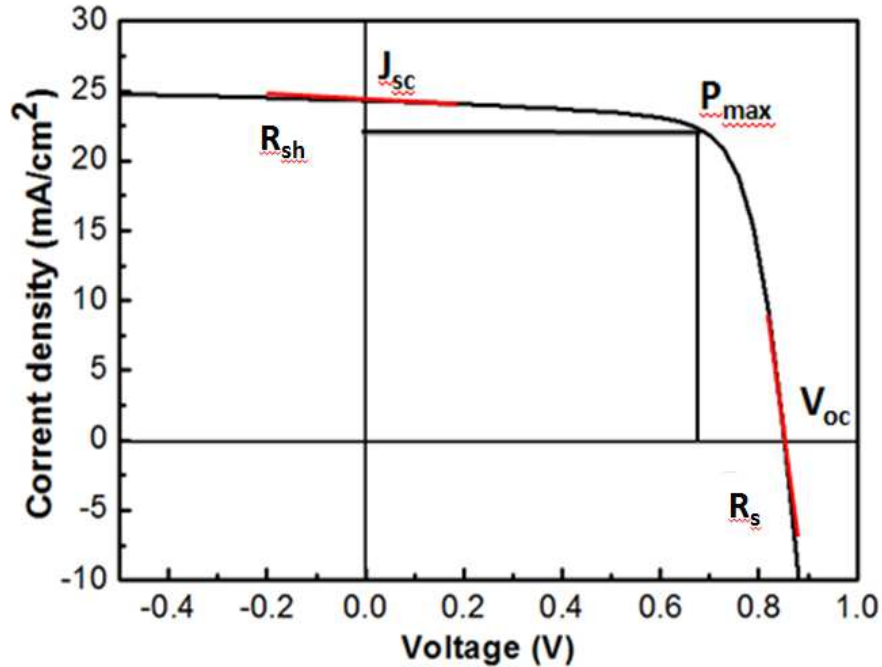


Figure 1-6: A representative J-V curve of a CdTe solar cell.

The open circuit voltage is the maximum voltage of the cell disconnected with external circuit under AM 1.5 solar spectral irradiance, while the short circuit current is the maximum

current when the solar cell is short circuited. Fill factor can be calculated by using the function below:

$$FF = \frac{P_{Max}}{J_{SC}V_{OC}} \quad (1-1)$$

where P_{Max} is the maximum output power.

To calculate the efficiency of the solar cell, we need to know the Fill Factor (FF), the short circuit current (J_{SC}) and the open circuit voltage (V_{OC}), which is given by:

$$Efficiency = \eta = \frac{FF \times J_{SC} V_{OC}}{P_S} \quad (1-2)$$

where the P_S is the input power from solar irradiance.

There are also two other parameters to diagnose the device, the shunt resistance and the series resistance, which are evaluated by the slope of the J-V curve at 0 bias and V_{OC} , respectively. The shunt resistance is ideally infinite, but is decreased due to the formation of alternate current paths for the light generated current. Low shunt resistance will reduce the amount of carrier flowing through the solar cell junction and decrease the voltage. The series resistance is ideally zero, but arises due to imperfect contacts between different layers of the front and back of the device. High series resistance will damage the fill factor and J_{SC} . So, we want shunt resistance as high as possible and series resistance as low as possible.

1.4 Current State of CdTe Solar Cells

First Solar has installed more than 10 GW with CdTe solar cells to date with manufacturing costs of ~\$0.6/W [77]. First Solar also holds the world record cell and module efficiency at 22.1% and 18.6% respectively [7]. However, further improvements in efficiency are required to lower balance of systems costs and become competitive with fossil fuel generated electricity [78]. Table 1-1 lists the recent champion cells and compares their J_{SC} , V_{OC} and FF with their potential values. After stagnating at 16.7% for nearly a decade [79], record device efficiencies have increased sharply over the past few years [71, 72] to the current standard of 22.1% reported by First Solar in 2016 [7]. Recent increases have been driven primarily by improvement in short circuit current density (J_{SC} , from 26 to 31 mA/cm²) and fill factor (FF, from 75 to 80%).

Table 1-1: The performance of recent champion cells.

Company	V_{OC}(mV)	J_{SC}(mA/cm²)	FF(%)	η(%)	References
NREL-2001	845	26.1	75.5	16.7	[70]
First Solar-2011	842	29.0	75.6	17.3	[71]
GE-2012	857	27.0	77.0	18.3	[72]
First Solar-2013	857	28.59	80.0	19.6	[73]
First Solar-2014	875	30.25	79.4	21.0	[74]
First Solar-2015	877	30.94	79.2	21.5	[75]
First Solar-2016	887	31.7	78.5	22.1	[7]
Theoretical	1065	30.5	88.6	28.8	[76]

In a recent presentation at the 43rd IEEE Photovoltaic Specialist Conference (Portland, Or, June 1016), First Solar candidly discussed the innovations that enabled their recent achievements [80]. In the presentation they acknowledged three specific changes, and these are discussed below along with a 4th significant departure from the conventional solar cell structure.

Replacement of CdS based emitters: Though not officially disclosed, First Solar devices display near perfect blue quantum efficiency all the way out to the TCO band edge (~300 nm). This implies that they are using an alternative to CdS, whose parasitic absorption is the largest loss mechanism in a conventional CdTe device [81]. One possibility is magnesium zinc oxide (MZO) [82], which the group at CSU has recently used with great success [83].

Use of ZnTe Buffer layers: First Solar has credited improvements in both record cell efficiency and module stability to the integration of ZnTe in their back contact structure [84]. This topic is a principle focus of this thesis and our work has provided some insight into the unique benefits of ZnTe.

Improved carrier lifetimes: There has been a significant increase in V_{OC} from 842 mV in Wu's cell to 887 mV in the current record. A well-established pathway to increase V_{OC} is through an increase in both carrier density and lifetime [85, 86]. Though carrier concentrations have remained essentially unchanged the lifetime in record cells has increased

from ~5 ns to 100 ns. One possible reason is because not using CdS allows them to use higher CdCl₂ temperature which always causes delamination in common CdS/CdTe solar cells. It is found that at high CdCl₂ treatment temperature, CdTe will delaminate from CdS [87, 88] because Cl will preferably segregate at CdS. Without CdS, they are able to use higher CdCl₂ treatment temperature which helps to passivate defects and results in higher carrier lifetime and V_{OC}. Moreover, they said that using alloyed absorber also helps them to get better carrier lifetime [80].

Alloyed absorber: As shown in Table 1-1, the J_{SC} values of recent record cells exceeds the theoretical potential of CdTe, and this is because First Solar no longer used pure CdTe but an alloyed absorber to get enhance red absorption. They substituted tellurium with Se to build a ternary compound with lower bandgap. Because of the bandgap of CdTe is 1.45 eV, red photons above 860 nanometers in wavelength are inaccessible to CdTe. With a reduction of the material bandgap toward the front of the device, those red photons can be absorbed and converted and contribute to the short circuit current. They also showed that CdTe band-gap grading enhanced carrier collection by enhancing absorber quality [89]. So, using CdTeSe is a way to increase CdTe solar cell performance.

Although J_{SC} and FF have been increased a lot during the last few years, the open circuit voltage (V_{OC}) in these champion cells has remained essentially unchanged at ~850 mV, far below the record of 1122 mV achieved in thin film devices employing GaAs [90], which is an absorber with a similar band gap. With J_{SC} and FF values approaching fundamental limits due to advanced front contacts, increasing the V_{OC} offers the greatest potential for further advances [85].

1.5 Outline of Thesis Goals

In this thesis, we are trying to better control and understand using ZnTe: Cu as the buffer layer for CdTe solar cells. During the course of this thesis, First Solar also announced the use of ZnTe in their back contact structure, crediting it as key to both record efficiency and improved stability [84]. We wanted to deeply explore the role of ZnTe:Cu by characterization of the impact of Cu dosing, activation, different metallization materials, and stability measurements. In addition, we explored using alloy CdS_{1-y}Te_y window layers to provide

opportunities to design and fabricate new CdTe architectures through band-gap grading.

The first goal was to develop a good control over the activation of ZnTe:Cu back contact with RTP technique. To achieve that goal, we optimized the back contact evaporation parameters including the Cu loading, the film thickness and the film configuration. The RTP treatment parameters including time and temperature were also optimized. RTP provides low thermal budgets and precise control over time-temperature trajectories. Moreover, it can facilitate activation and avoid any unwanted diffusion or oxidation due to extremely steep temperature ramps, which is very applicable to CdTe solar cell fabrication.

Next, we tried to further understand the role of Cu by using advanced characterizations. Copper is an essential component of effective back contacts, but its presence in the CdTe absorber creates detrimental recombination centers and its diffusion to CdS causing degradation. In this work the dramatic improvements in device performance afforded by this RTP process were tried to be quantified and interpreted through measurements of current-voltage (J-V), quantum efficiency (QE), carrier density (N_A) and minority carrier lifetime (τ). The redistribution of copper during RTP was examined using secondary ion mass spectrometry (SIMS) and atom probe tomography (APT). SIMS is used to quantify the extent of Cu diffusion into the CdTe absorber while APT is employed to characterize the back contact region with nanoscale resolution. We wanted to combine these measurements to postulate the changes in band structure that occur in the back contact region under optimal process conditions.

Then, we paid our attention to the metallization layer. The third goal was to replace Au with other cheaper metallization layers, Cr and Ti. Cu loading and RTP treatment parameters were optimized with regard to each metal. J-V curves were measured to provide the Cell performance under each condition. Reliability tests were made to further understand the role of the metallization layers.

Last, a novel window layer, $CdS_{1-y}Te_y$, was developed. Oxygenated cadmium sulfide (CdS:O) is an alternative CdTe window layer that delivers improved blue response relative to CdS. But our recent study revealed that CdS:O completely transforms during device fabrication into a layer containing cadmium sulfate clusters interspersed among $CdS_{1-y}Te_y$ nanocrystals. This motivated us to study CdTe solar cells employing pre-formed $CdS_{1-y}Te_y$

alloy windows without sulfate present. The intrinsic properties of alloys deposited by co-evaporation were evaluated with UV-vis and XRD. Then they were used in place of CdS in standard device fabrication. J-V, QE and post fabrication XRD were used to characterize the cell performance and the interdiffusion of CdS and CdTe. In this work we also addressed the role of the HRT layer in this device.

CHAPTER 2

MATERIALS AND METHODS

In this chapter, the experimental deposition systems and the device fabrication processes as well as the characterization techniques are described. First, the deposition techniques including thermal evaporation, vapor transport deposition and RF sputtering are described. Then, processes of the baseline and all devices used in this thesis are introduced. Last, relevant thin-film characterization methods are explained.

2.1 Thin Film Deposition Systems

2.1.1 Thermal Evaporation

Thermal evaporation is a common high vacuum technique for thin-film deposition. The source materials are always evaporated under high vacuum ($< 10^{-5}$ torr), with heat provided by Joule heating via a refractory element. Vapor particles can travel to the substrate and then condense back to solid state. The configuration of our thermal evaporation system is shown in Figure 2-1. During the deposition, source materials are put in quartz boats surrounded by a resistively heated tungsten coil. The chamber is evacuated by the mechanical pump and the diffusion pump, which can get to 10^{-6} torr in about an hour. The substrate is heated to the desired temperature (25 to 350 °C) during the evacuation of the chamber. When the chamber pressure is as low as needed, source heaters are turned on using variac and the deposition rates will be detected by two quartz crystal microbalances (QCMs) separately. When the desired deposition rates are reached, the shutter will be opened and the vapor of the source materials will transport to and condense on the rotating substrate. The deposition rate and film thickness will be continually detected by the QCMs. When we get the desired thickness, we will close the shutter and turn off the source and substrate heaters. Because there are two source heaters, two kinds of materials can be deposited together. A baffle prevents the QCM from detecting the other source material. In our experiments, we used the evaporator for CdS, ZnTe:Cu, Au and Cr. For CdS window layer, we evaporated a 150 nm film at 150 °C. For

ZnTe:Cu, we co-evaporated ZnTe and Cu at 100 °C. Other thicknesses were also used from different conditions. Alloy window layers were fabricated by co-evaporation of CdS and CdTe at 150 °C. We evaporated 100 nm Au and Cr at room temperature as the metallization layers.

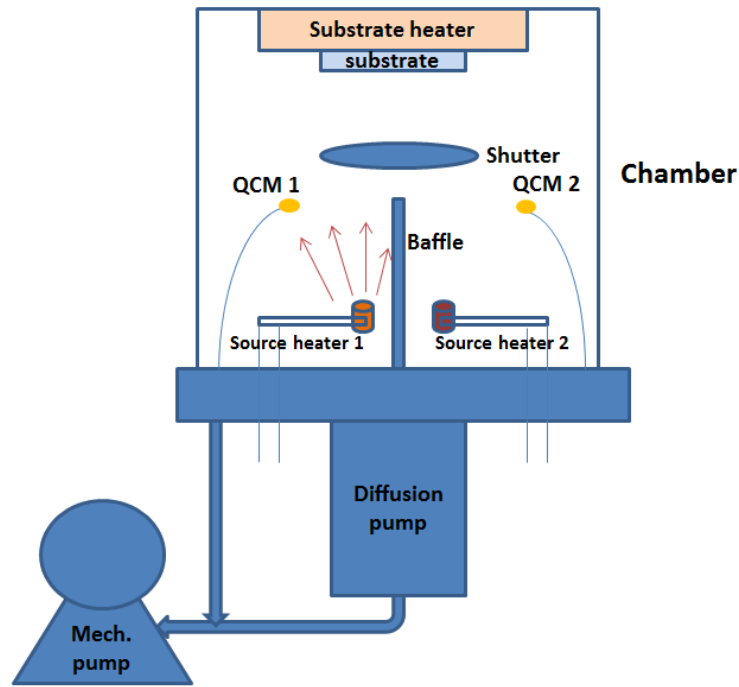


Figure 2-1: The configuration of the thermal evaporation system.

The phase change from a liquid state to a gaseous state is called evaporation. But in this case, the word “evaporation” also includes sublimation, which means the phase change from a solid state to a gaseous state. For evaporation, the saturated vapor pressure is the pressure at which the gaseous and condensed phases coexist. The relation between the saturated vapor pressure and the temperature is given by the *Clausius – Clapeyron relation*:

$$\ln \left(\frac{P_2}{P_1} \right) = - \frac{\Delta H_{vap}}{R} \left(\frac{1}{T_2} - \frac{1}{T_1} \right) \quad (2-1)$$

where P_1 , P_2 are the saturated vapor pressures at temperatures T_1 , T_2 respectively, ΔH_{vap} is the enthalpy of vaporization of the material and R is the universal gas constant.

To calculate the evaporation rate, we need to consider the molecular kinetics. During the deposition, two processes occur simultaneously: one is the evaporation of the condensed phase and the other is the condensation of the vapor molecules. According to the concept,

evaporation is a continuous process of molecular emission from the interface between the gas and condensed phases, and the rate of emission is governed by the thermal motion of molecules. The velocity of the reverse process (condensation) is proportional to the number of molecules per unit volume which is the partial pressure P^* . In a closed cavity, a state of dynamic equilibrium is established when the condensation rate is equal to the sublimation rate [91].

According to this model, the net evaporation flux of the gas molecules is the result of two counter processes, i.e., it is defined by the difference between the saturated vapor pressure which applies at the interface, and the partial pressure in the bulk vapor, P^* :

$$\frac{dN}{A dt} = \alpha_v (2\pi m k_B T)^{-1/2} (P^* - P) \quad (2-2)$$

This relation is known as the Hertz-Knudsen equation. Where A is the surface area, N is the number of gas molecules, m is the mass of a particle, k_B is the Boltzmann constant and α_v is the sticking coefficient for vapor molecules onto the substrate surface. P^* here refers to the system pressure during deposition.

So, the mass evaporation rates can be calculated by using the equation below:

$$\Gamma = m \frac{dN_e}{A_e dt} = \alpha_v \left(\frac{m}{2\pi k_B T} \right)^{1/2} (P^* - P) \quad (2-3)$$

Quartz crystal is a kind of piezoelectric materials, which can form electric field in the presence of mechanical stress and vice versa. So, when an alternating potential (sine wave) is applied, the crystal will oscillate. When the thickness of the crystal (t_q) is twice the acoustical wavelength, a standing wave can be established where the inverse of the frequency of the applied potential is of the period of the standing wave. This frequency is called the resonant frequency, f_0 , and is given by the equation [92]:

$$f_0 = \sqrt{\frac{\mu_q}{\rho_q}} / 2t_q \quad (2-4)$$

where μ_q is the shear modulus, ρ_q is the density, and t_q is the crystal thickness.

A quartz crystal microbalance measures a mass variation per unit area by measuring the change in frequency of a quartz crystal resonator, which is given by the equation below:

$$\Delta f = -\frac{2n f_0^2}{\sqrt{\rho_q \mu_q}} \frac{\Delta m}{A}; \quad T_f = \frac{\Delta m}{A \rho_f} \quad (2-5)$$

where Δm is the mass variation, T_f is the thickness of the deposited film, and ρ_f is the density

of the source material. A is a constant that related with the deposited material and the position of the QCM.

Diffusion pumps work on the principle of momentum transfer. They always use low vapor pressure oils. In this system which is shown in Figure 2-2, the oil is boiled by a heater and the oil vapor will go through the jet assembly. During operation, the heavy, high speed vapor molecule collides with a gas molecule and moves it in a preferred direction through the pump. The pump body is externally cooled so that the fluid will condense on its inside surface and run back down into the boiler. The pump body is externally cooled so that the fluid will condense on its inside surface and run back down into the boiler.

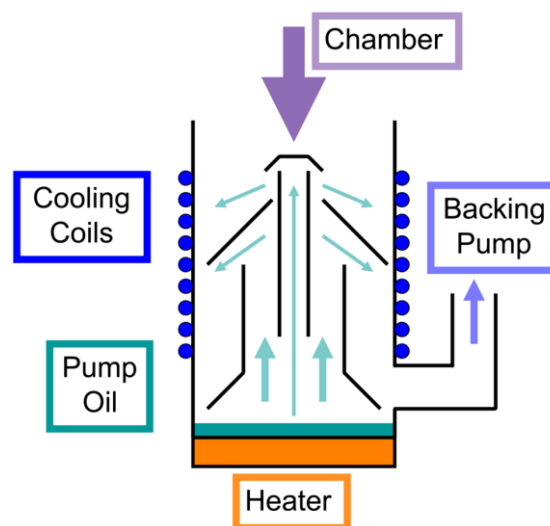


Figure 2-2: The configuration of the diffusion pump. Adapted from [93].

2.1.2 Vapor Transport Deposition

VTD is a kind of PVD thin-film deposition technique that was used in this work for CdTe deposition. VTD uses N_2 carrier gas flowing over solid CdTe placed in source heater, at where CdTe is sublimated to Cd atoms and Te_2 dimers into the flow as described earlier. The geometrical configuration of the system influences the thickness and uniformity of the film. We used VTD for CdTe deposition in our experiments. A photo of our VTD system is shown in Figure 2-3. During the deposition, the carrier gas, N_2 , was turned on and the flow rate was set at 365 sccm. Then we set the temperature of the frit heater to 650 °C and turned it on. After the temperature of the frit heater got 300 °C, we turned on the source heater and substrate heater to 600 °C and 420 °C separately. All heaters were controlled by PID

controllers and solid state relays. After about 30 min, all the temperatures were at their set temperatures and stabilized. We opened the shutter and started deposition. The typical film thickness was 3.5 μm and it typically took about 5 min. After certain time, we closed the shutter and turned off the source and substrate heater. Then, after the temperature of the source heater was below 450 $^{\circ}\text{C}$, we turned off the frit heater. The reason why we turned off the source heater first and then frit heat is to prevent the CdTe from condensing on the wall of the frit heater area. After the temperature of the substrate was below 50 $^{\circ}\text{C}$, we took the sample out. The deposition rate should be calibrated before film deposition. The described deposition rate is 3.5 $\mu\text{m}/5$ min. We can adjust the source temperature and the carrier gas flow rate to calibrate the deposition rate. With higher source temperature and higher gas flow rate, we can get higher deposition rate and *vice versa*.

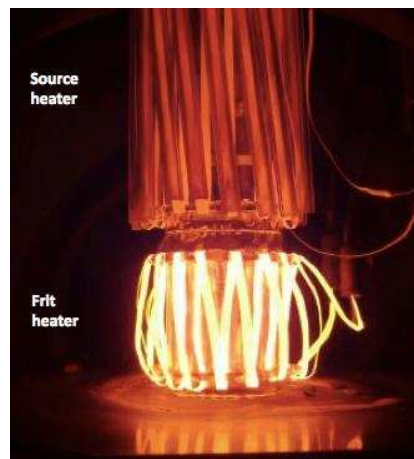


Figure 2-3: A photo of the VTD system.

2.1.3 Radio Frequency Magnetron Sputtering

Sputtering, a physical vapor deposition (PVD) technique performed under vacuum is always used in thin film depositions [94]. In this process ions bombard a target, ejecting particles onto a substrate which is shown by Figure 2-4. First, gaseous plasma is created through a cascade of electron impact ionization reactions. The ions from this plasma will be accelerated into the source materials (target). The source material is struck by the arriving ions and ejected in the form of neutral particles. Then, these neutral particles will travel in a straight line unless they come across with other particles or a nearby surface. The substrate

will be placed in the path of these ejected particles and will be coated by a thin film of the source material.

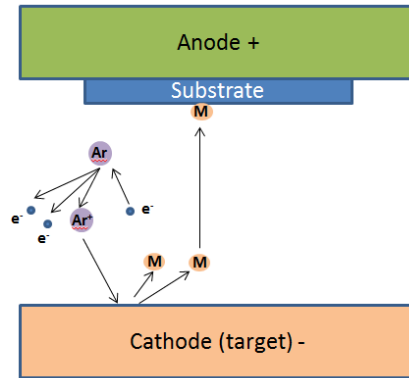


Figure 2-4: Sputtering process.

Figure 2-5 shows magnetron sputtering which uses magnets behind the cathode to trap the free electrons in a magnetic field in front of the target to prevent the electrons from bombarding the substrate. At the same time, these trapped electrons form an extensive and circuitous path which enhances the probability of ionizing a neutral gas molecule by several orders of magnitude, so the deposition rate is also increased significantly.

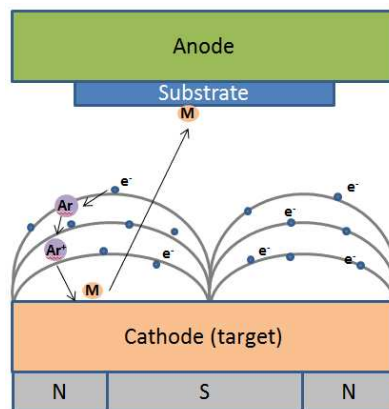


Figure 2-5: Magnetron sputtering.

Radio frequency magnetron sputtering can be used to sputter electrically insulating materials. If the source material is not conducting, the positive charge will build up on the materials and extinguish the plasma. In RF magnetron sputtering, the electrodes are biased

using 13.56 MHz alternating current (AC) power. Large ions cannot react quickly enough to the high frequency signal. Instead, they respond solely to the DC bias (mean of the AC signal). Electrons are affected by the AC field, oscillating toward and away from the target. Contact between electrons and the target neutralizes positive charges on the target surface, thereby reducing Ar⁺ repulsion.

Sputtering was used for Ti metallization layer. Firstly, the door between the load lock and the chamber was closed and then the load lock was vented. The substrate was loaded on the sample stage in the load lock and load lock was evacuated first by a mechanical pump and then a turbo pump until the pressure of the load lock was on the same order with the pressure of the chamber which was about 10⁻⁷ torr. Then the door between the load lock and the chamber was opened to transfer the substrate from the load lock to the sample stage in the chamber. After that, the door between the load lock and the chamber was closed. Next, we opened the mass flow controller (MFC) which controls the Ar flow rate into the chamber. We adjusted the pressure of the chamber to 5 mtorr through the usage of the MFC. When the pressure was stable, we ignited the plasma to start sputtering. The sputtering rate should be calibrated before the deposition of the film. The power input and the pressure of the chamber will influence the deposition rate. In our experiment, we used 100 W and the deposition rate was about 10 nm/min. After deposition, we turned off the power and then evacuated the chamber by the cryo pump to the same order with the pressure of the load lock. Finally, we used to load lock to take our substrate out.

2.1.4 Tube Furnace vs Rapid Thermal Processing

Tube furnaces are widely used heat treatment tool. It can be applied to annealing, physical vapor deposition, chemical vapor deposition and other high temperature processes. Rapid thermal processing is commonly used in semiconductor industry for dopant activation, interfacial reaction and thermal oxidation. Compared to conventional processing, it has very low thermal budget, high throughput and can avoid any unwanted diffusion or oxidation due to extremely steep temperature ramps [95]. At elevated temperatures, the short time processing feature of RTP results in the suppression or reduction of a number of undesirable thermally driven physical and chemical effects [96]. The principal advantage of RTP is due to

the fact that the occurrence of chemical and physical phenomena can be controlled precisely because the sample temperature acts as a reaction switch [97]. Thermal radiation is the dominant energy transfer mechanism in both the furnace and rapid isothermal processing. However, the spectral contents of the two energy sources are different. In the furnace, only photons in the infrared and the longer wavelength region have appreciable intensity and could be available for possible physical and chemical phenomena, while for the RTP, although the substrate temperature is low, intense halogen lamps provide substantial photon irradiation, so certain chemical and physical phenomena can be initiated or promoted [96].

In our experiment, tube furnace was used to run CdCl_2 treatment, which is a process that diffuses Cl into the bulk CdTe to help recrystallization, grain growth and defects passivation [37, 38, 98]. After CdTe deposition, the samples were exposed to CdCl_2 in a close space sublimation geometry in a tube furnace at 400 °C for 30 min using a 50%-50% O_2/N_2 ambient.

We used RTP for back contact activation. During the treatment, the substrate will be heated to high temperatures in only several seconds. Such high heating rates are often attained by using high intensity lamps or lasers. In our experiments, we used a commercial RTP furnace from MTI: OTF-1200X-4-RTP-UL. It has 8 units 1 KW halogen light with a max heating rate of 50 °C/sec which is shown in Figure 2-6. Our RTP treatments were always carried out under Ar ambient at about 2 torr. Our base line RTP treatment was one treatment at 320 °C for 30s followed by another treatment at 330 °C for 30s. But for samples from different groups, we re-optimized RTP parameters.

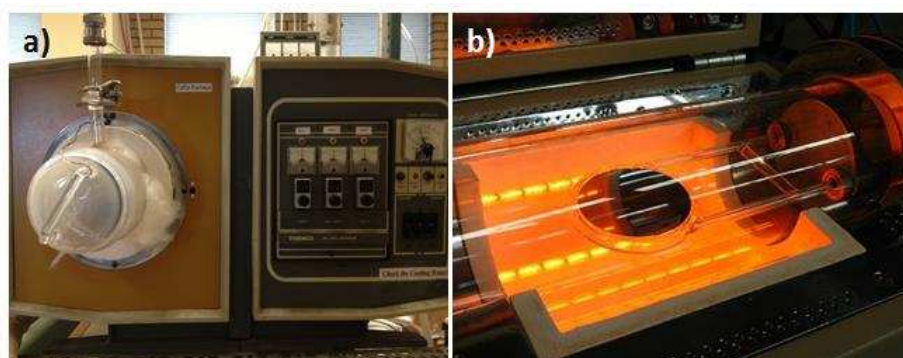


Figure 2-6: a) A photograph of the tube furnace b) A photograph of the RTP furnace while heating.

2.2 Baseline Solar Cell Fabrication

Figure 2-7 displays a baseline structure of the device architecture employed in this work. In our experiment, fluorine-doped tin oxide coated glass (TEC-15, Pilkington) was used as the substrate. Substrates were cleaned with detergent (Micro 90), rinsed with DI water, and processed in a UV-ozone furnace prior to device fabrication. First, 150 nm thick CdS layer was deposited by thermal evaporation at 150 °C. Then CdTe was deposited by using vapor transport deposition on a substrate at 420 °C and the thickness was about 3-4 μm [34]. The samples were exposed to CdCl_2 in a close space sublimation geometry in a tube furnace at 400 °C for 30 min using a 50%-50% O_2/N_2 ambient. The back surface was etched in a 0.5% $\text{Br}_2/\text{CH}_3\text{OH}$ solution for 10 s and rinsed with methanol prior to back contact preparation. A ZnTe:Cu buffer layer was deposited by thermal co-evaporation. The thickness of ZnTe was kept at 150 nm while the optimal thickness of Cu was 15 nm when using Au as the metallization layer.

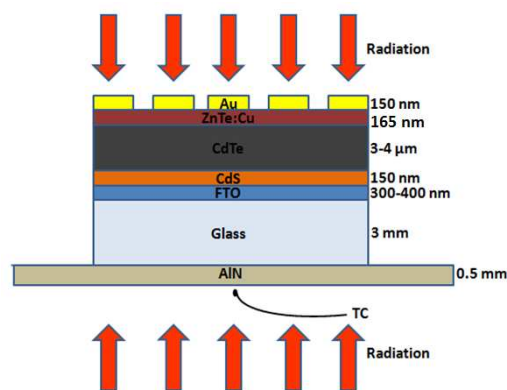


Figure 2-7: Configuration of RTP treatment and the baseline device architecture.

The thickness values are based on two shielded quartz crystal monitors that were used to control the evaporation rates and thicknesses of the individual sources. Devices with an area of 0.079 cm^2 were defined by evaporation of 150 nm of Au using a shadow mask. Individual devices were isolated by scribing along the perimeter of the metals through the semiconductors down to the transparent conductor. After device fabrication samples were subjected to RTP treatments to activate the back contact. Samples were placed on an AIN susceptor as shown inside a commercial RTP unit (RTP-10004, MTI Corporation) in which

the samples are exposed to heat lamps on all sides. Under an ambient of Ar the samples were ramped quickly ramped to the desired setpoint and held there for 30 s, at which time the lamps were turned off and the samples returned to ambient under convective cooling. In this work the reported temperatures are from a thermocouple placed in contact with the AlN susceptor.

2.3 Thin-Film Characterization Methods

2.3.1 Current-Voltage Measurement

A variety of measurements are made to determine the electrical characteristics of PV cells. Among them, current voltage measurement (I-V) is one of the most basic and important methods. I-V measurement is a photovoltaic (PV) device characterization technique that measuring the current as a function of an applied DC voltage to determine conversion efficiency and critical equivalent circuit parameters. The system includes the light source, the measurement electronics, computer, and software needed to measure solar cell I-V curves.

A light source is a solar simulator which is always used to simulate the standard solar spectral irradiance at 1 sun, air mass (AM) 1.5 G. 1 sun means the irradiance of one solar constant [99]. The irradiance of the sun on the outer atmosphere when the sun and earth are spaced at 1 AU, the mean earth/sun distance of 149,597,890 km, is called the solar constant. The solar constant is the total integrated irradiance over the entire spectrum, the area under the curve in Figure 2-8 plus the 3.7% at shorter and longer wavelengths.

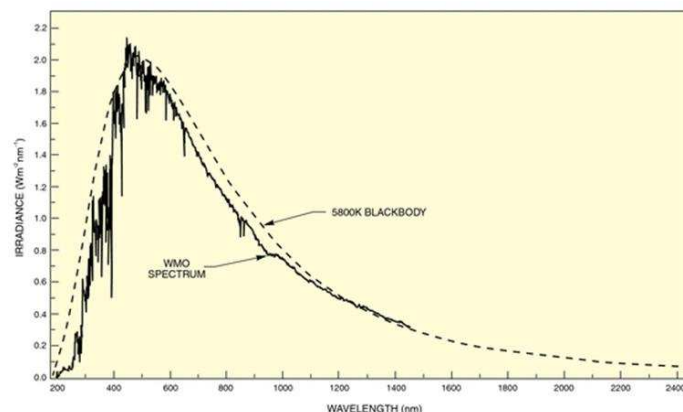


Figure 2-8: Spectrum of the radiation outside the earth's atmosphere compared to spectrum of a 5800 K blackbody. Adapted from Newport [99].

Air mass (AM) is the path length which light takes through the atmosphere normalized to the shortest possible path length (that is, when the sun is directly overhead). It quantifies the reduction in the power of light as it passes through the atmosphere and is absorbed by air and dust. An air mass of 1.5 were chosen for this standard because they are representative of average conditions in the 48 contiguous states of the United States [100]. These calculations give approximately 970 W/m^2 for AM1.5G and the standard AM1.5G spectrum has been normalized to give 1kW/m^2 due to the convenience of the round number and the fact that there are inherently variations in incident solar radiation [101].

Xenon arc lamps are commonly used for solar simulators. They have a relatively smooth emission curve, high intensities and an unfiltered spectrum which matches reasonably well to sunlight. However, the Xe spectrum is also characterized by many undesirable sharp atomic transitional peaks, making the spectrum less desirable for some spectrally sensitive applications. Xe arc lamps can be designed for low powers or up to several kilowatts, providing the means for small- or large- area illumination, and low to high intensities. Other lamp types, such as metal halide arc lamp, quartz tungsten halogen lamp and light-emitting diode, are also used sometime as the light source for solar simulation [102].

An equivalent circuit model of a solar cell is shown in Figure 2-9. It includes a photon current source (I_L), a diode, a series resistance (R_S), and a shunt resistance (R_{SH}). During the light measurement, the solar simulator illuminates the test device while the electronic load sweeps the cell voltage from a reverse-bias condition to beyond V_{OC} . The computer of the system gathers the data, calculates solar cell parameters and generates reports.

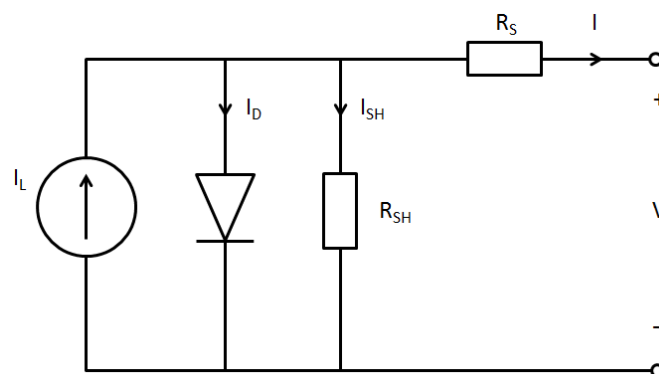


Figure 2-9: An equivalent circuit model of a solar cell.

2.3.2 External Quantum Efficiency (EQE)

External quantum efficiency measures the probability that a photon creates an electron-hole pair that is collected at 0 bias. EQE measures over a range of different wavelengths to characterize a device's efficiency. The key to measure the EQE is to quantify the intensity of monochromatic light incident to the device and measuring how much current is generated. During the measurement shown by Figure 2-10, light will be emitted from a light source and filtered. Then it will go through a monochromator and a chopper and focused by lenses onto the solar cell. The current generated by the solar cell under this wavelength will be measured. Before the lenses, a part of the light will be split onto a detector to monitor its intensity. Total optical power incident on the detector will be compared to the current generated by the solar cell to calculate the external quantum efficiency.

A calibration on the light should be done first before the measurement. Typically, a calibration measurement is run using a reference Si cell. The procedure includes measuring the reading from a reference device sitting in place of the sample holder and comparing this reading to a calibrated photodiode at a separate port. For instance, if the reading of the reference cell is 10% higher than the calibrated photodiode, this can be used to determine the light reaching the reference cell.

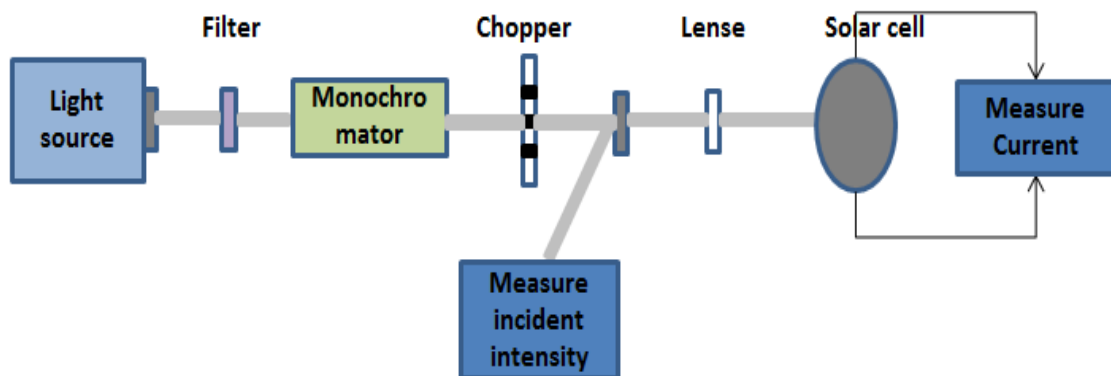


Figure 2-10: Eternal quantum efficiency system setup.

The wavelength resolution depends on the monochromator. A monochromator is an optical device that transmits a selected narrow band of wavelengths of light or other radiation chosen from a wider range of wavelengths available at the input [103]. Figure 2-11 shows the

configuration of a monochromator. A light from the light source irradiates on an entrance slit. Throughput and resolution can be adjusted by selecting the appropriate slit size. Then the light will be reflected from the collimator to get collimated light. Next, the collimated light is diffracted from the grating and then refocused by another mirror to the exit slits. At the exit slit, the colors of the light are spread out. Because each color arrives at a separate point in the exit slit plane, there are a series of images of the entrance slit focused on the plane. The range of colors leaving the exit slit is a function of the width of the entrance slit and exit slit, so the entrance and exit slit widths are adjusted together to get desired wavelength range and resolution [104].

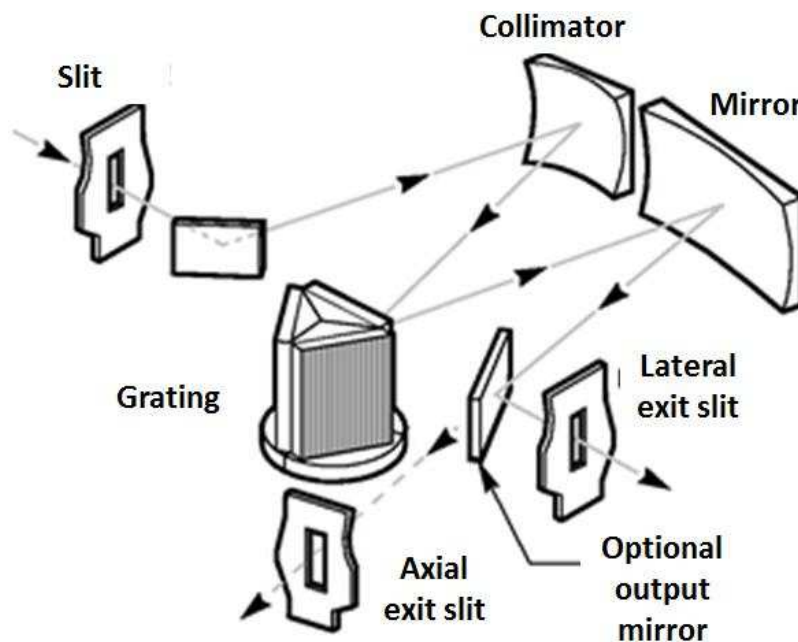


Figure 2-11: Optical configuration of a monochromator. Adapted from [105].

External quantum efficiency in this work was measured on a custom system with a grating monochromator and lock-in amplifier detection. Figure 2-12 shows representative EQE curves we measured with our samples. Blue response loss is due to front contact recombination, the overall QE reduction is mainly caused by the reflection and bulk recombination. As one approaches the bend edge, the red response is reduced due to rear surface recombination, reduced absorption at long wavelengths, short diffusion lengths of carriers.

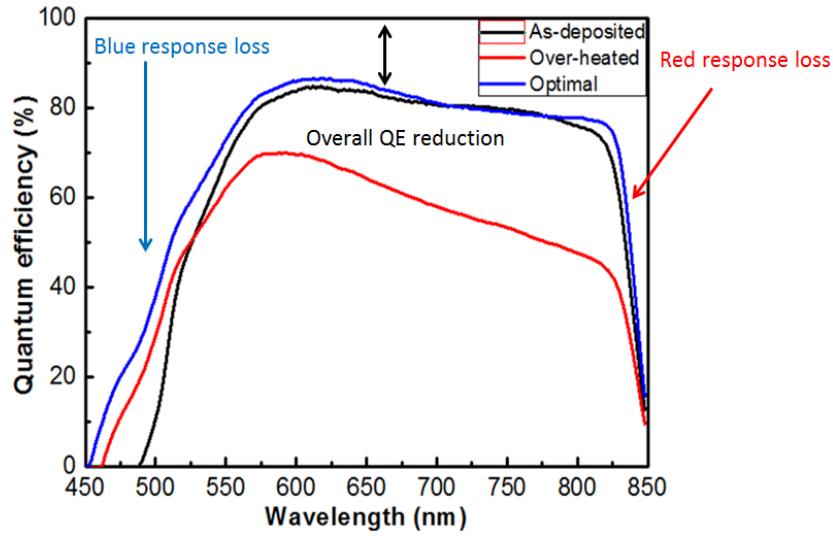


Figure 2-12: QE curves of our samples.

2.3.3 Time Resolved Photoluminescence

TRPL is a method that uses a pulsed light source to excite luminescence from the semiconductor and then measures the subsequent decay in photoluminescence (PL) as a function of time via time-correlated single photo counting (TCSPC). In TCSPC, the laser pulse is split into two beams with a beam splitter. The first beam triggers a time-amplitude converter (TAC) to define a “start”. The second beam excites PL from the sample. Some of the PL is first dispersed in a spectroscop and then detected by a gated intensified CCD camera. In the camera the light beam is converted to electron beam and goes through a sweeping device to finally obtain a spectrally and time resolved signal. The time between sample excitation by a pulsed laser and the arrival of the emitted photon at the detector is measured. The measurement of this time delay is repeated many times to account for the statistical nature of the fluorophores emission. The delay times are sorted into a histogram that plots the occurrence of emission over time after the excitation pulse. The schematic view is shown in Figure 2-13.

The PL density is proportional to the rate of radiative recombination. For direct bandgap recombination, the radiative recombination rate per unit volume, R_{rad} , is given by

$$R_{rad}(t) = B[p(r, t)n(r, t) - p_0(r)n_0(r)] \quad (2-6)$$

where B is the radiative recombination coefficient and p_0 and n_0 are the equilibrium hole and electron concentrations respectively. For p-type semiconductor, $p_0 \gg n_0$ and substitution of

$p=p_0+\beta$ and $n=n_0+\eta$ into Eq. 2-6 gives

$$R_{rad}(t) = B[p_0(r) + \beta(r, t)]\eta(r, t) \quad (2-7)$$

where β and η are the excess hole and electron concentrations respectively. In low-injection conditions, $\beta \ll p_0$, so Eq. 2-7 indicates that the rate of radiative recombination is linearly proportional to the number of minority carriers.

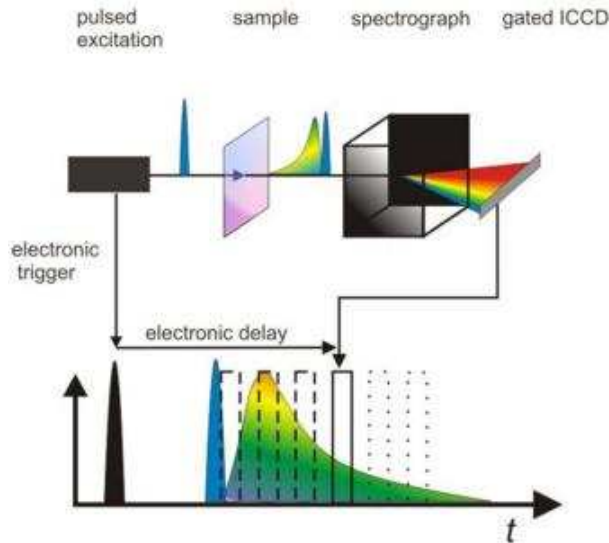


Figure 2-13: Schematic view of the TRPL setup. Adapted from MPI-P Research [106].

So PL density is proportional to minority carrier recombination. Even if the recombination is due to nonradioactive processes such as Auger and Shockley-Read-Hall (SRH) or under high-injection conditions, the PL decay can also tracks the excess carriers. The carrier life times of CdTe thin films are generally range from several hundred picoseconds to several nanoseconds. The carrier life time is often correlated with open circuit voltage (V_{oc}) [107]. In this work, Time resolved photoluminescence (TRPL) measurements used to determine minority carrier lifetime were performed at the National Renewable Energy Laboratory (NREL) using 650 nm pulsed laser excitation [108].

2.3.4 Secondary Ion Mass Spectrometry

Secondary ion mass spectrometry, shown in Figure 2-14, is a measurement method always used to analyze the composition of a solid material sample. In SIMS, material is removed using a focused primary ion-beam sputtering. The secondary ionized sputtered

species will be collected and analyzed by passing through an energy filter and mass spectrometer at where they will be converted to impurity densities. These secondary ions are also monitored by time which will be converted to the depth of the sample. The sputter depth verses the impurity densities will be plotted to get the analysis result. In this work, the Dynamic SIMS was performed using an ION-TOF Model IV.

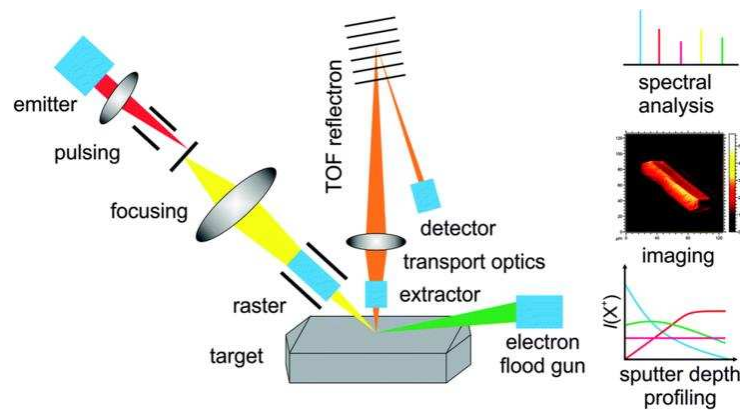


Figure 2-14: Schematic view of SIMS setup. Adapted from [109].

2.3.5 Atom Probe Tomography

Atom probe tomography has been demonstrated to be a powerful tool for characterizing polycrystalline solar cells, and in particular its 3D capability has been recently deployed to characterize the segregation of impurities at the grain boundaries in CdTe devices. APT is particularly suitable for interface detections because it delivers the highest spatial resolution 3 dimension compositional information of any microscopy technique. Figure 2-15 shows the structure of the RTP. Essentially, it produces a tip by focused ion beam and atoms are evaporated one at a time. The atom will be extracted into a time of flight mass spectrometer and fly toward a two-dimensional position sensitive detector, then their hit position in x and y is recorded. Gradually, each atom on the surface evaporates and exposes the underlying layers. The sequence of atom hits on the detector can be used to track both the serial evaporation of atoms in a given layer and the serial evaporation of the layers. The three dimensional image is thus reconstructed from this combination of two-dimensional hit positions and field evaporation sequence. APT analyses in this work were performed on a Cameca LEAP 4000X Si local electrode atom probe instrument using parameters optimized

for quantitative evaluation of these materials [110].

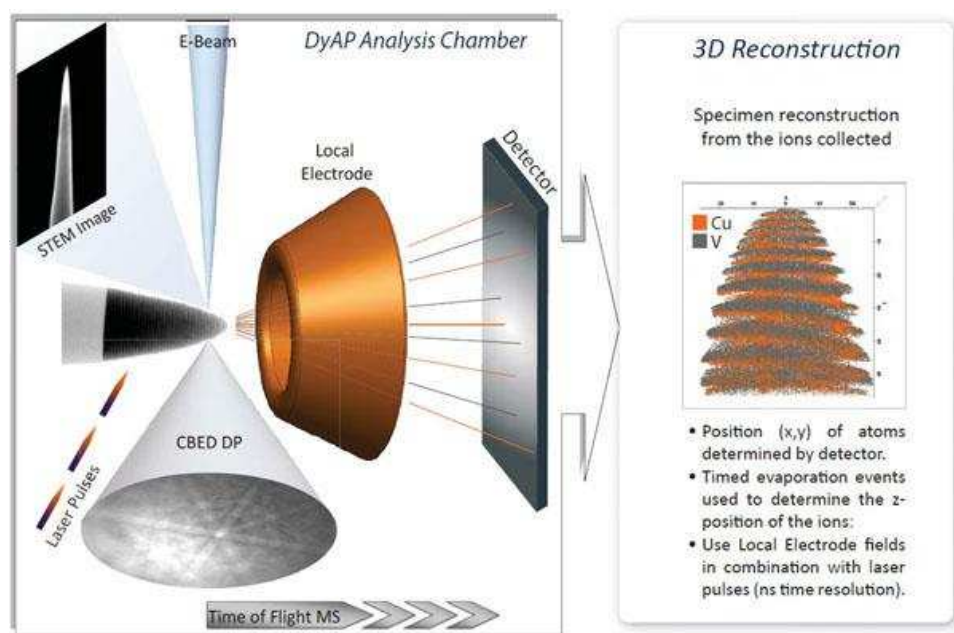


Figure 2-15: Schematic diagram of APT

2.3.6 Ultraviolet-Visible-Near Infrared spectroscopy

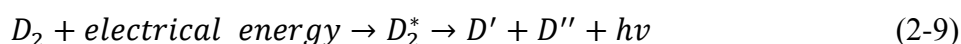
Ultraviolet-visible-near infrared spectroscopy (UV-VIS-NIR) refers to the transmittance or reflectance spectroscopy in the ultraviolet to near infrared spectral region. The radiation can interact with matter which excites electrons from the ground state to an excited state. For semiconductors, they have non-bonding electrons in their valence band, so these electrons can absorb photons with energy higher than the band gap and be excited to the conduction band. We can calculate the energy of the photon based on the equation:

$$E = \frac{hc}{\lambda} \quad (2-8)$$

where h is Planck's constant and c is the speed of light. For CdTe, its band gap is about 1.45 eV. If the energy of the photo is higher than 1.45 eV, which means the wavelength is shorter than 850 nm, it can be absorbed by the electrons in the valence band of CdTe to be excited into the conduction band. The bandgaps of the semiconductors can be interpreted from their transmission spectra by using Tauc relation: plot $(\alpha hv)^r$ vs hv , where $\alpha = 2.303 \log(T/d)$, d is the thickness of the film and $r=2$ for direct bandgap semiconductors, $r=1/2$ for indirect

bandgap semiconductor. The values of E_g can be estimated by taking the intercept of the extrapolation to zero absorption with photon energy axis.

The setup of the UV-VIS-NIR shown in Figure 2-16 includes light sources (UV and visible), monochromator, detectors, amplifier and readout. Tungsten filament lamp is commonly employed as a source of visible light. This type of lamp is used in the wavelength range of 350 to 2500 nm. A deuterium or hydrogen lamp is always used as the source of ultra-violet light. The electrical excitation of deuterium or hydrogen at low pressure produces a continuous UV spectrum. The mechanism for this involves formation of an excited molecular species, which breaks up to give two atomic species and an ultraviolet photon. This can be shown as:



Both deuterium and hydrogen lamps emit radiation in the range 160 to 375 nm.

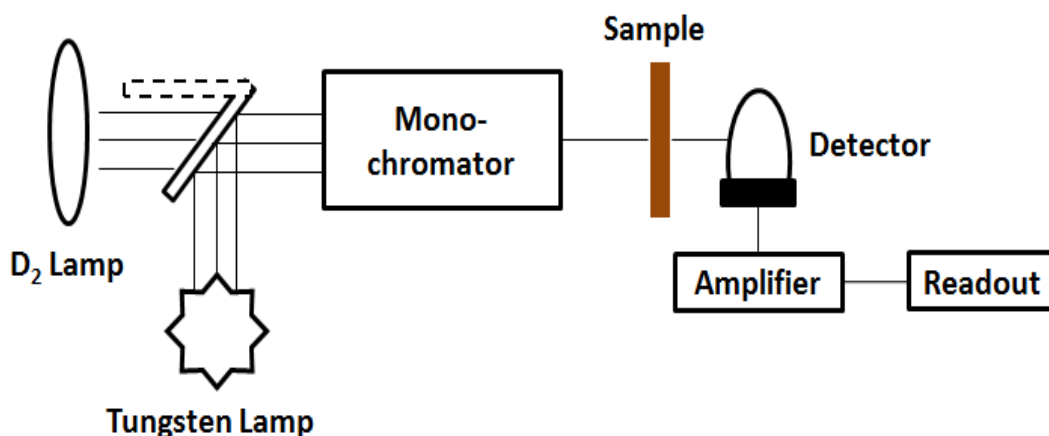


Figure 2-16: Schematic diagram of UV-VIS-NIR.

The photomultiplier tube is a commonly used detector in UV-Vis spectroscopy. It consists of a photo emissive cathode (a cathode which emits electrons when struck by photons of radiation), several dynodes (which emit several electrons for each electron striking them) and an anode. A photon of radiation entering the tube strikes the cathode, causing the emission of several electrons. These electrons are accelerated towards these dynodes and emit a lot of electrons. Eventually, the electrons are collected at the anode. By this time, each original photon has produced $10^6 - 10^7$ electrons. The resulting current is amplified and

measured [111].

During the measurement, the range of the wavelength should be selected based on the properties of the sample. For CdTe, its bandgap is 1.45 eV which equals to the energy of photons with 850 nm wavelength, so we usually select 700 to 1000 nm. A reference sample should be measured first to set a baseline for the experimental sample. The photons with different wavelengths will go through or be reflected by the sample and the current will be amplified and measured. The measured current is proportional to the photons that transmit through or reflected by the sample. So the transmittance or reflectance spectroscopy of the sample in the ultraviolet to near infrared spectral region will be achieved.

2.3.7 X-Ray Diffraction

X-ray diffraction (XRD) is a rapid analytical technique primarily used for identifying the components and crystal structures of the sample. X-ray diffraction is based on Bragg's Law shown in Figure 2-17:

$$n\lambda = 2d \sin \theta \quad (2-10)$$

where n is an integer, λ is wavelength, d is the inter-planar spacing in the crystal lattice, θ is the angle between the sample surface and incident beam. The X-rays are generated by a cathode ray tube, filtered to produce monochromatic radiation, collimated to concentrate, and directed toward the sample. The interaction of the incident X-rays with the sample produces constructive interference when conditions satisfy Bragg's Law. This law relates the wavelength of electromagnetic radiation to the diffraction angle and the lattice spacing in a crystalline sample. These diffracted X-rays are then detected, processed and counted. By scanning the sample through a range of 2θ angles, all possible diffraction directions of the lattice should be attained due to the random orientation of the powdered material [112]. Comparison these angles with standard reference patterns allows identification of the crystal because each crystal has a set of unique diffraction angels.

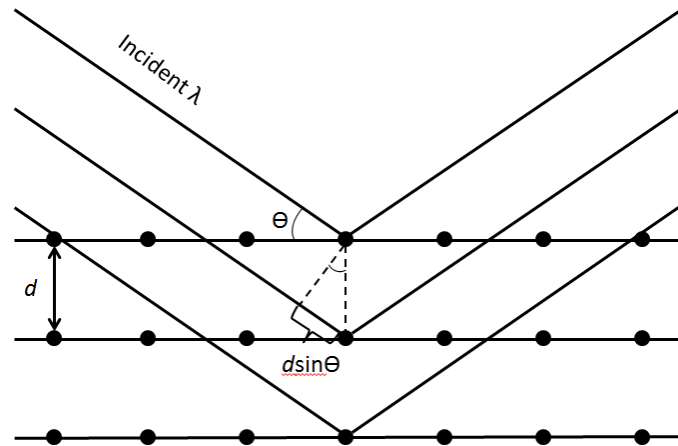


Figure 2-17: Bragg's law.

Figure 2-18 shows the geometry of an X-ray diffractometer. X-ray diffractometers consist of three basic elements: an X-ray tube, a sample holder, and an X-ray detector [113]. The sample rotates in the path of the collimated X-ray beam at an angle θ while the X-ray detector rotates at an angle of 2θ to collect the diffracted X-rays. X-rays are generated in a cathode ray tube by heating a filament to produce electrons, accelerating the electrons toward a target by applying a voltage, and bombarding the target material with electrons. When electrons have sufficient energy to dislodge inner shell electrons of the target material, characteristic X-ray spectra are produced. These spectra consist of several components, the most common being K_{α} and K_{β} . K_{α} consists, in part, of $K_{\alpha 1}$ and $K_{\alpha 2}$. $K_{\alpha 1}$ has a slightly shorter wavelength and twice the intensity as $K_{\alpha 2}$. The specific wavelengths are characteristic of the target material (Cu, Fe, Mo, Cr) [114]. Filtering, by foils or crystal monochrometers, is required to produce monochromatic X-rays needed for diffraction. $K_{\alpha 1}$ and $K_{\alpha 2}$ are sufficiently close in wavelength such that a weighted average of the two is used. Copper is the most common target material for single-crystal diffraction, with $\text{Cu}K_{\alpha}$ radiation = 0.5418\AA . These X-rays are collimated and directed onto the sample. As the sample and detector are rotated, the intensity of the reflected X-rays is recorded. When the geometry of the incident X-rays impinging the sample satisfies the Bragg Equation, constructive interference occurs and a peak in intensity occurs. A detector records and processes this X-ray signal and converts the signal to a count rate which is then output to a device such as a printer or computer monitor [112].

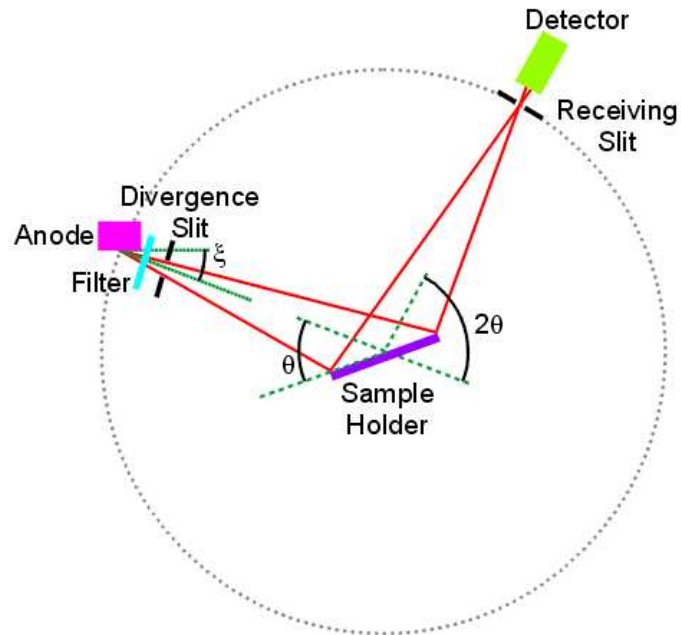


Figure 2-18: Geometry of the X-ray diffractometer. Adapted from [115].

2.3.8 Scanning Electron Microscope

A scanning electron microscope (SEM) is a type of electron microscope that uses a focused beam of electrons scanning the sample to produce images of the surface morphology of the sample. Qualitative and quantitative chemical analysis information is also obtained using an energy dispersive x-ray spectrometer (EDS) with the SEM. The electrons interact with atoms in the sample, producing various signals that contain information about the sample's surface topography and composition. The electron beam is generally scanned in a raster scan pattern, and the beam's position is combined with the detected signal to produce an image. SEM can achieve resolution better than 1 nanometer [116].

The setup of the SEM is shown in Figure 2-19. The SEM generates a beam of incident electrons in a vacuum chamber above the sample chamber. Then the electrons are accelerated by an anode and focused into a small beam by a series of electromagnetic condenser lenses in the SEM column. Scanning coils near the end of the column direct and position the focused beam onto the sample surface.

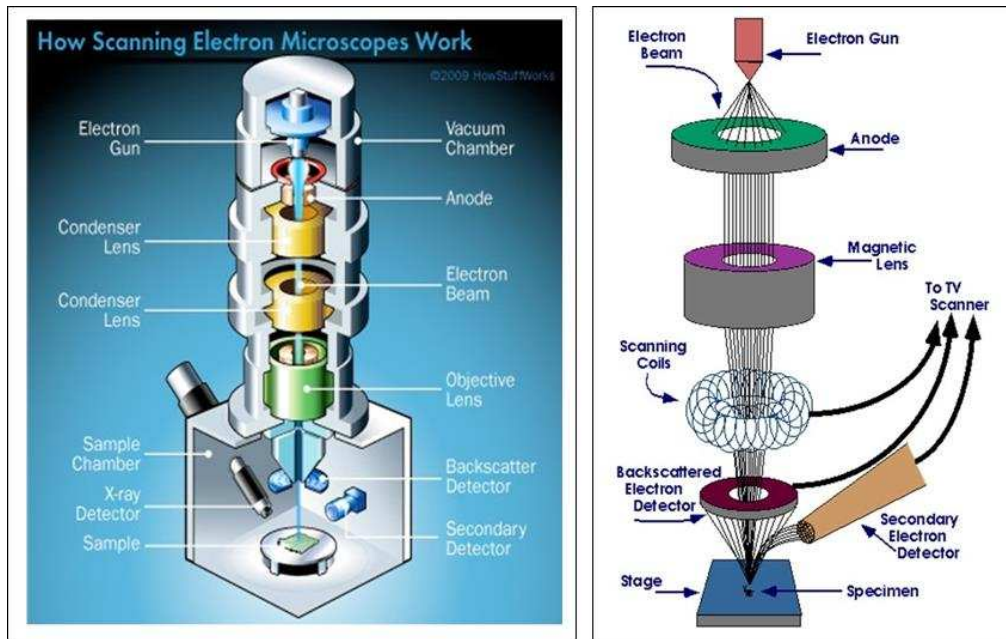


Figure 2-19: Basic SEM setup and its electron path. Adapted from [117].

The SEM column and sample chamber are at a moderate vacuum to allow the electrons to travel freely from the electron beam source to the sample and then to the detectors. High-resolution imaging is done with the chamber at higher vacuum, typically from 10^{-5} to 10^{-7} torr. Imaging of nonconductive, volatile, and vacuum-sensitive samples can be performed at higher pressures.

Accelerated electrons in an SEM carry significant amounts of kinetic energy, and this energy is dissipated as a variety of signals produced by electron-sample interactions when the incident electrons are decelerated in the solid sample. These signals include secondary electrons (that produce SEM images), backscattered electrons (BSE), diffracted backscattered electrons (EBSD that are used to determine crystal structures and orientations of minerals), photons (characteristic X-rays that are used for elemental analysis and continuum X-rays), visible light (cathode luminescence–CL), and heat. X-ray generation is produced by inelastic collisions of the incident electrons with electrons in discrete orbitals (shells) of atoms in the sample. As the excited electrons return to lower energy states, they yield X-rays that are of a fixed wavelength (that is related to the difference in energy levels of electrons in different shells for a given element). Thus, characteristic X-rays are produced for each element in a mineral that is "excited" by the electron beam [118]. Emitted lower-energy electrons resulting

from inelastic scattering are called secondary electrons. Secondary electrons can be formed by collisions with the nucleus where substantial energy loss occurs or by the ejection of loosely bound electrons from the sample atoms. The energy of secondary electrons is typically 50 eV or less. The most common SEM mode is detection of secondary electrons emitted by atoms excited by the electron beam. The number of secondary electrons that can be detected depends, among other things, on the angle at which beam meets surface of specimen, i.e. on specimen topography [119]. By scanning the sample and collecting the secondary electrons that are emitted using a special detector, an image displaying the topography of the surface is created. Scintillator type detectors (Everhart-Thornley) are used for secondary electron imaging. This detector is charged with a positive voltage to attract electrons to the detector for improved signal to noise ratio [120].

CHAPTER 3

RAPID THERMAL PROCESSING OF ZNTE:CU CONTACTED CDTE SOLAR CELLS

This chapter is adapted from its published form in IEEE Photovoltaic Specialists Conference [20].

3.1 Introduction

With an ideal band gap about 1.45 eV and a large absorption coefficient ($>10^4 \text{ cm}^{-1}$) CdTe has emerged as the leading thin film photovoltaic (PV) technology. First Solar produced $>1.6 \text{ GW}$ production in the third quarter of 2013 at self-reported costs of $\sim \$0.65/\text{W}$, the lowest among all PV technologies [121]. However, further improvements in efficiency are required to lower balance of systems costs and remain competitive with polycrystalline silicon [78]. After stagnating at 16.7% for nearly a decade [79], record device efficiencies have increased over the past few years [81] to the current standard of 20.4% reported by First Solar in March 2014 [122]. Recent increases have been driven primarily by improvement in short circuit current density (J_{SC} , from 26 to 29 mA/cm^2) and fill factor (FF, from 75 to 80%). However the open circuit voltage (V_{OC}) in these champion cells has remained essentially unchanged at $\sim 850 \text{ mV}$, far below the record of 1122 mV achieved in thin film devices employing GaAs [90], which is an absorber with a similar band gap. With J_{SC} and FF values approaching fundamental limits due to advanced front contacts, increasing the V_{OC} offers the greatest potential for further advances [85]. The low V_{OC} in CdTe devices has been attributed to the quality of the CdTe absorber and barriers at the back contact. This paper addresses the latter issue by exploring rapid thermal processing (RTP) to control the activation of a ZnTe:Cu buffer layer at the back contact. The fabrication of CdTe solar cells involves numerous high temperature steps, and RTP offers high throughput capability, reduced thermal budgets, and precision control over time-temperature trajectories. Despite its apparent suitability for CdTe device fabrication there are very limited reports of its use. RTP has been

demonstrated to facilitate grain growth and improve crystallinity of evaporated CdTe [123], but we are unaware of its application to back contact preparation.

It is notoriously difficult to make good ohmic contact with CdTe using conventional metals, because this requires a work function of greater than 5.7 eV [36]. The most common method to solve this problem is by etching the CdTe surface to make its surface heavily p-doped and contacting it with a buffer layer before metallization. Wet chemical etching using solutions such as Br₂/methanol or nitric acid/phosphoric acid mixtures are most common [45]. An alternative preparation is through ion beam milling, which also produces a Te -rich surface [124]. Copper-doped zinc telluride (ZnTe:Cu) is one of the most commonly employed buffer layers [42]. ZnTe was identified due to its valence band alignment and compatibility with CdTe [43, 44]. Copper is commonly used to degenerately dope this layer, which narrows the barrier width and permits electron tunneling, creating a quasi-ohmic contact [45]. First Solar has integrated ZnTe:Cu into its product line, crediting this layer for improvements in both champion cell efficiency and module reliability [84]. Small amounts of copper are also beneficial for doping CdTe [125]. However the free carrier concentration is typically several orders lower than the total Cu concentration, suggesting that significant charge compensation takes place during Cu incorporation [56]. Excessive copper has also been implicated in the formation of deep level defects [58, 126, 127], which have been correlated with reduced carrier lifetimes [124]. Copper is highly mobile [128], and has been observed to preferentially accumulate at both the back contact interface and in the CdS window layer after thermal processing [124, 125, 129]. With copper having both positive and deleterious effects it is critical to precisely control both its amount and spatial distribution in order to obtain high efficiency. The most common approach to apply ZnTe:Cu is through thermal evaporation or sputtering at elevated temperature. A typical process in research laboratories employs temperatures between 240-360 °C, and process times on the order of hours which accounts for sample heating, deposition, and cool down. The amount of copper introduced is controlled by either the target composition (1-5 wt.%) [129], or by using a fixed composition and altering the total thickness of the buffer layer [124]. One drawback of this procedure is that deposition and diffusion occur simultaneously, with substantial diffusion continuing to occur during the subsequent cool down. In this work we have developed an

RTP-based process for back contact preparation that de-couples Cu deposition from its re-distribution. The ZnTe:Cu back contact is co-evaporated at low temperature, with little or no interdiffusion. The sample is then subjected to short RTP treatment(s) to activate the junction. In this work we first describe experimental system and then discuss the optimization of buffer layer composition, thickness, and RTP parameters that resulted in significant efficiency improvements.

3.2 Experimental

Figure 3-1 displays a cross section of the device architecture employed in this work. All devices were processed identically with the exception of the ZnTe:Cu layer. In our experiment, fluorine-doped tin oxide coated glass (TEC-15, Pilkington) was used as the substrate. Substrates were cleaned with detergent (Micro 90), rinsed with DI water, and processed in a UV-ozone furnace prior to device fabrication. First 150 nm thick CdS layer was deposited by thermal evaporation at 150 °C. Then CdTe was deposited by using vapor transport deposition on a substrate at 450 °C and the thickness was about 3-4 μm [34]. The samples were exposed to CdCl₂ in a close space sublimation geometry in a tube furnace at 400 °C for 30 min using a 50%-50% O₂/N₂ ambient. The back surface was etched in a 0.5% Br/CH₃OH solution for 10 s and rinsed with methanol prior to back contact preparation. The ZnTe:Cu buffer layer was deposited by thermal evaporation. Devices with an area of 0.079 cm² were defined by evaporation of 150 nm of Au using a shadow mask.

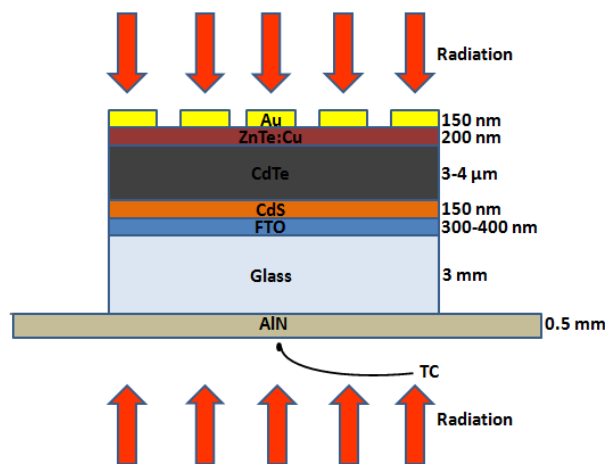


Figure 3-1: Configuration of RTP treatment and device architecture.

After device fabrication samples were subjected to RTP treatments to activate the back contact. Samples were placed on an AlN susceptor as shown inside a commercial RTP unit (RTP-10004, MTI Corporation) in which the samples are exposed to heat lamps on all sides. Under an ambient of Ar the samples were quickly ramped to the desired setpoint and held there for 30 s, at which time the lamps were turned off and the samples returned to ambient under convective cooling. In this work the reported temperatures are from a thermocouple placed in contact with the AlN susceptor (Figure 3-1). The samples were calibrated by attaching temperature indicating labels to the base of the glass superstrate. These record the maximum temperature experienced during the 30 s RTP treatment. Figure 3-2 plots the calibration observed using devices deposited on both 3 mm TEC 15 and 0.7 mm Corning 7059. In both cases the temperature scaled with the setpoint, but the absolute values were consistently lower than the thermocouple which is exposed directly to the incident radiation. Samples deposited 7059 glass were ~ 20 °C cooler than the thermocouple, while the temperatures recorded on TEC15 were ~ 60 °C below the setpoint. The difference is attributed to the greater thermal mass of the TEC15 substrates, suggesting that the glass serves as a heat sink in this system.

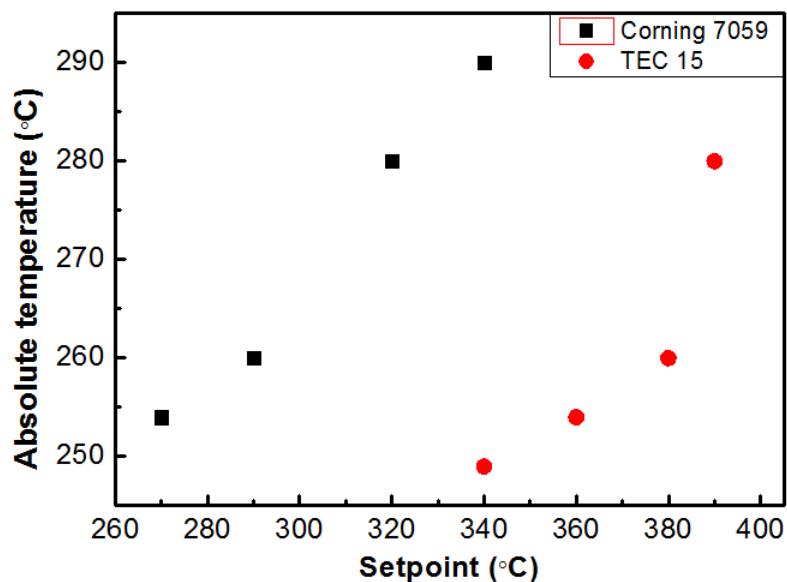


Figure 3-2: Calibration plot of glass temperature recorded from devices deposited both TEC15 and Corning 7059 after 30 s RTP treatments at the thermocouple temperature.

The solar cell performance was measured before and after RTP treatments under simulated AM1.5 using a commercial tool that is calibrated using a silicon standard (PV Measurements). For each sample 6-10 individual devices were measured and they are displayed in box plots. Note that mechanical scribing to minimize current collection from beyond the cell definition isolated the individual devices.

3.3 Results and Discussion

The variables considered were Cu content, the arrangement of Cu during deposition, the total buffer thickness, and the RTP treatment conditions. First, we optimized the Cu content. Buffer layers were deposited by co-evaporation with the ZnTe thickness fixed at 200 nm and variable amounts Cu, with both values determined by quartz crystal microbalance. The QCMs were used for in situ control of the relative amounts ZnTe and Cu deposited, while the absolute values of thickness and composition were determined using transmission electron microscopy and atom probe tomography [110].

Figure 3-3 plots the efficiencies of devices with different contents of Cu after an un-optimized RTP treatment. Without Cu the performance was poor, as expected, and with copper addition a clear optimum was obtained at 3.4 wt.%. This value is quite consistent with amount of Cu in ZnTe sputter targets employed in conventional processing [129]. This value was used in all subsequent experiments.

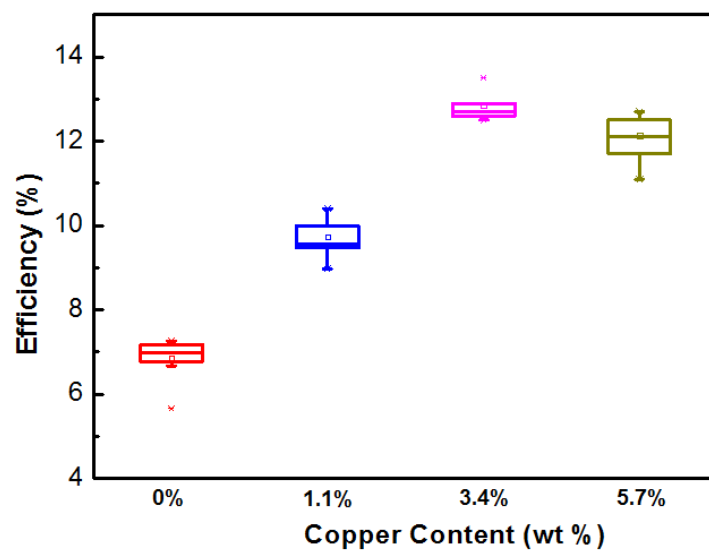


Figure 3-3: Post-RTP device efficiency as a function of Cu thickness.

Figure 3-4 compares device results before and after RTP for ZnTe:Cu buffers with the same overall composition but fabricated through co-evaporation or as bi-layers. Though the differences were not dramatic, the devices produced through co-evaporation show the highest improvement and overall device efficiency, so this configuration was used going forward. Lastly we examined the effect of buffer layer thickness, and as shown in Figure 3-5, there was no significant improvement as the buffer layer thickness was increased. Thus, for all remaining samples the buffer layers were nominally 200 nm in thickness with 3.4 wt.% Cu produced by co-evaporation.

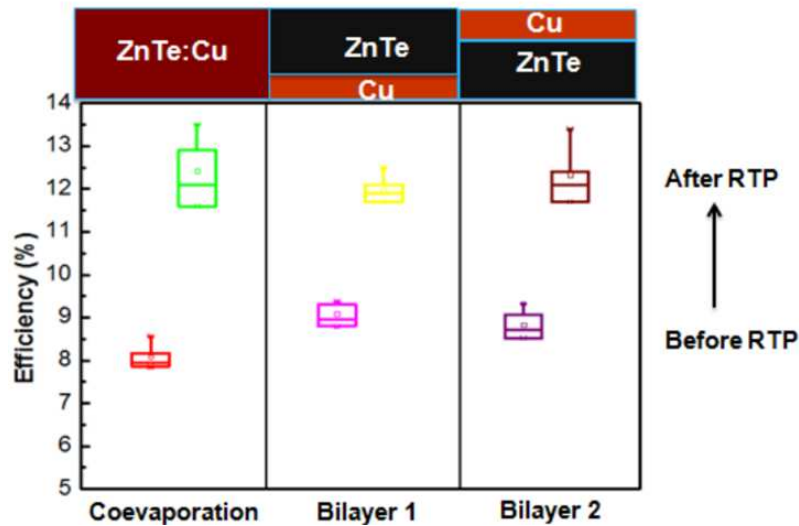


Figure 3-4: Device efficiency before and after RTP for 3 different ZnTe:Cu buffer layer configurations.

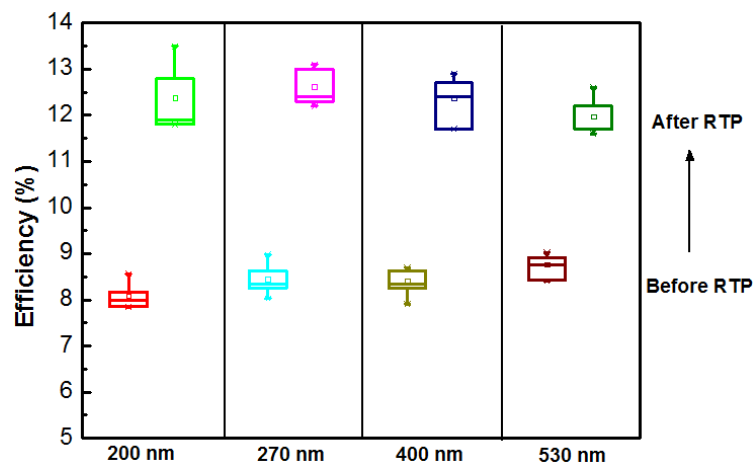
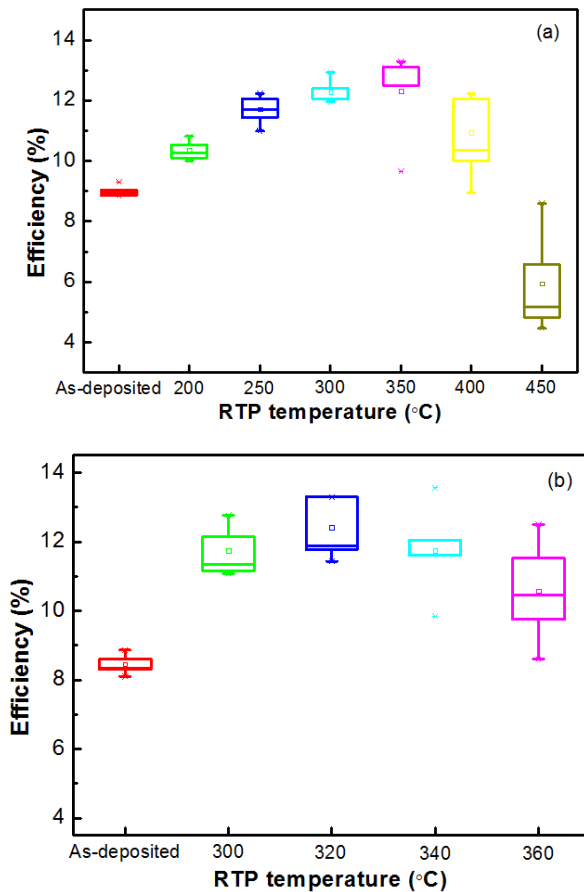


Figure 3-5: Device efficiency before and after RTP as a function of ZnTe:Cu buffer layer thickness.

The process for optimizing the RTP process was as follows. The efficiency of the as-deposited sample was measured, and then that sample was exposed to a series of 30 s RTP treatments at progressively higher temperatures until the devices began to fail. The results are shown in Figure 3-6. In the initial screen the setpoint was ramped in 50 °C increments from 200 to 450 °C. As shown in Figure 3-6 a), the RTP treatment at 200 °C resulted in a little bit increase in efficiency compared to the as-deposited device. With subsequent treatments the device efficiencies improved monotonically until a maxima was obtained at 350 °C, and further treatments at higher temperatures lead to degradation of efficiency. The second sample was exposed to refined set 20 °C steps beginning at 300 °C (Figure 3-6 b). Here devices at 320-340 °C had the highest efficiency. As a final refinement we used a sample in which the first treatment was at 320°C, followed by increasing in 10 °C increments (Figure 3-6 c). The devices produced after exposed to treatments at 320 and 330 °C produced the best results, where the highest efficiency of 14.5% was obtained which marked a 53% increase over untreated samples.



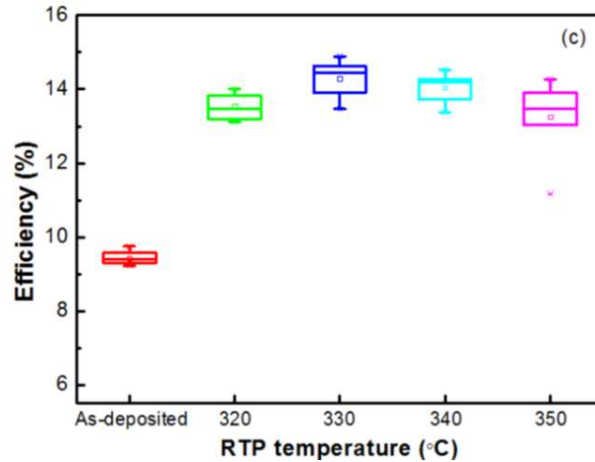


Figure 3-6: Device efficiency during sequential RTP treatments with different temperature steps. (a) 200 - 450 °C using 50 °C increments; (b) 300 – 360 °C using 20 °C increments; (c) 320 – 350 °C using 10 °C increments.

Figure 3-7 shows J-V curves of four representative devices exposed to different RTP treatments, and the detailed parameters are summarized in Table 3-1. The original sample was the as-deposited device which wasn't treated by RTP. The as-deposited device showed good current collection, but the open circuit voltage was only 676.3 mV. In addition, the sample showed significant roll-over, which attributed to the presence of barriers at the back contact [128]. The highest efficiency device was obtained after subsequent RTP treatments at 320/330 °C. In this case the J_{SC} value remains essentially unchanged, but the V_{OC} and FF increase significantly to 826.4 mV and 71.1%, respectively, and the rollover in the J-V was eliminated. Very similar results could also be obtained from devices processed using just one 30 s RTP step, and here it was found that a set point of 360 °C provided optimal results. Finally the device treated at 450 °C is characteristic of overcooked samples. Here all the parameters decreased significantly, and it is inferred that Cu had diffused to the CdS layer, degrading the quality of the junction and leading to shunting.

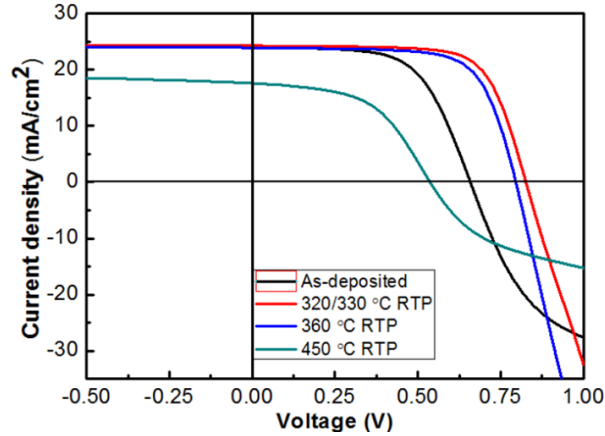


Figure 3-7: J-V curves of devices with different RTP treatments.

Copper migration is a thermally activated process, in which the extent of diffusion is proportional to $(Dt)^{1/2}$, where D is the diffusion coefficient. The temperatures employed in this work are comparable to conventional processing, but the time at temperature is reduced by more than 100X. As such the extent of copper diffusion as expected to be reduced by an order of magnitude. It is expected that this feature would be beneficial for stability. Although formal reliability studies have yet to be performed, we note that devices fabricated using RTP processing 6 months ago display nominally identical performance as they did initially after processing. Studies are underway to fully characterize the extent of Cu redistribution and understand its impact on device performance.

Table 3-1: Summary of the J-V curves from Figure 3-7.

RTP process	Efficiency (%)	FF (%)	Voc (mV)	Jsc (mA/cm²)	R_{shunt} (10⁵/cm²)	R_{series} (Ω/cm²)
As-Deposited	9.1	59.1	676	23.7	2.0	1170
320/330 °C	14.5	71.1	826	24.3	5.1	856
360 °C	13.7	70.5	810	23.9	3.3	770
450 °C	4.9	52.2	537	17.6	0.5	1760

3.4 Conclusion

We have demonstrated that thermal evaporation combined with RTP processing is an effective approach for fabricating back contacts for CdTe solar cells. RTP provides low thermal budgets and precise control over time-temperature trajectories, which is very applicable to CdTe solar cell fabrication. Our work showed that the fraction of Cu in the ZnTe buffer was critical, but its initial distribution or the thickness of the buffer layer was not critical. Sequential RTP treatments were refined to optimize the process. By using appropriate RTP treatments, we increased the efficiency of our device from about 9% to 14.5%, increasing the V_{OC} to >825 mV.

CHAPTER 4

HIGH-EFFICIENCY, FLEXIBLE CDTE SOLAR CELLS ON ULTRA-THIN GLASS SUBSTRATE

This chapter is an adaption of previously published works in Applied Physics Letters [48]. In this paper, we applied our back contact to NREL's absorber on willow glass and got NREL certified flexible CdTe solar cell efficiency.

4.1 Introduction

CdTe solar cells on ultra-thin glass substrates are light and flexible. These traits can enable applications that require high specific power, unique form factors, and low manufacturing costs. The ultra-thin glass can reduce manufacturing costs and increase manufacturing throughput due to its lower thermal mass, which can reduce processing warm-up and cool-down times. It is also possible to produce CdTe solar cells on this glass in a roll-to-roll process. Flexible CdTe solar could be installed as building-integrated photovoltaics or in other configurations that are not amenable to rigid flat-panel installations. Lightweight, flexible solar has significant advantages over conventional technology for applications where specific power is important such as consumer electronics, transportation, remote installations, and military applications.

Flexible CdTe solar cells have been made in both superstrate and substrate configurations [47, 125, 130, 131]. Commercial CdTe modules are made in the superstrate configuration, which has higher efficiency to date. Substrate-configured cells were previously thought to be more amenable to high temperature roll-to-roll processing because they can be made on metal foils. Flexible superstrate cells have been made using DuPont clear Kapton and flexible Corning Willow glass. Flexible substrate cells have been made on metal foils [132]. Efficiencies reaching 14% and 11.5% have been reported for flexible CdTe solar cells in a superstrate and substrate configuration, respectively [125, 130]. Here, we focus on flexible CdTe superstrate cells made on ultra-thin glass.

Our previously reported flexible device with 14.05% certified efficiency had a CdS window layer deposited by chemical-bath deposition (CBD) and sputtered ZnTe:Cu/Ti back contact [130]. The 16.4% device reported here uses a sputtered CdS:O window layer coupled with an evaporated and rapidly processed ZnTe:Cu/Au back contact. The CdTe layer is nominally identical for both devices. By replacing the CBD CdS with an oxygenated CdS:O sputter process, we were able to improve the uniformity of the window layer and ultimately increase short circuit current density (J_{sc}). The sputtered ZnTe:Cu/Ti back contact we used in our earlier work was replaced by a co-evaporated ZnTe:Cu back contact followed by rapid thermal processing (RTP), leading to higher open circuit voltage (V_{oc}) and Fill Factor (FF) values.

4.2 Materials and Methods

All Willow glass substrates used in this work were pre-cut to 100 μm x 38.1 mm x 38.1mm and used as received from Corning. Bilayers of SnO₂:F (FTO) and undoped SnO₂ (TO) transparent conducting oxides (TCOs) were deposited by metal-organic chemical vapor deposition (MOCVD) at a substrate temperature of 550 °C. The bilayer film had a sheet resistance of approximately 13 Ω/sq , measured by a collinear 4-point probe. The CdS:O layer was reactively r.f.-sputtered at room temperature using a hot-pressed stoichiometric CdS target. As determined by Meysing *et al.*, the optimum sputtering ambient was Ar with 6 vol.% oxygen at a pressure of 10 mTorr [27]. The resulting film demonstrated an as-deposited optical band gap of 2.8 eV. The thickness of the CdS:O layer was approximately 100 nm, as measured with a stylus profilometer (VeecoDektak 8). The CdTe layer was deposited by close-spaced sublimation (CSS) with the glass substrate maintained at 600 °C and the CdTe source plate maintained at 660 °C for 2.5 min. The device stack was vapor CdCl₂ treated by CSS at 400 °C for 10 min. Contact pre-etching was performed using a 0.05% bromine/methanol etch for 20 s. The ZnTe:Cu back contact layer was deposited by co-evaporation from ZnTe and Cu, followed by Au, onto an unheated substrate. The contact area was defined by evaporating gold through a metal mask, followed by hand scribing with a razor blade to remove the active region around each Au contact [65].

4.3 Results and Discussion

Following the back contact deposition, the samples underwent three separate RTP treatments of 30 s at 280 °C, 290 °C, and 300 °C, with device characterization performed between each heat treatment. RTP treatment at 300 °C gave the optimal performance. Current density-voltage (J-V) performance was measured using a solar simulator (Oriel 91193, Class ABA) that was adjusted to closely simulate AM1.5 response of a CdS/CdTe cell. The best cells were then re-measured under standard conditions by the device performance and measurements group at the National Renewable Energy Laboratory (NREL) to yield a certified efficiency (see Figure 4-1). Prior to this certification, a 100 nm MgF₂ antireflection layer was deposited by thermal evaporation. The device area was precisely defined by an aperture for these measurements. A comparison of the device parameters for the 16.4% device with our previously reported 14.05% device is shown in Table 4-1. This efficiency of 16.4% is the highest reported for any flexible CdTe solar cell. The 16.4% device shows improvement in all device parameters compared to the 14% cell. The evaporated ZnTe:Cu back contact process significantly increases the FF.

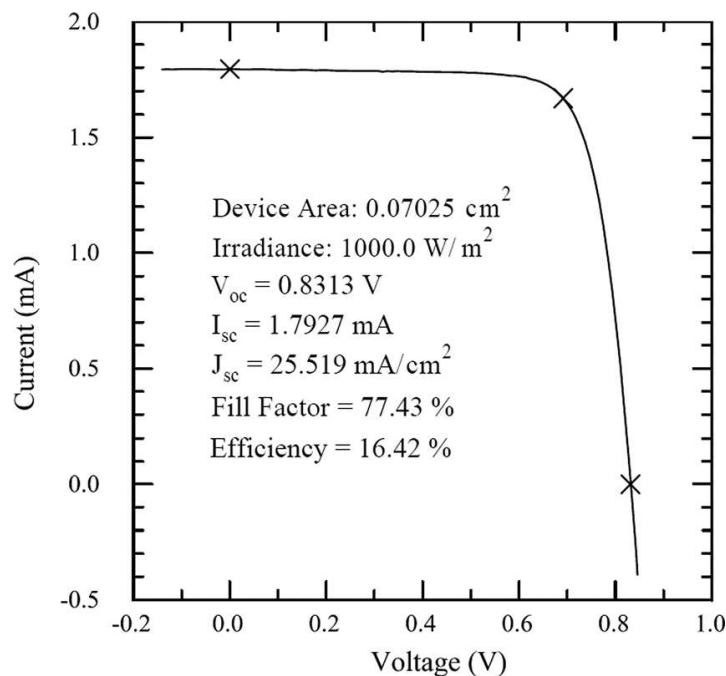


Figure 4-1: NREL-certified 16.4% flexible CdTe solar cell on Willow glass.

Table 4-1: Comparison of the device parameters for both certified devices.

Device	V _{oc} (mV)	J _{sc} (mA/cm ²)	FF (%)	Efficiency (%)
14% exp	822	24.3	70.3	14.1
16% exp	831	25.5	77.4	16.4

Figure 4-2 compares the absolute quantum efficiency (QE) measurements of the 16.4% device with the previous best 14.05% device. The device with the sputtered CdS:O has a noticeably higher blue QE than the device with the CBD CdS. As calculated from the integrated QE, the increased transmission due to sputtered CdS:O (i.e., from 300 to 500 nm) should contribute 1.1 mA/cm² higher J_{sc}. The slightly lower QE around 600-700 nm is likely due to a thicker (250 nm vs. 450 nm) SnO₂:F layer used in the device with sputtered CdS:O. We note that the sputtered CdS:O films also have much better uniformity than the chemical bath process, leading to an average efficiency of 15.3% over the 16 pixels on this substrate.

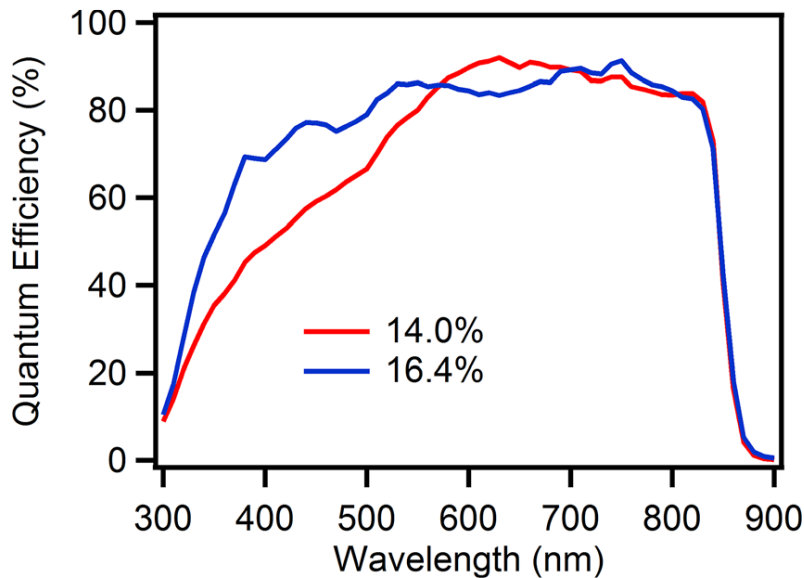


Figure 4-2: Comparison of absolute QE measurements of the 14.05% device and the 16.4% device.

Figure 4-3 compares the extracted net acceptor density (N_A) vs. depletion width (w) for two representative devices with sputtered and co-evaporated/RTP-treated back contacts. These devices were processed identically to the certified devices and had similar performance. Carrier density was measured at the zero bias point as indicated in Figure 4-3. Devices with

co-evaporated ZnTe:Cu back contact have a carrier density of $4.3 \times 10^{14} \text{ cm}^{-3}$ and a depletion width of $1.25 \text{ }\mu\text{m}$ at the zero bias point. Devices with sputtered ZnTe:Cu back contact have a carrier density of $1.8 \times 10^{14} \text{ cm}^{-3}$ and a depletion width of $2.15 \text{ }\mu\text{m}$ at the zero bias point [87]. This shows that the carrier density is higher for the devices with the co-evaporated ZnTe:Cu back contact. It should be noted that the devices shown in Figure 4-3 were processed identically to the certified 14.05% and 16.4% devices and had similar performance. Both C-V profiles have the U-shape characteristic of CdS/CdTe devices [129].

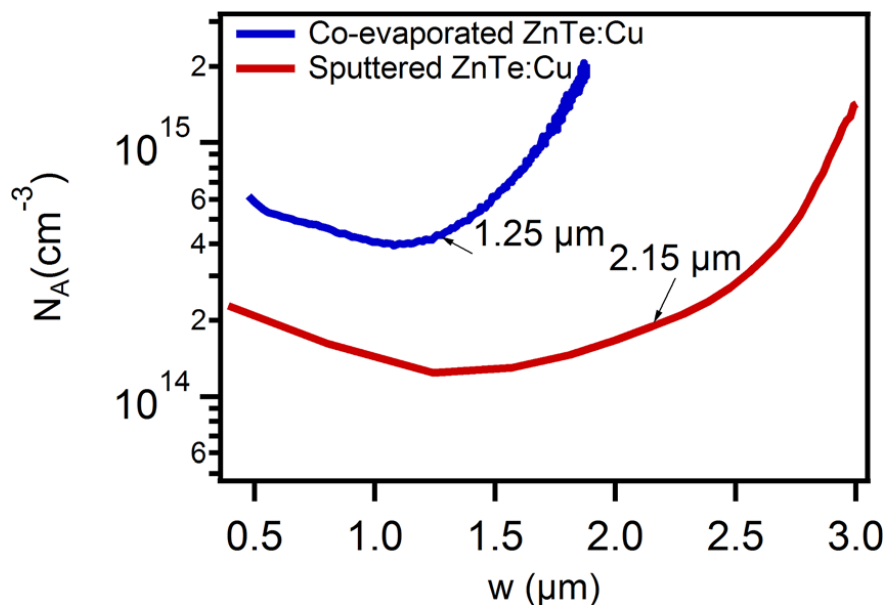


Figure 4-3: Acceptor density profiles extracted from the C-V data for the devices with evaporated ZnTe:Cu and sputtered ZnTe:Cu back contacts. The arrows indicate the zero bias point at which the depletion width is indicated.

The differences in V_{OC} and FF between the two ZnTe:Cu contacting processes could be due to differences in temperature profiles, which would alter Cu diffusion. For example, higher-temperature RTP annealing for very short times would yield a different diffusion profile than the longer duration of lower temperatures for the sputtered contact. The energetics of the processes also varies. Sputtering produces high-energy ions, which impinge on the surface and result in additional surface damage compared to a thermal evaporation process. RTP and high-temperature sputtering would also affect the ability of the surface to reconstruct as well. A combination of all of these processes likely contributes to the difference in net acceptor density between the two contacts.

Considering thermal differences first, the sputter process includes a 2-h pre-heat step at 300 °C and maintains that temperature throughout the hour-long ZnTe:Cu deposition. In the RTP, the samples are at the maximum annealing temperature for only about 30 s. Furthermore, in contrast to the long heat-up and arbitrary cool-down times for sputtering, RTP has precisely controlled time and temperature profiles. Li *et al.*, used quantitative analysis of secondary ion mass spectrometry (SIMS) to show that the majority of Cu segregates to the outer Au metallization layer, and that the ZnTe interface layer appears to limit the Cu out-diffusion into CdTe during the RTP [65]. The longer heating step used with the sputtered ZnTe:Cu process tends to generate Cu profiles that look more like those from an “overheated” RTP-processed device. Both SIMS profiles show similar Cu concentrations in the $10^{17}/\text{cm}^3$ range in the CdTe layer, so higher carrier densities in evaporated devices may indicate better activation due to RTP.

Considering kinetic differences between the two contacting processes, the absence of ion bombardment of the CdTe surface during evaporation could be expected to lead to fewer defects at the CdTe and ZnTe:Cu interface. To investigate this possibility, time-resolved photoluminescence (TRPL) measurements were used to determine carrier lifetimes (s) in the two devices used for C-V measurements. The carrier lifetime extracted from TRPL was about 1.2 ns in devices made with both types of back contacts. This suggests that even though the process difference may cause differences in recombination at the back surface, either these differences are not significant or minority carriers are not reaching the back surface in sufficient density to cause an observable difference in lifetime. To investigate this further, we used SCAPS modeling to simulate the effect of varying carrier density and τ [133].

Using numerical simulations, Kanevce and Gessert have shown how the hole density and minority carrier lifetime can couple together to affect V_{OC} and FF [134]. We used SCAPS simulations to investigate the dependence of V_{OC} and FF on carrier density. The full set of parameters used in the simulations is shown in Table 4-2. These parameters were chosen from the literature [85, 135]. The simulated J-V curves in Figure 4-4a show increases in V_{OC} with carrier density at a constant lifetime. FF also increases with carrier density but saturates at higher carrier density. As the carrier density increases, the space-charge region (SCR) narrows. For carrier densities of 10^{15}cm^{-3} and above, the number of carriers generated outside

of the SCR is not negligible [134]. These carriers need to rely on diffusion to get collected. Therefore, FF saturates and eventually decreases for higher carrier densities with a constant lifetime. We also simulated the effect of increasing the carrier lifetime at the measured carrier densities. Increasing the lifetime would lead to even higher V_{oc} and FF values than we measured here. This suggests that further improvements to the back contact interface to reduce surface recombination would lead to increased efficiency.

Table 4-2: Parameters used in the SCAPS model.

Layer	CdTe	CdS	i-SnO ₂	SnO ₂ :F
Mobility (cm ² /V s) h/e	80/320	25/100	25/100	7.5/30
N _a /N _d (1/cm ³)	2×10^{14}	1×10^{17}	1×10^{18}	5×10^{20}
Bandgap (eV)	1.5	2.4	3.6	3.6
Electron affinity (eV)	4.4	4.5	4.7	4.8
Defect density (1/cm ³)	2×10^{13}	1×10^{16}	1×10^{15}	1×10^{15}
Lifetime (ns) h/e	1.00/1.00	0.01/0.01	0.1/100	0.1/100
Conduction band density of states (1/cm ³)	8.0×10^{17}	2.3×10^{18}	3.2×10^{18}	3.2×10^{18}
Valence band density of states (1/cm ³)	2.2×10^{19}	1.7×10^{19}	2.5×10^{19}	2.5×10^{19}
Thickness (μm)	4	0.07	0.1	0.3
e/h thermal velocity (cm/s)	1×10^7	1×10^7	1×10^7	1×10^7
Dielectric permittivity	10.2	9	9	9

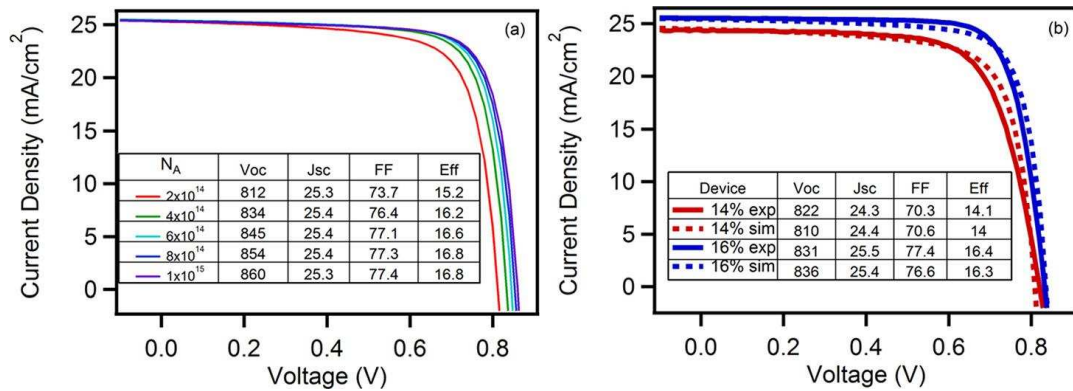


Figure 4-4: a) Simulation of J-V curves with increased carrier density. b) Comparison of certified devices with SCAPS simulations.

Figure 4-4b compares the device parameters for both certified devices with the SCAPS simulation. Experimentally determined carrier densities (Figure 4-3) of $1.8 \times 10^{14} \text{ cm}^{-3}$ and $4.3 \times 10^{14} \text{ cm}^{-3}$ were used for device simulations, respectively. The simulation predicts a negligible change in J_{sc} for this range of carrier densities. J_{sc} would also decrease for higher carrier densities, which can be explained following the same arguments for FF. Simulated results of increasing carrier lifetime at the measured carrier densities also show negligible

changes in J_{SC} for this range of carrier densities. Negligible changes in J_{SC} within the experimentally observed carrier densities and lifetime support the assignment of the increased J_{SC} to CdS:O as previously mentioned. The integrated QE (Figure 4-2) showed that the contribution from the increased transmission of CdS:O is 1.1 mA/cm². To reflect this difference in the simulations, the CdS thickness was reduced from 100 nm to 70 nm in the simulations, respectively. Varying the CdS layer thickness to reflect the differences in the CdS:O absorption is a simplification required in order to use the basic SCAPS model. A comparison of the experimental and simulated values is tabulated in the inset table along with the respective J-V curves in Figure 4-4b. The trends in simulation results agree well with the trends in the experimental data.

4.4 Summary and Conclusions

There are relatively few reports of flexible CdTe devices in the literature, and therefore, many questions about their potential stability and mechanical robustness. In the previous work, we showed that the efficiency of flexible CdTe devices does not change significantly under static bend testing [130]. We have also conducted dynamic bend testing of TCO films on Corning VR Willow VR glass as there are few reports on the flexibility of high temperature TCOs used in CdTe. Burst *et al.* flex-tested indium doped tin oxide (ITO) to 25-50 k bend cycles without breakage and with ~0.1% change in sheet resistance [136]. Dynamic bending stability studies for complete devices on flexible Corning Willow glass are planned for future studies. We have performed shelf life tests of similarly processed device stacks on rigid Corning 7059 glass and have seen minimal changes over the course of 330 days (see Figure S1 in supplementary material) [137]. First Solar recently demonstrated ZnTe-based back contact increases robustness against thermal and bias-driven power degradation [84]. These results indicate that this device structure on flexible glass should be stable and reliable.

This work was supported by the U.S. Department of Energy through the Sun Shot Foundational Program to Advance Cell Efficiency (F-PACE) under Contract No.DE-AC36-08-GO28308. J. D. Beach and J. Li were supported by the Bay Area Photovoltaic Consortium.

CHAPTER 5

CONTROLLED ACTIVATION OF ZNTE:CU CONTACTED CDTE SOLAR CELLS USING RAPID THERMAL PROCESSING

This chapter is an adaption of previously published works in Solar Energy Materials and Solar Cells [65].

5.1 Introduction

A notorious challenge for CdTe solar cell technology is the formation of high quality ohmic back contacts [138]. The large electron affinity of CdTe coupled with its inability to be highly doped leads to the formation of a Schottky barrier when contacted directly with a metal.

Consequences of such barriers involve loss of open circuit voltage (V_{OC}) and fill factor (FF), which are often manifested by the presence of roll over behavior in J-V curves [139]. A common strategy to address this problem is through the insertion of a thin interfacial layer between the CdTe and metal contact [132]. One such buffer layer is Cu_xTe ($1 < x < 2$), which may be formed by the deposition of Cu followed by thermal treatments. Such contacts reduce the series resistance and have resulted in high efficiency devices [18, 79], but copper migration to the front contact can lead to shunting and loss of efficiency [128, 140]. Another commonly used buffer layer is copper doped zinc telluride (ZnTe:Cu), where the copper doping level is in the range of 1-5 wt.% [42]. ZnTe is chemically compatible with CdTe and offers a number of advantages. First, its valence band maximum is well aligned with that of CdTe, facilitating hole collection [44]. With a band gap of the ~ 2.2 eV ZnTe also provides a back contact reflector for electrons which is proposed to reduce recombination at the back contact, particularly in thin or fully depleted device structures [85]. Lastly, ZnTe can be highly doped ($> 10^{20} \text{ cm}^{-3}$) [141] to provide an effective tunnel junction to the metal layer [45]. First Solar recently revealed that it has integrated a ZnTe buffer into its current product line, crediting this layer for recent improvements in both champion cell efficiency and

module reliability [142].

As most commonly practiced, ZnTe:Cu layers are deposited by sputtering at elevated temperature (240–360 °C) in processes whose duration are on the order of hours [124, 129]. The amount of copper is controlled by varying the composition of the sputter target or the layer thickness. It is well known that copper is a fast diffuser, with reported coefficients of $\sim 10^{-9}$ cm²/s at the temperatures employed [143][144]. In addition to limiting throughput, another drawback of this procedure is that deposition and diffusion occur simultaneously, making process control difficult and resulting in copper migration throughout the device [129]. In bulk CdTe a very small amount of copper may be beneficial [125, 145], however excessive amounts lead to deep level defects and recombination centers [52, 58, 127].

In this paper we describe a new process in which deposition and activation of ZnTe:Cu are decoupled. The ZnTe:Cu buffer and Au metallization layers are first deposited by evaporation at low temperature, followed by rapid thermal processing (RTP) to precisely control activation. Despite RTP's apparent suitability for CdTe device fabrication there are very limited reports of its use. RTP has been demonstrated to facilitate grain growth and improve crystallinity of evaporated CdTe [123], but we are unaware of its application in back contact preparation. RTP offers a number of important advantages for this purpose. First, it is expected that high temperature-short time processes should be selective to Cu activation over diffusion based on energetics. The diffusion process is weakly activated, with reported activation energies of 0.3-0.7 eV [146][144, 147]. In contrast, the enthalpies of formation for copper doping states range from 1.5-2.5 eV [54]. Second, RTP offers high throughput and precise control over time-temperature trajectories. Lastly, the low thermal budgets involved should not disturb the optimization of preceding processes used in front contact formation or absorber deposition, making this process easily adaptable to multiple device fabrication platforms.

In this work the dramatic improvements in device performance afforded by this RTP process are quantified and interpreted through measurements of current-voltage (J-V), quantum efficiency (QE), carrier density (N_A) and minority carrier lifetime (τ). The redistribution of copper during RTP is examined using secondary ion mass spectrometry (SIMS) and atom probe tomography (APT). SIMS is used to quantify the extent of Cu

diffusion into the CdTe absorber while APT is employed to characterize the back contact region with nanoscale resolution. These measurements are combined to postulate the changes in band structure that occur in the back contact region under optimal process conditions.

5.2 Materials and Methods

5.2.1 Device Fabrication

Devices were fabricated using two different superstrate/front contact combinations to demonstrate the flexibility of the RTP back contact process. The first employed fluorine-doped tin oxide coated glass (TEC-15, Pilkington) that was coated with 150 nm of CdS deposited by thermal evaporation at 150 °C. The second superstrate consisted of Corning 7059 glass coated with a SnO₂:F (FTO)/SnO₂ (TO) transparent conductive oxide (TCO) bilayers deposited by metal-organic chemical vapor deposition followed by 100 nm of CdS:O deposited by reactive sputtering at room temperature [148]. The remaining processing was identical. For all devices a ~3 micron CdTe absorber layer was grown by vapor transport deposition at $T = 450\text{ °C}$ [34]. The samples were exposed to CdCl₂ in a close spaced sublimation geometry in a tube furnace at 400 °C for 30 min using a 50%-50% O₂/N₂ ambient. The back surface was etched in a 0.5% (v/v) Br/CH₃OH solution for 10 s and rinsed with methanol prior to back contact preparation. A 200 nm ZnTe:Cu buffer layer was deposited by thermal co-evaporation. Quartz crystal monitors (QCM) were used to control the evaporation rates of both sources, and the total copper content was 3.4 wt.%. Devices with an area of 0.079 cm² were defined by evaporation of 150 nm of Au using a shadow mask. Individual devices were isolated by scribing along the perimeter of the Au through the semiconductors down to the transparent conductor. After device fabrication, samples were subjected to 30 s RTP treatments under flowing Ar to activate the back contact. Further details on the optimization of buffer layer composition and RTP process conditions are provided in the literature [20].

5.2.2 Device Characterization

The solar cell performance was measured under simulated AM1.5 radiation using a commercial tool that is calibrated using a certified silicon standard (PV Measurements).

Quantum efficiency (QE) was measured on a custom system with a grating monochromator and lock-in amplifier detection. For these measurements no intentional white light bias is added to the mechanically chopped monochromatic light. Results are calibrated by comparison to a NREL-measured standard silicon solar cell. Capacitance Voltage (CV) was measured on an Agilent HP4284A precision LCR meter controlled by Labview at 100 kHz and with a 10 mV AC signal. Time resolved photoluminescence (TRPL) measurements used to determine minority carrier lifetime were performed at the National Renewable Energy Laboratory (NREL) using 650 nm pulsed laser excitation [108]. Dynamic SIMS was performed using an ION-TOF Model IV, and the copper density was quantified by normalizing the measured Cu/Te ratio to the copper content in the as-deposited sample which was quantified by APT. APT analyses were performed on a Cameca LEAP 4000X Si local electrode atom probe instrument using parameters optimized for quantitative evaluation of these materials [110]. Additionally, transmission electron microscopy (TEM) images before and after APT analyses were acquired with a Philips CM200 TEM using a holder specifically designed for imaging APT specimens [149].

5.3 Results

5.3.1 Opto-electronic Properties

The CdTe cells used in these studies were fabricated using the conventional superstrate architecture as detailed in the experimental section. Throughout this work comparisons are made among sets of three devices in which the fabrication steps were identical with the exception of the RTP treatment applied after back contact formation. “As-deposited” samples refer to devices that were contacted with a ZnT:Cu|Au bilayer, but not subjected to RTP annealing. “Optimal” samples were subjected to a 30 s RTP treatment at an optimized setpoint temperature that was 300-340 °C depending on the specific superstrate employed. “Overheated” samples received an additional 30 s RTP treatment at slightly elevated temperature.

Figure 5-1a provides box plots comparing the efficiency obtained from 8-10 devices in the as-deposited state, after an optimal RTP treatment, and a sample that was overheated. Figure 5-1b provides representative J-V curves from this set of devices and the associated

device parameters are summarized in Table 5-1. For these samples, which employed the Corning 7059 front contact, the optimal RTP treatment consisted of a single 30 s treatment at a setpoint temperature of 300°C. The overheated sample was exposed to an additional 30 s treatment at 320 °C. Note that nominally identical results were observed for devices employing the TEC15/CdS front contact [20]. The as-deposited device showed good current collection, but the efficiency was just 10% due to the low open circuit voltage of just 636 mV. After the optimal RTP treatment there were significant improvements in both V_{OC} (852 mV) and FF (73.7%) that are consistent with the elimination of back contact barriers. The J_{SC} value remains essentially unchanged, and thus the overall efficiency was elevated to 15.3%. After receiving the second 30 s RTP treatment the efficiency was greatly attenuated (8.9%), with losses in V_{OC} , FF, and J_{SC} . The significant decrease in J_{SC} could be attributed to the presence of excess Cu in the CdTe that form defects that serve as recombination centers. Another possibility is shunting, which is commonly observed when significant Cu has diffused to the CdS layer, thus degrading the quality of the hetero junction. These possibilities are discussed below.

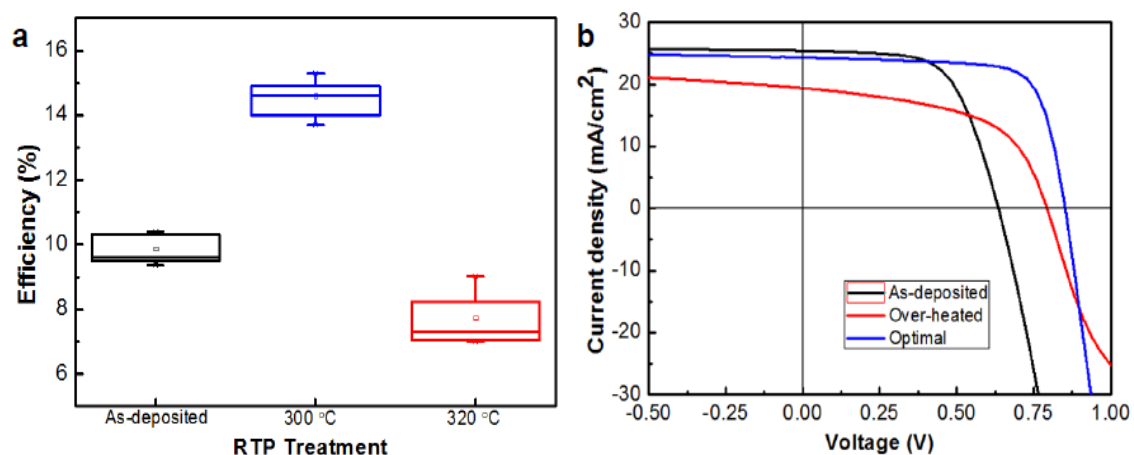
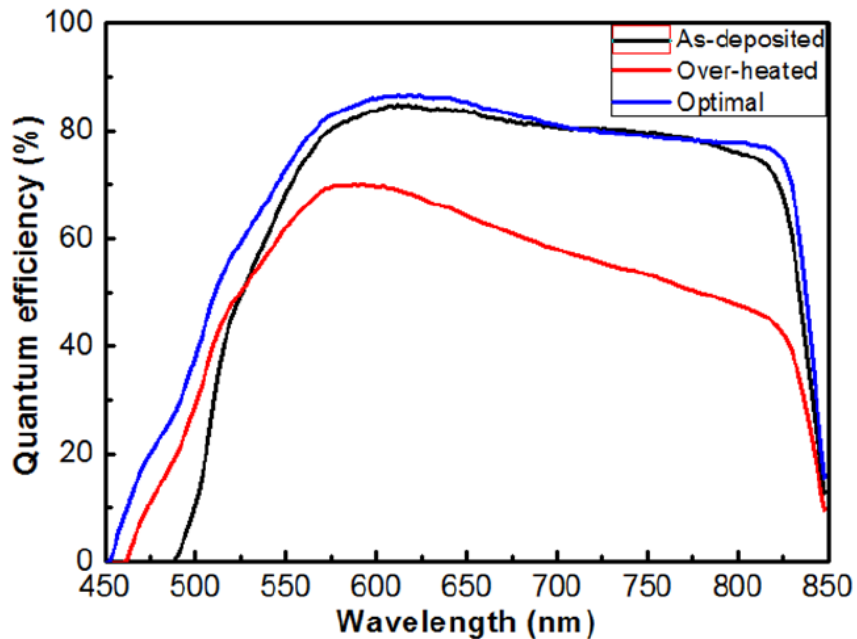


Figure 5-1: Influence of RTP treatment on a) device efficiency as shown in a box plots based on 8-10 devices at each condition. 50% of the measurements fall within the box, while the position of the error bars reflect the maximum and minimum obtained from each sample. b) J-V curves representative of ZnTe:Cu contacted devices in the as-deposited state, after optimal RTP treatment, and overheated.

Table 5-1: Summary of device parameters in the three states.

Sample	Voc (mV)	Jsc (mA/cm ²)	FF (%)	Efficiency (%)
As-deposited	636	25.4	62.2	10.0
Optimal	852	24.3	73.7	15.3
Overheated	793	19.4	54	8.3

Measurements of quantum efficiency, carrier density and lifetime are consistent with the J-V behavior. Figure 5-2 compares the QE response obtained from devices prepared in the as-deposited, optimal, and overheated states. The QE of the as-deposited and optimally processed devices were quite similar as would be expected from their J_{SC} values, showing that the optimal RTP treatment does not significantly impact the properties of the front contact or the CdTe absorber. In contrast, excessive heating is deleterious to current collection throughout the visible spectrum. In particular, significant QE loss is observed in the red portion of the spectrum, behavior which has previously been correlated with copper content and ascribed to related defects that cause voltage-dependent collection [150].

**Figure 5-2:** Comparison of external quantum efficiency spectra for the 3 representative devices.

The carrier density (N_A) profile as a function of the depletion width (W) is calculated by:

$$N_A(W) = \frac{2}{q\varepsilon} \left[\frac{d(1/C^2)}{dV} \right]^{-1} \quad (5-1)$$

where $W = \varepsilon/C$, q is the elemental charge, ε is the permittivity, C is the specific capacitance, and V is the bias voltage. Figure 5-3a compares the carrier density profile for the as-deposited and optimally processed samples. The overheated sample displayed very high leakage current, providing unreasonable results and as such was excluded from this comparison. Both of the remaining samples display U-shape profiles characteristic of CdTe/CdS solar cells [151]. The carrier concentrations were estimated from the bases of these curves to avoid the complications that can occur at both forward and reverse bias. The results are somewhat surprising, in that the apparent acceptor density actually declined after optimal RTP treatment from 10^{14} to $4 \times 10^{13} \text{ cm}^{-3}$. However these changes are small, and suggest that the observed device improvements are not due to copper doping of the CdTe.

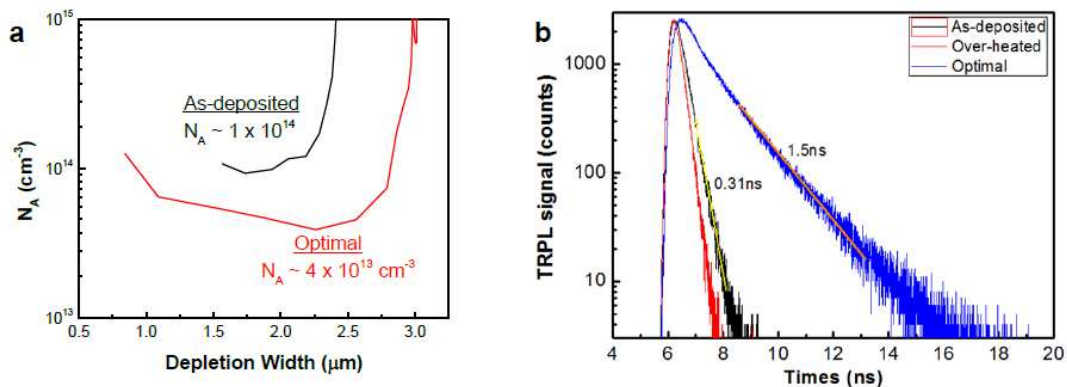


Figure 5-3: a) Net acceptor density, N_A vs. depletion width, W , as derived from C-V measurements for the as-deposited device and after optimal RTP treatment; b) Comparison of TRPL measurements of minority carrier lifetime from three representative devices.

Figure 5-3b compares TRPL measurements which were used to extract minority carrier lifetimes (τ) for these samples. After optimal RTP treatment, τ jumped by a factor of five from 0.3 ns in the as-deposited sample to 1.5 ns. With excessive heating τ declined to values less than the as-deposited case. Open circuit voltage has been strongly correlated with lifetime [152], although the underlying reasons for this relationship are not fully understood. For devices contacted with Cu_xTe it was observed that lifetimes declined with increasing

copper, which was attributed to the formation of defects in the bulk or near the CdS/CdTe heterojunction that serve as recombination centers [150]. In contrast, for devices contacted with ZnTe:Cu lifetimes increased to an optimal value that was a strong function of contacting temperature [124], not dissimilar from the behavior observed here. Recently it has been shown that 1 photon TRPL using excitation above the band gap may be more sensitive to surface than bulk recombination, particularly in thin film devices [153]. The addition of buffer layers is expected to introduce interface defect states that can create dipole layers [132]. The resulting fields would oppose the built-in field associated with the junction, and thus their removal by post-deposition processes such as RTP would increase the energy of collected carriers. An optimally formed ZnTe:Cu back contact will also have a large conduction band offset at the CdTe|ZnTe interface, creating an electron reflector that keeps electrons from getting to the ZnTe|metal interface. It is postulated that the large increase in τ and V_{oc} observed under optimal RTP conditions is due to modification or passivation of these interface states, and an associated reduction in recombination and barriers in the back contact region.

5.3.2 Copper Distribution

5.3.2.1 Secondary Ion Mass Spectrometry

To better understand how copper migration may be influencing the results described above, its distribution was measured using SIMS and APT using a set of TEC15/CdS based devices. The former provides an averaged 1D profile throughout the device structure, while APT was used to create 3D reconstructions of the structure and elemental distribution in the back contact region. Figure 5-4 displays SIMS profiles confirming systematic variation in Cu diffusion into the CdTe layer as a result of RTP treatment. The as-deposited case shows that copper is uniformly distributed through the ZnTe layer in a step profile as expected. Upon RTP treatment copper diffuses out of the ZnTe layer into both the CdTe absorber as well as into the gold contact (the first ~150 nm of the depth profile). The latter is not surprising since copper and gold form completely miscible solid solutions. Also as expected, successive RTP treatments further deplete the ZnTe layer and increase the extent of copper diffusion into the device. For the optimal device Cu extends ~1 μm into the CdTe before

falling below the sensitivity limit of the instrument. The overheated sample displays higher Cu levels in the CdTe, and there is also some evidence of copper accumulation in the CdS layer, which would be consistent with the shunting behavior observed in those devices (Figure 5-1b).

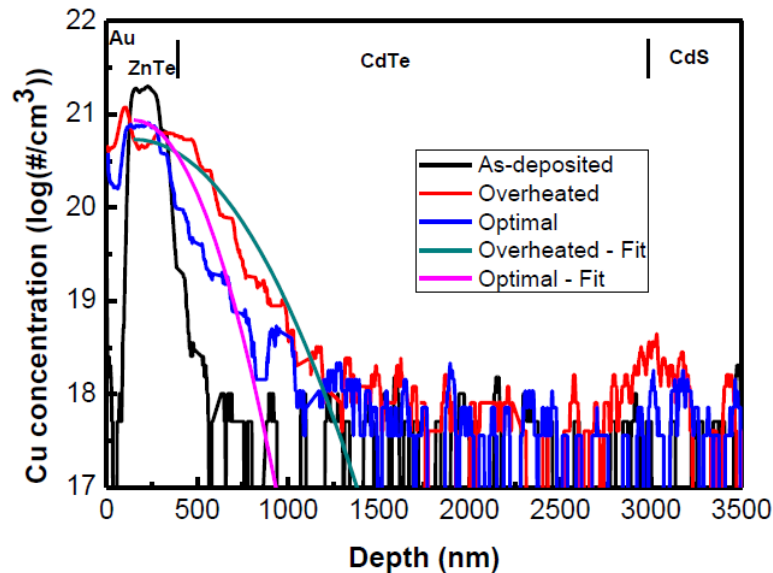


Figure 5-4: Quantified SIMS depth profiles of Cu concentration from the Au/ZnTe:Cu/CdTe/CdS devices considered in this work. The smooth curves through the RTP samples are solutions to Fick’s law using Eq. (5-2).

The smooth curves running through the data are Gaussian profiles that are the solutions to Fick’s second law, approximating the initial Cu distribution as a delta function:

$$C(x, t) = \frac{Q_T}{\sqrt{\pi Dt}} \exp\left(\frac{-x^2}{4Dt}\right) \quad (5-2)$$

where the two adjustable parameters are the initial dose, Q_T , and a characteristic diffusion length Dt . For both profiles the dose was fixed at $Q_T = 2 \times 10^{16} \text{ cm}^{-2}$ and the diffusion lengths were 0.13 and 0.21 μm for the optimal and overheated samples, respectively. These simple analytical solutions do a relatively good job of modeling the experimental profiles, and the parameters employed provide insight into the processes that are occurring. The total dose of copper provided in the as-deposited ZnTe:Cu layer was $1 \times 10^{17} \text{ cm}^{-2}$. The lower value of $2 \times 10^{16} \text{ cm}^{-2}$ that was found to best fit both diffusion profiles reflects the fact that a significant fraction, perhaps the majority, of copper provided in the buffer layer accumulates in the gold contact. Based on the RTP times employed one extracts diffusion coefficients that are on the

order of 5×10^{-12} cm²/s. These are surprisingly low values, and using the Arrhenius relationships for copper diffusion coefficients available in the literature [144, 154] it would suggest that the temperature of the sample was ~ 150 °C, significantly below the nominal RTP setpoint recorded by a thermocouple in contact with the susceptor. This contradicts evidence that suggest that during RTP processing the effective temperature of the CdTe layer is actually hotter than the value recorded by the thermocouple in contact with the AlN susceptor. At the short time scales involved radiation is selectively absorbed in the CdTe layer with the glass superstrate and AlN susceptor serving as heat sinks. Evidence in support of this hypothesis comes from our observation that the RTP temperature setpoint must be reduced in order to achieve optimal performance when the thickness of the glass superstrate is reduced or when devices are intentionally placed in poor thermal contact with the susceptor. Assuming the CdTe layer is at temperature greater than equal to that recorded by the thermocouple these results suggest that barriers at the ZnTe interface may inhibit Cu diffusion into the CdTe, accounting for the low effective diffusion coefficients observed. Such behavior would be consistent with recent reports of improved reliability with the use of ZnTe buffer layers [155].

5.3.2.2 Atom Probe Tomography

SIMS is very useful for providing an overview of the distribution throughout the device, but it provides profiles that are radially averaged due to the sputtering spot size. Atom probe tomography has been demonstrated to be a powerful tool for characterizing polycrystalline solar cells [156], and in particular its 3D capability has been recently deployed to characterize the segregation of impurities at the grain boundaries in CdTe devices [157]. Here we apply APT to characterize the structure and composition of the three representative samples as shown in Figure 5-5. Each of these figures includes a TEM image of the sample before APT, the resulting elemental reconstruction, and volume averaged 1D concentration profiles down the tip axis, which was approximately orthogonal to the layers. The original samples prepared by FIB contained a small portion of the Au contact (~ 5 - 10 nm) at the apex, but this layer popped off during specimen turn on, likely due to the lower evaporation field for ZnTe than for Au. Therefore, zero on the x axis of the concentration profiles corresponds to the Au|ZnTe interface. In the APT images Cd is represented as black, Zn is grey, Cu is orange, and Te is

excluded for clarity. Note that the images provided in Figure 5-5 are just 2D representations of the full 3D reconstructions. Videos displaying the full 3D elemental distributions for these samples are provided in the supplementary information. A sharp ZnTe|CdTe interface is observed in all samples, demarked by the grey/black border. Significant heterogeneity in the copper distribution is observed in all samples as discussed below.

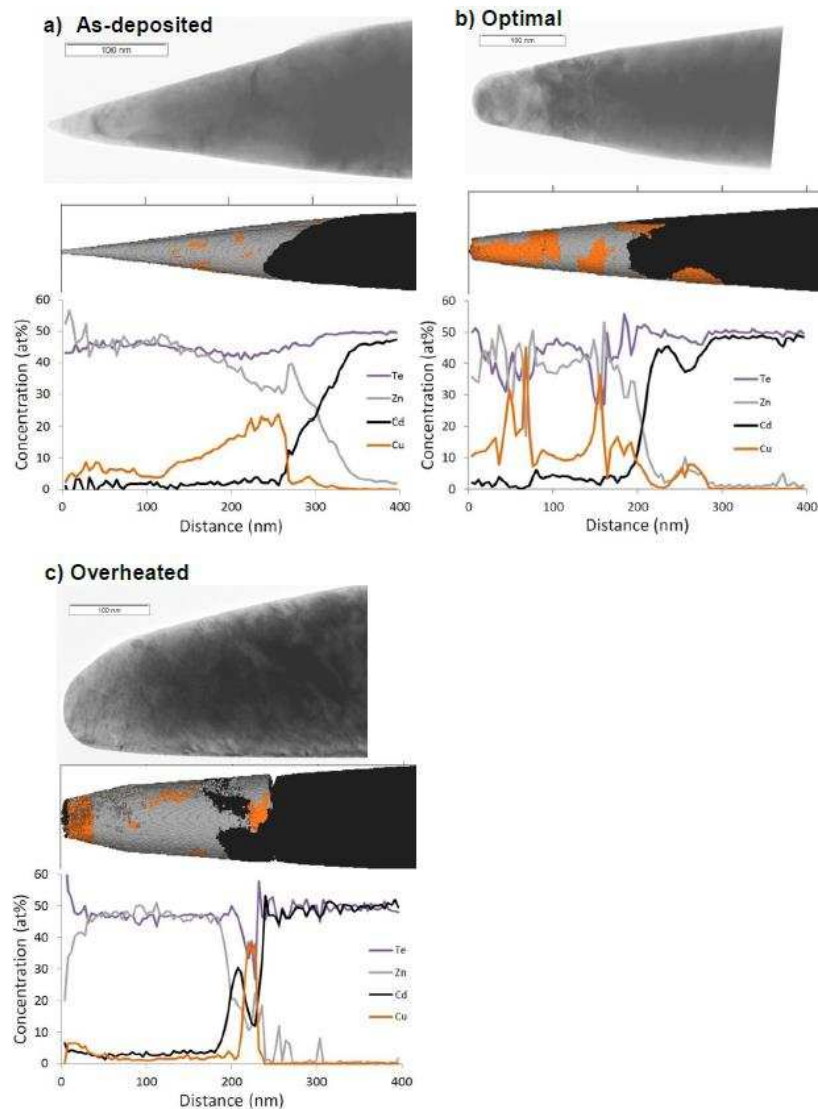


Figure 5-5: TEM images of samples before APT processing, 2D images of the resulting elemental reconstruction, and 1D volume averaged concentration profiles of the back contact region obtained from a) the as-deposited; b) optimally-processed and c) the overheated samples. Note that $z = 0$ in the APT reconstructions corresponds to the position of the ZnTe/Au interface. Click on the following URL to access videos displaying the full 3D elemental reconstruction of the as-deposited, optimal, and overheated samples. In the videos and images above the threshold values used for the iso concentration surfaces – are 25 at.% for Cd (black), 25 at.% for Zn (grey), and 10 at.% for Cu (orange).

Figure 5-5a displays the results for the as-deposited sample. During co-evaporation the intent was to deposit copper uniformly throughout the buffer layer sample, though in this sample higher levels are observed near the CdTe interface. The non-uniform profile is attributed to the challenges of the co-evaporation process. The evaporation rates of both constituents are controlled by independent power supplies and monitored by two QCMs. However the nominal evaporation rate of Cu is 0.5 \AA/s , which is near the lower limit of the QCM's sensitivity, making control challenging. It is straightforward to control the total amount of copper deposited, but the variations observed in this APT sample are attributed to our ability to precisely control the local Cu evaporation rate. However, we note that while the RTP process is sensitive to the total fraction of copper in the buffer layer, but not significantly influenced by its initial distribution. Previously we demonstrated that device results achieved with ZnTe|Cu bilayers were nominally identical to co-evaporated buffers [20]. The volume-averaged copper content in the as-deposited buffer was 9.8 at.% (3.4 wt.%), which is quite comparable to the nominal composition of ZnTe:Cu targets used in sputter deposition [124].

Figure 5-5b shows the APT reconstruction of a sample processed with an optimal RTP treatment. In this case APT reveals considerable segregation of copper toward both the Au and CdTe interfaces. Comparison of Figure 5-4 and Figure 5-5 highlight the power of APT for nanoscale analysis of these interfacial regions that are so critical to controlling the performance of thin film photovoltaic devices. The SIMS profile for these samples indicate that Cu is uniformly distributed throughout the ZnTe, where in reality it is highly localized with some individual regions exceeding 50 at.%. These images suggest that copper redistribution within the ZnTe region is controlled primarily by thermodynamic parameters such as solubility and partition functions as opposed to Fickian diffusion. The high localized levels of Cu suggest the possibility of Cu_xTe formation, as the regions with elevated Cu content are well-correlated to displacement of Zn. This finding is perhaps not surprising given that the formation energy of Cu_2Te is close to zero [54]. So while Cu_xTe and ZnTe:Cu have been previously considered to be distinct buffer layers, these results suggest that they may share some notable similarities, at least when processed using RTP.

Finally Figure 5-5c shows the APT reconstruction of a sample that has been overheated

during RTP treatment. It is remarkable that the application of just 30 s of additional RTP treatment beyond the optimized condition results in significant depletion of Cu from the ZnTe buffer layer. Characteristics of the Cu_xTe phase remain at the CdTe interface, but it is largely diminished at the Au interface. Significant Cd diffusion from the absorber layer is also observed. This is also seen in the optimal sample, but in the overheated sample the alloying process appears complete with a uniform density of ~ 4 at.% Cd throughout the ZnTe layer. In addition, significant Te and Cd accumulations at the Au interface are observed, which may be another contributing factor to the substantial decline in performance of the overheated sample.

5.4 Discussion

It is somewhat surprising that the very heterogeneous structure produced under optimal RTP processing was correlated to such dramatic improvements in device performance. Figure 5-6 displays proposed band diagrams of the back contact region illustrating the changes that occur in the optimized RTP process. The electronic structure of the back contact region in the as-deposited state was based on the work of Späth *et al.* [158], who constructed their band diagram of this heterojunction using ultraviolet photoelectron spectroscopy (UPS) measurements of the valence band maximum position relative to the Fermi level obtained from CdTe and after subsequent sputter deposition of ZnTe. We assume that the Fermi level in the as-deposited ZnTe:Cu is similar to their value, because although Cu is present, it has not been thermally activated. In this structure there is a negligible valence band offset (~ 0.1 eV) at the ZnTe|CdTe interface, but a significant Schottky barrier present at the gold interface. In addition, since these layers are deposited at low temperature it is expected that there are significant densities of defects and trap states at the interface. Indeed it was suggested in the previous UPS work that defects must be present at this interface to ensure charge neutrality and explain why band bending only occurs in the CdTe layer [158]. After optimal RTP treatment we postulate two major changes. First, the ZnTe:Cu layer becomes more p-type due to activation of Cu dopants, which shifts the valence band offset into a position that eliminates any barriers to hole transport at the ZnTe|CdTe interface [158]. Second, it is postulated that the Cu migration to the interfaces observed by APT is critical for passivation

of defect states, which allows band bending to occur on both sides of the ZnTe|CdTe interface and creates an efficient tunnel junction into the Au metallization layer. Finally this structure presents a formidable barrier to electron transport, which should minimize recombination in the back contact region.

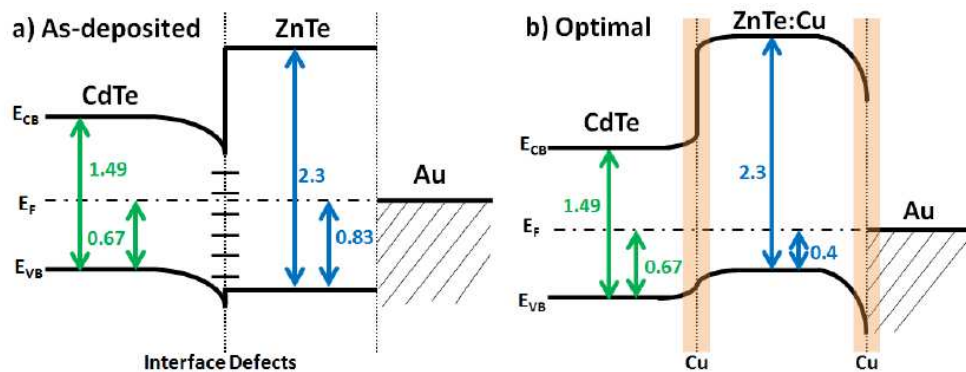


Figure 5-6: Postulated band diagrams of the back contact region for these devices in the a) as-deposited state and b) after application of an optimized RTP treatment.

Rapid thermal processing is critical to enable the benefits shown in this work. The staggering changes that occur in the ZnTe buffer region after 30 s RTP treatments suggest that its structure is determined by thermodynamic quantities such as solubility and stability of the relevant phases. It is highly unlikely that the unique non-equilibrium structures observed in this work that are correlated with high performance could be achieved through conventional thermal processing. Decoupling buffer deposition and activation, combined with the precise control imparted by RTP, are identified as the key enablers. Finally, the low thermal budgets employed suggest that this process should be readily adapted to other systems. This attribute was recently demonstrated when the back contact procedure described here was applied to devices fabricated by the National Renewable Energy Laboratory based on 100 μm flexible glass superstrates [130]. Application of the RTP back contact contributed to elevating the certified efficiency of devices fabricated on this platform from 14% to >16% [159].

5.5 Conclusions

It is demonstrated that RTP is a highly effective approach to activate ZnTe:Cu-based back contacts, providing significant improvements in V_{OC} , FF, and efficiency. The dramatic

improvements in V_{OC} and τ are attributed to the elimination of barriers and mitigation of surface recombination in the back contact region. Analysis of SIMS profiles suggest that the Au metallization layer serves as a sink for much of the Cu supplied in the buffer, and that the degree of copper migration into the CdTe is substantially reduced relative to conventional thermal activation. As such, the impact of optimal RTP on the bulk CdTe device structure is minimal, which is confirmed by the observation of negligible changes in parameters such as N_A , QE, or J_{sc} . APT reveals the nanoscale heterogeneity of this back contact and the dramatic elemental redistribution that occurs during brief RTP treatments. Under optimal conditions Cu displays heterogeneous local enrichment including segregation to both the CdTe and Au interfaces, perhaps in the form of Cu_xTe , which is suggested as one of the underlying reasons for the dramatic improvements in back contact performance. This process has been demonstrated to be beneficial on multiple device structures, as the low thermal budget of RTP facilitates its adoption without impacting the optimization of upstream processing.

CHAPTER 6

THE ROLES OF ZNTE BUFFER LAYERS ON CDTE SOLAR CELL PERFORMANCE

This chapter is an adaption of a paper submitted to the Solar Energy Materials and Solar cells.

6.1 Introduction

With an ideal band gap (~ 1.45 eV) and large absorption coefficient ($>10^4$ cm⁻¹) CdTe has emerged as the leading thin film photovoltaic (PV) technology with record efficiency currently at 21.5% [75]. Most recent advances have been due to improvements in short circuit current (J_{SC}) and fill factor (FF), whereas the open circuit voltage (V_{OC}) values have remained largely unchanged [81]. A requirement for high V_{OC} is good ohmic contact with CdTe, which is challenging due to its low doping and electron affinity. Consequences of such barriers involve loss of open circuit voltage (V_{OC}) and fill factor (FF), which are often manifested by the presence of roll over behavior in J-V curves [139]. A common strategy to address this problem is through the insertion of a thin interfacial layer between the CdTe and metal contact [132]. Copper-doped zinc telluride (ZnTe:Cu) has been widely adopted for this role [42]. Copper degenerately dopes this layer, which narrows the barrier width and permits electron tunneling, creating a quasi-ohmic contact [45]. Copper has been associated with several defect state located throughout the band gap [160], some of which have been attributed to reduced carrier lifetime and/or problems with stability [52]. First Solar Inc. recently reported that they have integrated ZnTe buffer layers into their commercial modules [161]. Incorporation of ZnTe has been credited with improving the efficiency of champion device efficiency, as well as enhancing both the stability and temperature sensitivity of their modules. In this paper we provide nanoscale characterization of the back contact region that provides new insights into the mechanism(s) that may contribute to these improvements.

We have recently introduced a back contact procedure in which ZnTe:Cu is

co-evaporated at low temperature following by activation using rapid thermal processing (RTP) [20, 65]. RTP offers several advantages for this activation step including improved control, low thermal budget, and high throughput. This technique has been used in the fabrication of CdTe solar cells on flexible glass with certified efficiencies of 16.4% [162]. Previously the macroscopic distribution of Cu was we characterized secondary ion mass spectrometry (SIMS) both before and after RTP processing [65], and quantitative analysis of this data raised a number of important questions. First, the optimal dose of Cu in the as-deposited ZnTe:Cu is $Q_0 \sim 10^{17} \text{ cm}^{-2}$, which is two orders of magnitude greater than the optimal amount required for doping CdTe as reported by Kranz *et al.* [125], and about an order of magnitude greater than the few nms of copper that is typically used to form Cu_xTe -based contacts [150, 163]. In fitting the Cu diffusion profiles in CdTe as a function of RTP temperature it was found that it was required to reduce the modeled dose to 20% of the experimental value in order to obtain good agreement with the SIMS data [65], which implies that the majority of the Cu supplied during co-evaporation does not enter the absorber layer. Lastly, the effective diffusivity of Cu extracted from the SIMS profiles was just $\sim 10^{-12} \text{ cm}^2/\text{s}$, which is three to five orders of magnitude less than values expected at the temperatures involved [144, 154].

One limitation of SIMS is that it provides averaged one-dimensional profiles, and does not account for any lateral variations that may be present. In polycrystalline CdTe it is observed that impurities such as Cu are preferentially transported and accumulated along grain boundaries [157]. Understanding the nanoscale distribution of these components is critical to advancing the fundamental understanding of this material system. To this end we employ atom probe tomography (APT) and high resolution transmission electron microscopy (HR-TEM) to quantify the changes in structure and composition in the back contact region of ZnTe:Cu contacted solar cells during RTP activation.

6.2 Materials and Methods

6.2.1 Device Fabrication

Figure 6-1 displays a schematic cross-section of the superstrate architecture employed by the devices examined in this work. The front contacts employ a tin oxide bilayer deposited

on Corning 7059 glass by thermal chemical vapor deposition and an oxygenated CdS:O window layer deposited by reactive sputtering as described in the literature [27]. The only difference in the two sets of devices examined was the nature of the CdTe absorber layer. One set of devices employed CdTe deposited by close space sublimation (CSS) at 600 °C at the National Renewable Energy Laboratory (NREL) [27]. The second set of devices were fabricated at Colorado School of Mines (CSM) by vapor transport deposition (VTD) at 450 °C [34]. In both cases the back contact preparation involved a 10 s dip in a bromine methanol solution to remove oxides and surface contaminants introduced during vapor CdCl₂ treatment. Afterwards ~165 nm of ZnTe:Cu (~4 wt.% Cu) was evaporated by co-evaporation, followed by evaporation of ~100 nm of Au which served as the metallization layer. Activation of the back contact was accomplished by annealing the devices in an RTP system for 30 s at the desired setpoint, which was measured by a thermocouple in contact with the AlN susceptor as described previously [20].

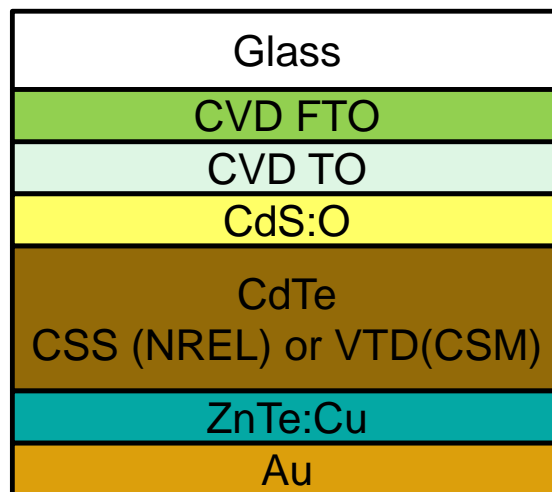


Figure 6-1: Schematic cross-section of the device structures considered in this work. NREL absorbers were deposited by CSS at 600 °C while CSM absorbers were deposited by VTD at 450 °C.

6.2.2 Device Performance

The solar cell performance was measured under simulated AM1.5 radiation using a commercial tool that is calibrated using a certified silicon standard (PV Measurements).

Figure 6-2 displays the evolution of the J-V behavior of these devices as a function of RTP annealing temperature. The CSS devices have very low efficiency (<2%) after application of the back contact. RTP activation leads to monotonic increases in all three contributors to efficiency (V_{OC} , FF, and J_{SC}) up until the optimal temperature which was 300 °C. In contrast, the devices fabricated at CSM display strong current collection prior to RTP activation. Application of an optimal RTP treatment increases V_{OC} and FF without altering J_{SC} . The applications of excessive heat treatment reduce efficiency through a decline in all secondary parameters, and are correlated with an increased density of Cu-related defects [160].

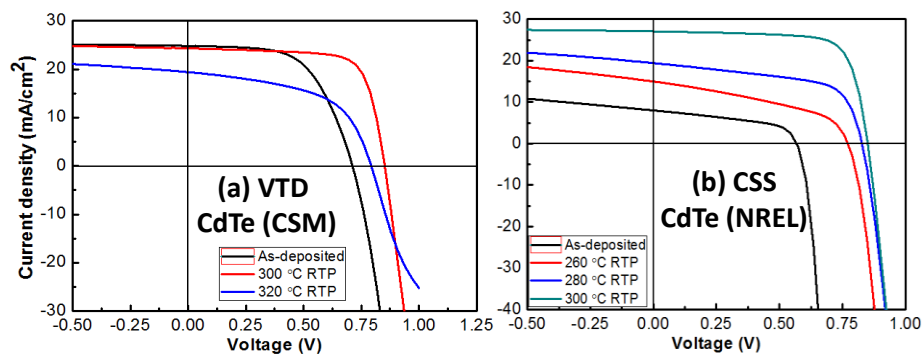


Figure 6-2: Evolution of J-V performance as a function of RTP treatment temperature for devices employing a) CSM VTD CdTe and b) NREL CSS CdTe.

The reasons for the strikingly different J-V evolution profiles are not fully understood. Impurities are one possibility, though the CdTe source materials used in both VTD and CSS processes had nominally identical purity (>99.999%). Another factor might be the different temperatures used, but the most plausible explanation is the presence of oxygen (6.25%) used during CSS deposition. It has been shown that oxygen can oxidize grain boundaries and inhibit interlayer diffusion [164, 165]. It is postulated that the oxidized grain boundaries may limit the effective conductivity of CSS-deposited CdTe prior to RTP activation. Despite the differences prior to RTP activation, the J-V characteristics of optimally processed devices exhibit very similar performance, with typical power conversion efficiencies of 15-16% on both platforms. To understand the changes that occur during activation nanoscale characterization of the back contact region is compared before and after RTP activation.

6.2.3 Nanoscale Characterization

Two techniques were employed to provide nanoscale characterization of structure and composition in the back contact region. High resolution transmission electron microscopy (HR-TEM) was the tool used to investigate the detailed microstructure of the NREL CSS cells using the facilities at Loughborough. TEM samples were prepared by focused ion beam (FIB) milling using a dual beam FEI Nova 600 nanolab. A standard in situ lift out method described previously [166] was employed for sample preparation. High resolution TEM imaging was carried out in a FEI Technai F20 equipped with an Oxford Instruments X-Max 80 silicon drift detector (SDD) energy dispersive X-ray detector (EDX). EDX was used to produce chemical distribution maps of the cells as well as line scans and point analysis for quantitative elemental analysis. Devices fabricated at CSM by VTD were examined using atom probe tomography (APT). APT analyses were performed on a Cameca LEAP 4000X Si local electrode atom probe instrument using parameters optimized for quantitative evaluation of these materials [110]. Additionally, transmission electron microscopy (TEM) images before and after APT analyses were acquired with a Philips CM200 TEM using a holder specifically designed for imaging APT specimens [149].

6.3 Results

6.3.1 High Resolution Transmission Electron Microscopy

6.3.1.1 Microstructure and Morphology

First we examine the structural changes that occur upon RTP activation using NREL CSS absorbers. Figure 6-3 displays HR-TEM images of the back contact region before (left) and after (right) optimal RTP activation, respectively. The before image is a high-angle annular dark-field (HAADF) image of the back contact region in which the gold contact appears bright, and the Pt was introduced during sample preparation. The image contains two large CdTe grains, with a well-defined ZnTe layer between the absorber and the gold. The individual layers are well defined with little evidence of intermixing, as expected for the low temperature co-evaporation process. As previously reported [167] the as-deposited ZnTe:Cu film is nanocrystalline, and consistent with literature [168]. Cu_xTe phases are observed to

form during low temperature co-evaporation. Specifically, XRD revealed peaks at 2θ 24.7° and 26.7° that have been assigned to (009) reflection of Cu_2Te and the (101) plane of $\text{Cu}_{1.4}\text{Te}$, respectively [60].

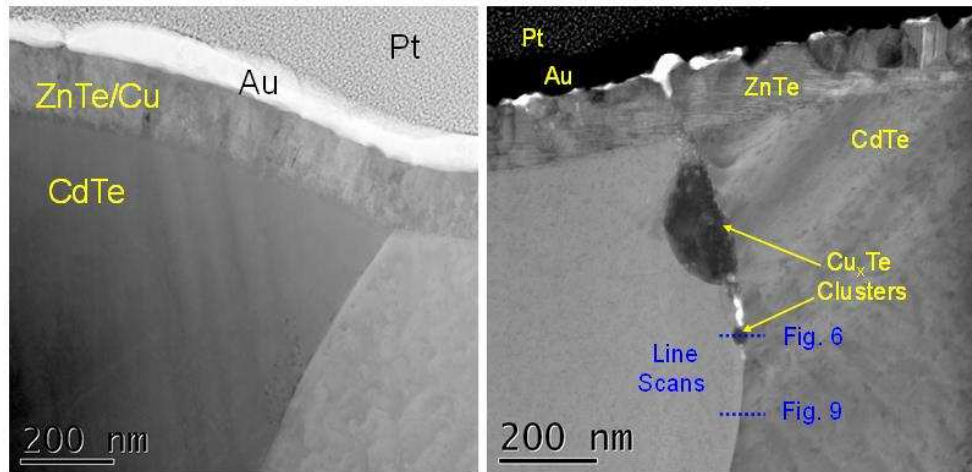


Figure 6-3: HAADF image (left) and a bright field TEM image (right) of the back contact region before (left) and after (right) RTP treatment. The dashed lines indicate the positions where 1-D compositional profiles were taken as presented and discussed below in Figure 6-6 and Figure 6-9, respectively.

The contrast is reversed in the bright field TEM image of the back contact after RTP activation, with heavy elements such as Au and Pt appearing dark. The ZnTe thickness remains nominally unchanged after RTP activation, but there are substantial changes to its morphology. Substantial grain growth occurs and twins not unlike those seen in CdTe are observed, particularly in the region adjacent to the gold metallization layer. In contrast, the region adjacent to the CdTe layer appears to be much more amorphous, and it is suggested that the cause may be Zn-Cd interdiffusion. The CdTe grain boundary (GB) before activation appears very clean, but after activation defects appear in the GB near the ZnTe interface. Most notable in Figure 6-3 (right) is the presence of a two dark clusters, one large and one small. As discussed below these clusters are Cu_xTe , and such clusters are observed at GBs and defects in the CdTe near the interface with ZnTe. Note that after moving a few hundred nanometers from the ZnTe interface the GBs appear to be very clean and defect free. Figure 6-4 displays a high resolution image of the CdTe|ZnTe interface after RTP activation as well as selected area diffraction (SAD) images obtained from the two regions. The interface is not

atomically abrupt, and its approximate position is indicated by the dashed line in the TEM image. Despite disordered material along the interface, which ranged in thickness from 5 to 15nm, lattice fringes may be clearly observed within the ZnTe layer, and the nanocrystalline nature of the film is confirmed by the SAD image. Note that the diameter of the SAD aperture was comparable to the ZnTe thickness, and though it was focused on center of the ZnTe layer contributions from either Au or CdTe cannot be ruled out, making quantitative analysis challenging. In clear contrast, the large CdTe grains provide a clean SAD image characteristic of its zinc blende structure.

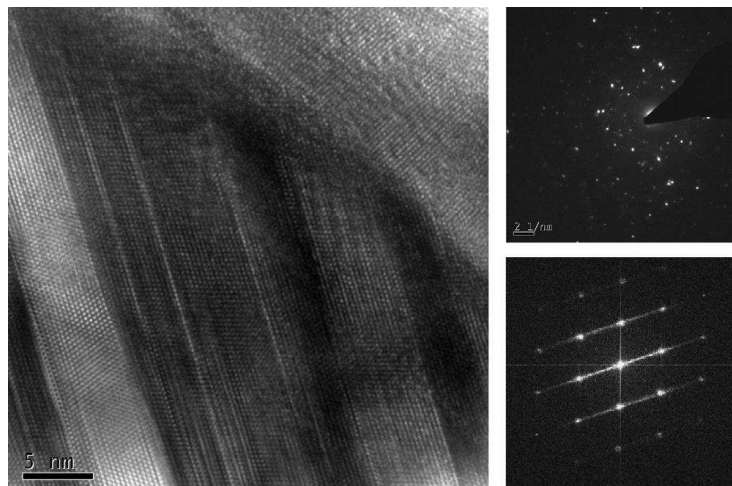


Figure 6-4: High resolution TEM of the CdTe/ZnTe interfacial region after RTP activation and selected area diffraction images taken from both layers.

6.3.1.2 Back Contact Composition

Figure 6-5 displays TEM images and elemental contour maps obtained from these regions before and after RTP activation, respectively. As expected, the co-evaporation process distributes the copper uniformly throughout the ZnTe layer. There is no evidence of intermixing with the exception of a small amount of Cu that appears to penetrate a grain boundary located at the knee in the profile maps. After RTP activation there are substantial changes in the elemental distribution, in particular Cu. The copper distribution is observed to both segregate and aggregate in dramatic fashion after RTP. The majority of the Cu segregates to the Au/ZnTe interface, with much of it present in clusters whose size is on the order of 30-50 nm. While the majority of Cu migrates to the Au layer, there are also several

Cu-containing clusters located adjacent to the ZnTe|CdTe interface. In Figure 6-5 there are two such clusters, one that appears at a GB and the other at a defect. In addition, it is observed that Zn also accumulates in these Cu-containing defect regions, and we will return to this observation below.

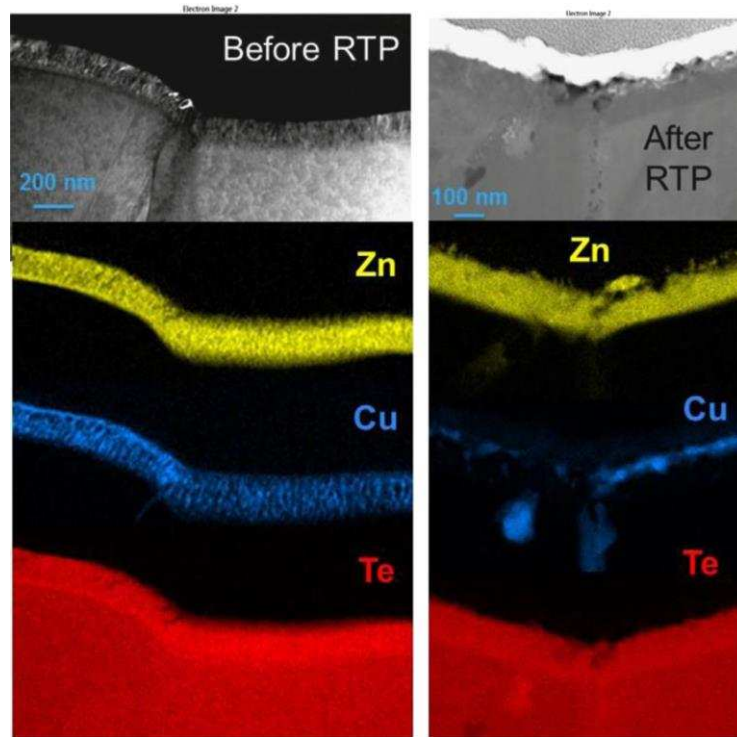


Figure 6-5: TEM images and elemental mapping of the back contact region before and after optimal RTP treatment.

The elemental contour maps provide a qualitative overview of the changes induced by RTP. To provide a more quantitative perspective EDAX line scans were used to quantify the elemental composition. Figure 6-6 displays an HAADF image as well as three plots showing the elemental profiles through the selected line scans. This TEM image was selected because it conveniently contains all the major features that have been observed along the interface. The leftmost scan b) profiles a clean interface with the absence of any major structural features. This is characteristic of the majority of the back contact region. The middle scan c) shows the profile through a defect in the ZnTe layer, which were rarely observed. The final scan d) profiles through the ZnTe layer and into a copper-rich inclusion within the CdTe.

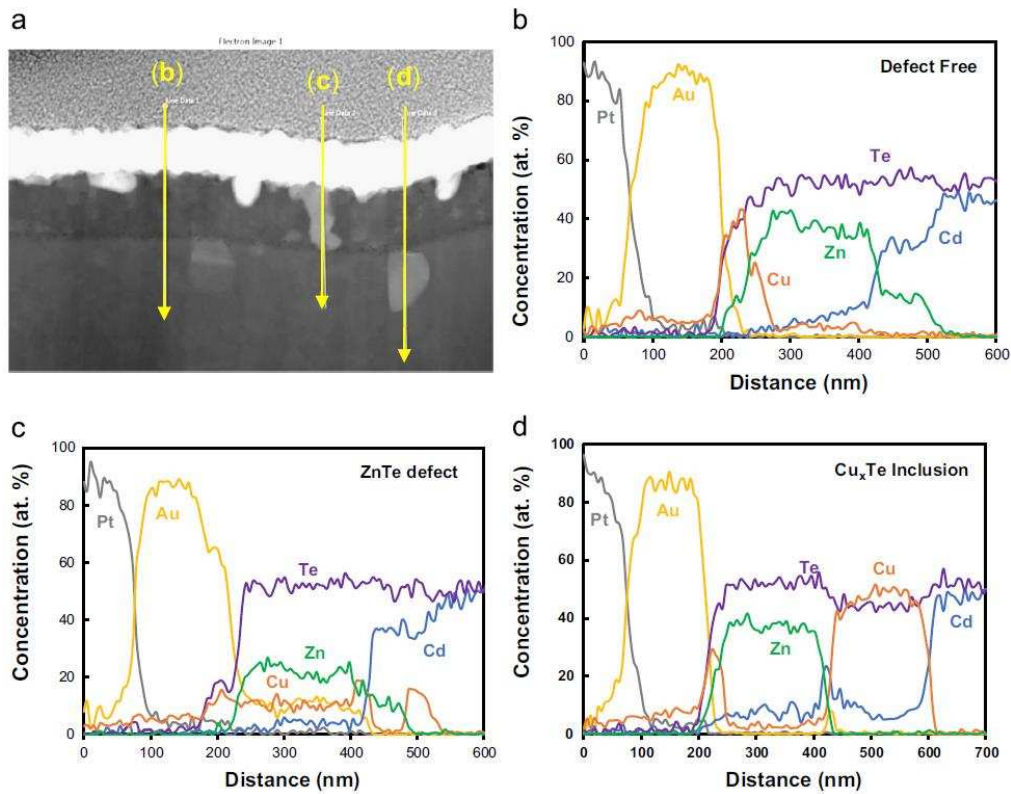


Figure 6-6: a) TEM image of the back contact region after RTP and 1D elemental profiles through the highlighted regions that include b) a defect-free region, c) a region with a defect in the ZnTe layer, and d) a region that passes through a Cu_xTe inclusion in the CdTe layer.

The first elemental profile begins in the Pt layer used during FIB sample preparation and crosses the back contact in a line that is free of structural defects (Figure 6-6b). The gold metallization layer remains largely intact, with little evidence of interdiffusion or rearrangement. It is observed that there is significant accumulation of Cu at the Au|ZnTe interface. This observation is consistent with the previous analysis of quantified SIMS results [65], which suggested that up to 80% of the Cu deposited in the ZnTe:Cu layer segregates into the gold during RTP processing. This is perhaps unsurprising as these two metals are completely miscible. Now turning to the ZnTe layer we see two distinct regions that correspond to the morphological distinctions discussed above. It is observed that the composition of the first ~100 nm of this layer adjacent to the gold is approximately stoichiometric ZnTe, corresponding to the region with well-defined crystallites (Figure 6-3b). In contrast the last 50 nm, the region that appears amorphous in the TEM, shows evidence of extensive Zn-Cd interdiffusion. In fact the Cd:Zn ratio is approximately 2 in this region. This interdiffusion process appears to occur predominantly within the ZnTe layer, as the

composition quickly reverts to stoichiometric CdTe once crossing the ZnTe|CdTe interface. The second line scan shows the profile through a defect present in the ZnTe layer (Figure 6-6c). In this case it is observed that Cu does not accumulate at the Au|ZnTe interface but remains rather uniformly distributed and is accompanied by the infiltration of significant amounts of gold, both present at levels on the order of ~10 at.% level throughout. Despite the presence of this structural defect there is again evidence of Zn-Cd interdiffusion at the interface with CdTe. Finally, the third line scan (Figure 6-6d) profiles through ZnTe into a Cu-rich cluster within the CdTe absorber. As in the first scan it is observed that a significant amount of Cu accumulates at the Au|ZnTe interface, but Cu is largely displaced from the ZnTe layer itself. Again strong evidence of Cd diffusion into the ZnTe layer is observed. As eluded to earlier the composition of the Cu-rich cluster appears to be Cu_xTe , as the Cd signal is strongly attenuated and no other elements are detected. Upon exiting cluster the composition abruptly returns to that of stoichiometric CdTe.

It is surmised that these Cu_xTe clusters located at defects and grain boundaries in the CdTe layer may have a major impact on both performance and stability, so their composition was investigated in more detail. Figure 6-7 displays the elemental line scan obtained across CdTe grain boundaries at the two positions highlighted in Figure 6-3. The first profile (Figure 6-7a) crosses the small Cu_xTe cluster located within the CdTe grain boundary. No impurities are detected within the bulk CdTe. The cluster itself is composed exclusively of Cu and Te, as the Cd signal is reduced to background levels. The approximate composition of the clusters is estimated to be $\text{Cu}_{1.2}\text{Te}$, which is very close to the $\text{Cu}_{1.4}\text{Te}$ phase that is commonly observed in CdTe back contacts [60, 150, 169]. Perhaps most interesting aspect of this plot is the Zn profile. Recall that the elemental contour plots (Figure 6-5) showed that the Cu-rich aggregates within the CdTe were accompanied by enhanced levels of Zn. The 1D Zn profile shows that Zn is concentrated at the interface between the cluster and CdTe, giving rise to the idea that a thin layer of Zn may be encasing the Cu_xTe clusters.

Figure 6-7b displays the elemental profile obtained across the clean grain boundary shown in Figure 6-3 that is approximately 150 nm away from the $\text{Cu}_{1.4}\text{Te}$ cluster. The width of the grain boundary at this point is 2 nm, and the only significant impurity observed is Cl, which is well-known to decorate grain boundaries in CdTe [157, 166]. The Cl reaches a peak

concentration of 7 at.%, and is accompanied by a reduction in both Cd and Te. There may also be a slight enrichment of Zn at this position. The Cu signal is at the limits of detection, with no significant difference in the nominal intensity between the grain and grain boundary. The grain boundary composition was examined at several positions in the sample, and no Cu or Zn was detected beyond 500nm from the ZnTe interface, indicating that the structural and chemical changes induced by RTP were restricted to the vicinity of the back contact.

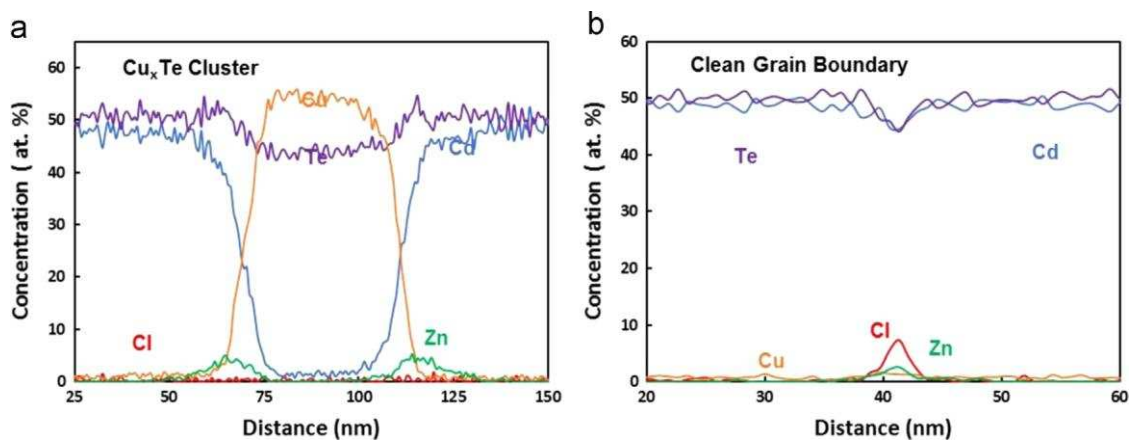


Figure 6-7: Elemental composition profile across CdTe grain boundaries at the positions indicated in Figure 6-3. Profile a) crosses the small Cu_xTe inclusion and b) crosses the clean grain boundary located 150nm away.

6.3.2 Atom Probe Tomography

TEM analysis of the CSS absorbers suggests the formation of core-shell nanostructures comprised of Zn and Cu_xTe at GBs and defects in the CdTe near the back contact. To fully assess this possibility atom probe tomography was used to provide three-dimensional characterization of the back contact region using devices made at CSM by VTD. Previously we had used APT to examine the composition of the back contact region after RTP activation [65], and as reported here it was found that copper segregates and aggregates at both the interface with gold and CdTe. With the insight provided by the preceding TEM analysis were turned to these images to look for evidence of core-shell nanostructure formation.

Figure 6-8 shows 3D isocontours of Cu, and Cu and Zn, with threshold levels set at 25 and 6 at.%, respectively. This Cu-rich cluster is approximately 30 nm in diameter, and as in the TEM images it was located in CdTe within 100 nm of the nominal interface with ZnTe.

The second image clearly shows that this Cu_xTe cluster is encased in Zn. To further confirm the core-shell nature of these clusters Figure 6-9 shows 2D contour plots of the relative Cu and Zn density extracted from a slice through the center of one of these clusters. The Zn composition reaches a peak of 12 at.% within the shell and the FWHM thickness of this layer is 11 nm based on 1D profiles orthogonal to the cluster surface. Both the width and density of Zn in the shell layer are in good agreement with the values provided by EDX line profiles shown in Figure 6-7a. Quantitative analysis of the composition at the center of the particle confirms that its formula is $\text{Cu}_{1.4}\text{Te}$. In the mass spectrum there are peak overlaps between some isotopes of Te^{2+} and Cu^+ and Te^{2+} and Zn^+ . For quantification of the particle composition, the mass spectrum from only within the particle was extracted and analyzed. The APT analysis conditions were such that very little Te^{2+} was observed; nevertheless, peak decomposition was performed using the non-overlapping isotopes for precise quantification.

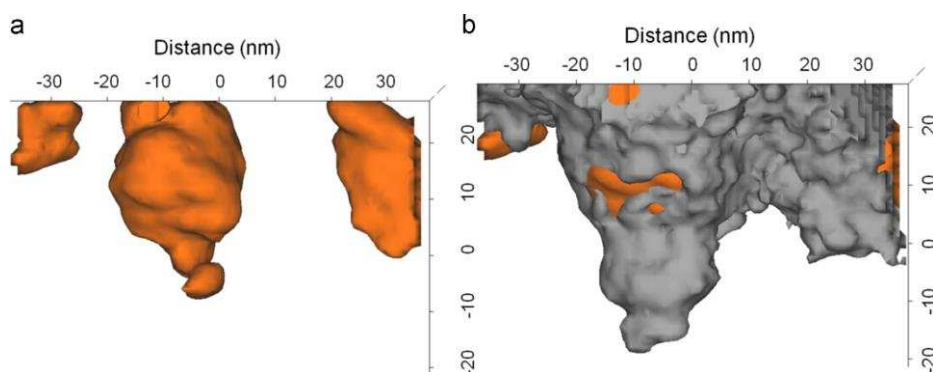


Figure 6-8: 3D isocontours of a $\text{Cu}_{1.4}\text{Te}$ cluster provided by APT showing the a) Cu and b) both Cu and Zn with the concentration threshold set at 25 and 6 at.% respectively.

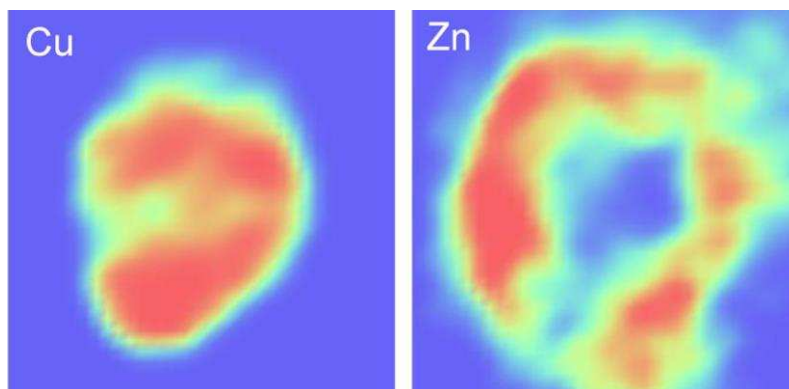


Figure 6-9: 2-D contour plots obtained from the center of a $\text{Cu}_{1.4}\text{Te}$ cluster confirming the core-shell structure with a Zn-enriched layer completely encasing a $\text{Cu}_{1.4}\text{Te}$ cluster.

6.4 Discussion

It is shown here that copper, introduced uniformly as ZnTe:Cu by co-evaporation, dramatically aggregates and segregates upon RTP activation. A majority of copper is found adjacent to the Au metallization layer, drawn here by the miscibility of the two metals. This Cu is effectively removed from CdTe, explaining the limited amount observed in SIMS analysis. The bulk of the remaining Cu is found in the form of $\text{Cu}_{1.4}\text{Te}$ clusters encased in Zn at grain boundaries and defects in CdTe near the interface with ZnTe. Such an observation is also consistent with extremely low effective Cu diffusivity observed [65], as the transport of such nanoclusters would be significantly diminished relative to elemental Cu. The sequestration of Cu at the metallization layer and in these clusters limits the amount of free Cu available to dope CdTe, explaining why the amounts of Cu used in ZnTe:Cu buffers [42, 65, 124] exceeds that employed in conventional Cu_xTe contacts [150, 163] or the amount required for optimal doping of CdTe [125].

The ZnTe layer itself undergoes significant rearrangement, forming a bilayer structure. Significant recrystallization and grain growth is observed in the layer adjacent to the Au metallization with evidence of twin formation. The layer adjacent to CdTe appears amorphous and is characterized by significant Cd-Zn interdiffusion. It is suggested that interdiffusion process liberates Zn and T, enabling the reaction with free Cu to form the Zn-encased $\text{Cu}_{1.4}\text{Te}$ clusters. The great similarity of the nanostructured morphology observed in VTD and CSS devices suggest that this structure is a function of the RTP back contacting process and not the absorber itself.

The phenomenological observations discussed above are also consistent with device performance. The significant characteristics of ZnTe:Cu devices activated by RTP as shown in Figure 6-2 and previously [65, 162] is the improvements in both V_{OC} and FF. In particular, these devices exhibit low series resistance and the absence of rollover. It is assumed that CdTe-ZnTe interdiffusion passivates interface states providing a good ohmic contact. It is well established that passivated GBs provide pathways for efficient current collection [145]. The presence of $\text{Cu}_{1.4}\text{Te}$ clusters at the GB terminus is suggested to promote charge extraction. Rollover, often observed in devices contacted with Cu_xTe [27], has been attributed to the formation of Cu-related oxidation [150], and its absence in the devices described here

suggests that ZnTe may mitigate its formation. The diffusion of excess Cu into the CdS often manifests itself in a “cross over” feature a when comparing dark and light J-V curves [150]. Likewise excess Cu in the absorbers itself has been correlated with voltage-dependent collection that limits FF. Both of these issues are concerns for long term stability. The absence of significant cross-over and high FF in the ZnTe:Cu contacted devices suggests that excess Cu diffusion is mitigated, likely through its sequestration in clusters as described above.

It is of value to compare the results observed here for ZnTe:Cu with the more commonly used Cu_xTe buffer layer [33, 170]. This layer is commonly prepared by etching the CdTe absorber to remove oxides and create a Te-rich surface, followed by evaporation of copper and thermal annealing. The Cu-Te phase diagram is incredibly complex with numerous phases and polymorphs, particularly in the Cu_{2-x}Te region [171]. Nevertheless, under conditions employed for forming CdTe back contact the three primary phases observed are CuTe, $\text{Cu}_{1.4}\text{Te}$, and Cu_2Te , which may be controlled through the amount of Cu supplied and the temperature used for activation [60]. Early reports [170] suggested that Cu_2Te was optimal for cell performance, being the most highly conductive phase it provides low series resistance. However, Cu_2Te has a high propensity to decompose and release Cu [168], raising stability concerns. Wu and co-workers reported best performance with a mixture of CuTe and $\text{Cu}_{1.4}\text{Te}$ [150], recommending that $x \leq 1.4$ to minimize Cu diffusion. More recently it was reported that $\text{Cu}_{1.4}\text{Te}$ contacts exhibited improved stability under thermal cycling than devices employed mixed $\text{Cu}_{1.4}\text{Te}/\text{CuTe}$ contacts [169]. Thus there is an emerging consensus that the $\text{Cu}_{1.4}\text{Te}$ phase provides an ideal balance of conductivity and stability. Like Cu_xTe there is an optimum amount of Cu that produces optimal performance in devices contacted with ZnTe:Cu [20], and in the optimal devices analyzed here the $\text{Cu}_{1.4}\text{Te}$ phase is observed to form, consistent with the findings from Cu_xTe buffer layers.

6.5 Conclusions

Nanoscale imaging and analysis has provided new insight into the role of ZnTe buffer layers on CdTe device performance and stability. It is shown that during thermal activation significant of CdTe-ZnTe interdiffusion occurs, creating a graded interface. Copper reacted

with Zn and Te released during this process, forming Zn-encased $\text{Cu}_{1.4}\text{Te}$ nanoclusters that are found in CdTe grain boundaries and defects along the interface with CdTe. It is suggested that these processes passivate defects and produce a good ohmic contact that enable good V_{OC} and FF. The absence of rollover in these devices is attributed to the ability of this contact to minimize the formation of Cu-related oxides. The sequestration of Cu into nanoclusters is expected to limit its diffusion into the CdTe and CdS, with positive implications for long term stability.

CHAPTER 7

THE IMPACT OF DIFFERENT METALLIZATION LAYERS ON CDTE SOLAR CELLS CONTACTED WITH ZNTE:CU BUFFER LAYERS

This chapter is an adoption and extension of a previously published paper on IEEE Photovoltaic Specialist Conference 2016.

7.1 Introduction

The advantage of thin film CdTe solar cells over crystalline silicon solar cells is low cost. CdTe is a direct bandgap semiconductor with high absorption coefficient which is greater than $10^4/\text{cm}$. The bandgap of CdTe is about 1.45 eV which is ideally matched with the solar spectra. These properties make CdTe an ideal candidate for thin film solar cells: only a few microns CdTe is enough to absorb over 90% of the incident light. However an ongoing challenge with this technology is forming high quality ohmic contact with CdTe, which reflects its low carrier concentration and high work function (5.7 eV). To overcome this problem, the CdTe surface is often treated to form a Te-rich surface and then a degenerately doped buffer layer is introduced between CdTe and the metallization layer. Commonly used materials for the back contact are Cu-contained materials, such as Cu/Au [172], Cu_2Te [173] and Cu doped ZnTe [67]. Among them, ZnTe is promising because it has good valence band alignment with CdTe [44] and can be easily doped to form a quasi-ohmic contact. First Solar has credited the integration of ZnTe as a contributor to improvements in both champion device efficiency and module reliability [174]. Cu is critical to the performance of the devices. The presence of Cu is necessary for high efficiency, but excess Cu is harmful for stability.

Previously, we demonstrated high efficiency solar cells using rapid thermal processing (RTP) to activate a back contact comprised of a ZnTe:Cu buffer layer and a gold metallization layer [65]. Observed benefits included improvements in open circuit voltage (V_{OC}) and fill factor (FF), which correlated with a significant reduction in the density of a defect located 1.2 eV above the valence band [160]. This technique has been achieve high efficiencies (15

-16.4%) using a number of different architectures [162, 175]. Copper is distributed uniformly through ZnTe in as-deposited buffer layers deposited by co-evaporation [167]. After RTP activation a suite of nanoscale characterization techniques (SIMS, TEM, APT) revealed that the majority of the Cu, as much as 80%, segregates to the Au interface reflecting the perfect miscibility of these two metals [65].

Our previous studies employed devices contacted with Au, which is commonly used as the metallization layer in research labs because of its high work function (5.2 eV), stability in air and, ease of deposition. But Au is not compatible with industrial manufacturing because of its high price. So researchers have explored a number of alternatives such as Ag [66], Ni [67], Mo [68], and Ti [69]. In addition to the cost, reliability is also one of the most important concerns for CdTe solar cells. Copper is often cited as a culprit for cell instability due to its diffusion the back contact into the CdS region [53, 128, 176]. Thus it is desirable to minimize the amount of Cu introduced into the back contact. From the SIMS profile of our optimal device, we found that over 80% of Cu co-evaporated in the ZnTe:Cu segregates into the Au [65], which is not terribly surprising since Cu and Au are completely miscible. However, this creates a reservoir of Cu that may potentially be released from Au into the device over time, causing degradation. To replace the expensive Au and minimize the amount of Cu loading in the buffer layer, we explored Cr and Ti as the potential alternatives for Au. These metals are low cost, stable and have limited solubility for Cu. The Cu content of the ZnTe buffer layer was re-optimized with different metals. The current-voltage (J-V) and quantum efficiency (QE) of these devices fabricated with different levels of copper loading are compared to understand its impact on performance. Stability tests under dark and light stressing were carried out with different metallization materials to provide insight into the degradation mechanism.

7.2 Materials and Methods

Devices were fabricated with three different metallization materials: Au, Ti and Cr. The device architecture and processing were identical with the exception of the composition of the back contact. A 150 nm CdS layer was deposited by thermal evaporation on Tec 15 glass obtained from Pilkington at 100 °C. A ~3 micron CdTe absorber layer was grown by vapor

transport deposition at $T = 450\text{ }^{\circ}\text{C}$ [34]. CdCl_2 treatment was done by using a close spaced sublimation geometry in a tube furnace at $400\text{ }^{\circ}\text{C}$ for 30 min using a 50%-50% O_2/N_2 ambient. The back surface was etched in a 0.5% (v/v) $\text{Br}/\text{CH}_3\text{OH}$ solution for 10 s and rinsed with methanol prior to back contact preparation. A $\text{ZnTe}:\text{Cu}$ buffer layer was deposited by thermal co-evaporation. The thickness of ZnTe was kept at 150 nm while the thickness of Cu was varied from 0 to 25 nm. The thickness values are based on two shielded quartz crystal monitors that were used to control the evaporation rates and thicknesses of the individual sources. 150 nm of different metallization layers were applied at room temperature. Au and Cr were deposited by thermal evaporation while magnetron sputtering was employed for Ti. Devices with an area of 0.079 cm^2 were defined with a shadow mask. Individual devices were isolated by scribing along the perimeter of the metals through the semiconductors down to the transparent conductor. After device fabrication, samples were subjected to 30 s RTP treatments under flowing Ar to activate the back contact. The solar cell performance was measured under simulated AM1.5 radiation using a commercial tool that is calibrated using a certified silicon standard (PV Measurements). Quantum efficiency (QE) was measured on a custom system with a grating monochromator and lock-in amplifier detection. Results are calibrated by comparison to a NREL-measured standard silicon solar cell. Two stressing test conditions were used to perform the reliability tests of devices with different metallization materials. One was taken in a furnace kept at $85\text{ }^{\circ}\text{C}$ under dark condition, and the other was subjected to 1 sun ($1000\text{ W}/\text{m}^2$) illumination with a halogen lamp, open circuit voltage bias and $85\text{ }^{\circ}\text{C}$.

7.3 Results

7.3.1 Device Performance Analysis

Figure 7-1 compares the efficiency as a function of the amount of Cu co-evaporated with 150 nm of ZnTe buffer with different metallization materials. The optimal Cu thickness for Au was 15 nm and the highest efficiency was 14.5%, while the optimal Cu thicknesses for Cr and Ti are 5 nm and 10 nm, respectively, with similar maximum values of 14% and 14.1%. These values demonstrate that the RTP-based back contact may be successfully applied to these low cost metals.

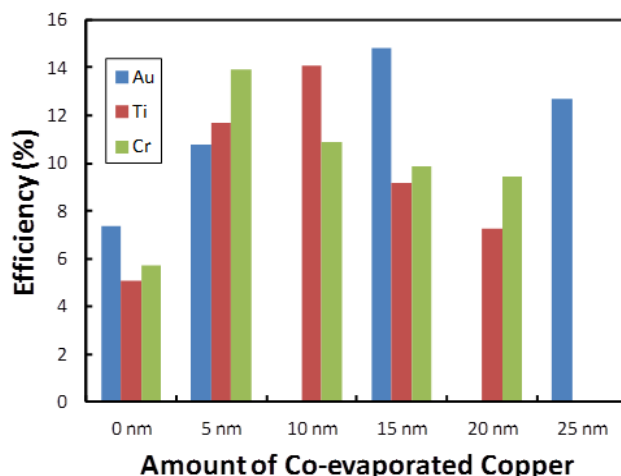


Figure 7-1: Device efficiency as a function of copper loading in the ZnTe buffer for different metallization materials.

The trend in Cu loading Au >Ti> Cr correlates with the metals affinity for Cu. Cu and Au are completely miscible [177], while Cu displays limited solubility in Ti [178] and is completely immiscible with Cr. As discussed above up to 80% of the Cu was observed to segregate into the Au layer. The 67% reduction in Cu loading for optimal performance with Cr metallization is consistent, as no such segregation would be expected to occur. Likewise the optimum loading for Ti is intermediate to these two extremes. In all three cases the efficiency slowly declines at Cu loadings below or above the optimum, and to understand the underlying mechanisms we examine the details of their J-V and QE response.

Figure 7-2 displays representative J-V curves from the devices fabricated in this study. Although the optimal devices for each metal have similar J-V curves, the evolution of the J-V behavior with changes in Cu loading is somewhat unique for each metal. In the case of Au there are monotonic improvements in all 3 secondary parameters (V_{OC} , J_{SC} , FF) as the Cu content is increased from 0 up to the optimum value of 15 nm. With excess Cu loading the J_{SC} decreases while the other parameters remain nominally unchanged. This suggests that the quality of the back contact remains largely intact, but excess Cu leads to recombination of photo-generated carriers. For Ti, without Cu, the device performance was very poor. With the addition of 5 nm of Cu all secondary parameters improved significantly. The V_{OC} is further improved as the Cu content was increased from 5 nm to the optimal value of 10 nm. With excess Cu, both J_{SC} and V_{OC} decrease but the FF remains largely unchanged. With Cr, the

initial device performance without Cu is poor, similar to Ti. With Cr best performance was obtained at the minimal Cu loading (5 nm). As the loading is increased to 10 nm the J_{SC} and FF remain essentially unchanged, but the V_{OC} is significantly attenuated. Further increases in Cu loading deteriorate all parameters and these devices begin to display rollover.

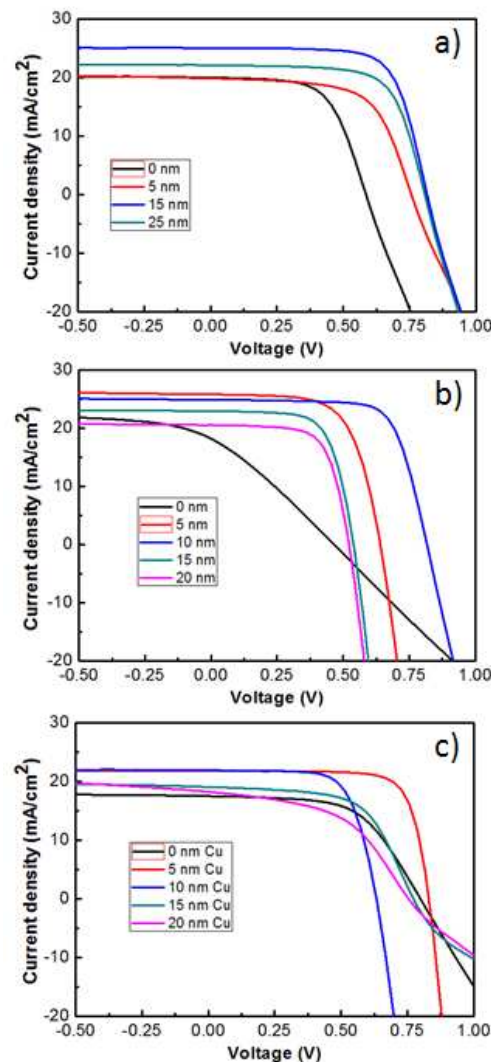


Figure 7-2: J-V curves from devices with varying Cu content using a) gold, b) titanium and c) chrome metallization layers.

Figure 7-3 shows the QE of the devices showed in Figure 7-2. The QE is basically consistent with the J_{SC} . For Au the red and blue responses not shift significantly, but the response of the CdTe (550-800 nm) increases to a maximum when Cu is 15 nm and then decreased. With regard to Ti, with 5 nm Cu it has high mid-range QE response but the response in the blue region is quite poor. Additional Cu improves the blue response but the

mid-range QE response deteriorates. Though higher current is obtained with 5 nm, the improvement in V_{OC} makes the optimal Cu loading 10 nm. With higher than 10 nm Cu the QE systematically decreases. For Cr, the best QE of the device with Cr is lower than with Au and Ti, which is consistent with the lower J_{SC} of the optimal device with Cr. The 5 nm Cu device has similar QE with the 10 nm Cu device which is agreed with their J_{SC} , and again additional Cu deteriorates the response.

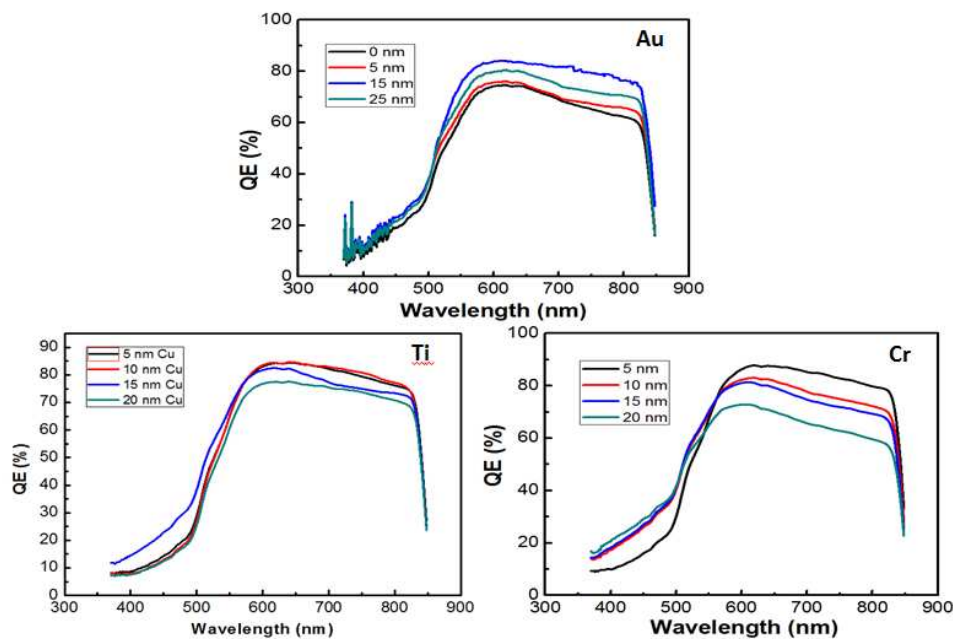


Figure 7-3: QE spectra from devices with varying Cu content using gold, titanium and chrome

The results of Figure 7-1 to Figure 7-3 indicate that the choice of metal has a major impact on device optimization and performance. The trend in Cu loading requirements ($Au > Ti > Cr$) is well correlated with the metals affinity for Cu. Cu and Au are completely miscible [177], while Cu displays limited solubility in Ti [178], while Cu is completely immiscible with Cr. As discussed above up to 80% of the Cu was observed to segregate into the Au layer. The 67% reduction in Cu loading for optimal performance with Cr metallization is consistent, as no such segregation would be expected to occur. Likewise the optimum loading for Ti is intermediate to these two extremes. Choice of metal also impacts the quality of the back contact. Titanium appears to provide the most ohmic contact, evidenced by the low series resistance and good FF observed consistently in this series of devices.

7.3.2 Reliability Tests

To further evaluate the impact of different metallization layers we subjected selected devices to accelerated lifetime testing (ALT). Devices with optimal Cu loading for each metal were exposed to two ALT conditions: light soaking and dark stressing at $T = 85\text{ }^{\circ}\text{C}$. For the first condition, devices were illuminated by a halogen lamp positioned to deliver an intensity comparable to 1 sun ($\sim 1000\text{ W/m}^2$). Samples were heated by the lamp and a fan was used to keep the temperature of the sample at $85\text{ }^{\circ}\text{C}$. According to the estimates of Hiltner [179], the life time acceleration factor is about 1000 compared to the duration in the field [176]. For the dark condition, samples were settled in a furnace and also kept at $85\text{ }^{\circ}\text{C}$. All samples were in open circuit condition.

Figure 7-4 summarizes the relative changes in device efficiency a) in the dark and b) under illumination for the three different metals. In the dark the most striking feature is the similarity between the three metals. In all cases there are three distinct regions. First, the efficiency declines $\sim 10\%$ sharply in the first few hours. Next, there is a gradual decline during the next 100 hours while afterwards the devices stabilize at 80-85% of their initial value. Under illumination there are very significant differences among the different metallization layers. Again a three step behavior is observed: (i) a sharp initial decline (0-5 hours); (ii) a gradual decline (5-125 hours), and (iii) stabilization of device performance ($t > 125$ hours). Among the metals the initial degradation period was quite similar, and also similar to the behavior of samples stressed in the dark. This suggests that this initial degradation is intrinsic and thermally controlled. Significant differences among the metals arise during the secondary stage of degradation. In the case of Ti almost no secondary degradation is observed, and devices stabilize at $\sim 85\%$ of their initial value, very similar to what was observed during dark stressing. In the case of Cr the level of secondary degradation is greater than in the dark, with final performance saturating at $\sim 65\%$ of the initial value. In the case of Au the secondary degradation is substantial, with efficiency falling to $\sim 50\%$ of its initial performance.

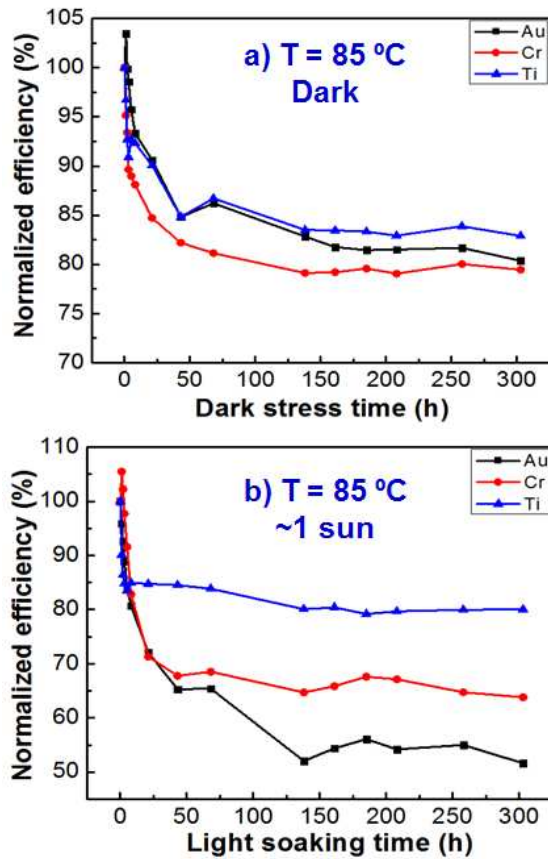


Figure 7-4: Changes in device efficiency during 300 hours of accelerated lifetime testing of a) in the dark and b) under illumination for the three metallization materials.

A principle difference between ALT testing in the dark and under illumination is that in the latter case the devices are biased at $\sim V_{OC}$. This suggests that the increased level of degradation observed under illumination reflects electromigration of ionized impurities (i.e. Cu^+) as opposed to neutral impurities. To further understand the changes we examine the evolution of their J-V behavior for these series of devices.

Figure 7-5 shows the evolution of J-V curves of the samples with three different metallization materials under dark stressing condition. As expected from Figure 7-4a samples show similar degradation behavior. In each case with increased stress the J_{SC} remains essentially unchanged and efficiency declines predominantly due to a loss of FF that accompanies the onset of rollover. Rollover develops when the back contact behaves as a rectifying Schottky contact, which is reverse biased when the CdS/CdTe solar cell is at forward bias [139]. During ALT testing of unencapsulated devices under ambient conditions rollover is commonly observed and has been attributed to oxidation of the back contact,

which results in a back contact barrier [180, 181]. For samples under dark stressing this appears to be the predominant source of device degradation, and the process is largely independent of the choice of metal.

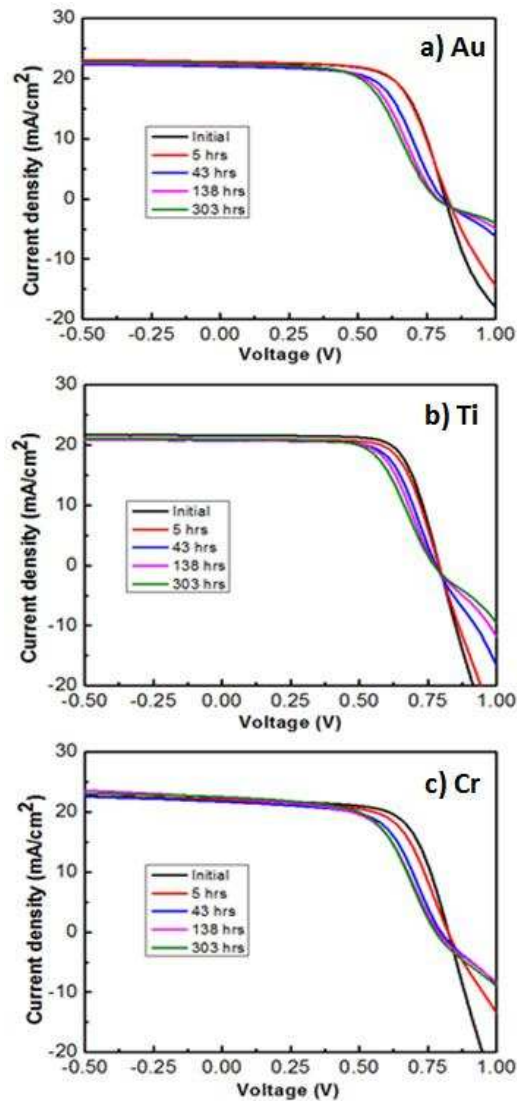


Figure 7-5: J-V curves at selected times during dark ALT testing of devices with a) gold, b) titanium and c) chrome.

Figure 7-6 compares the degradation of samples using different metallization materials under the light soaking condition. Under illumination device performance evolves very differently, and the choice of metallization material has a significant impact. During the initial phase ($t < 10$ hrs) degradation is due primarily to loss of V_{OC} with other secondary remaining largely unchanged. In the case of Ti (Figure 7-6b) after the initial V_{OC} loss device

performance stabilizes for the duration of the 300 hour test. Devices contacted with gold (Figure 7-6a) displayed the worst stability. Through the first 138 hours there are monotonic declines in all three secondary parameters. Chromium is an intermediate case. The majority of the loss is due to V_{OC} , but there are also modest declines in J_{SC} and FF.

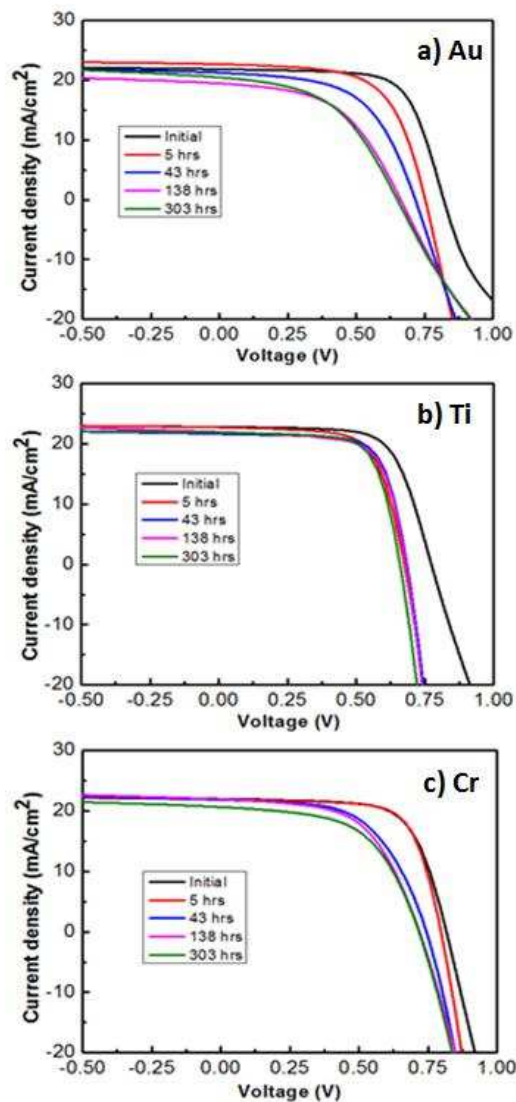


Figure 7-6: J-V curves at selected times during dark ALT testing of devices contacted with a) gold, b) titanium, and c) chrome.

The loss of V_{OC} observed under illumination has been attributed to the degradation of the main junction, which requires both high temperature and forward bias [53, 182]. Under bias the barrier to Cu^+ ion drift at the cell junction is reduced, so Cu accumulation in the CdS is enhanced which creates shunting paths and recombination centers [128, 180]. In addition,

previous studies suggest that the back contact degradation can cause a decrease in fill factor and J_{SC} [128]. It appears that the primary degradation mechanism is associated with the diffusion of Cu under illumination which degrades V_{OC} , while the samples with Au and Cr also have back contact degradation due to their losses of FF and J_{SC} . This suggests the advantage of using Ti as the metallization materials for ZnTe:Cu contacted CdTe solar cells.

Another stark difference with the illuminated samples is that they experience little rollover despite ALT being performed in an ambient atmosphere. This in part may reflect difference of our setups for dark and light stressing tests. Dark stressing was conducted in a closed furnace, with little exchange with the environment. In contrast, light soaking employed a fan to maintain the sample at 85 °C. Maintaining devices at an elevated temperature relative to the surroundings may have mitigated oxidation. Another possibility is that the presence of forward bias mitigated the oxidation process. Additional studies and physical characterization will be required to fully elucidate the differences. Regardless, titanium is clearly the most robust metal in terms of maintain excellent rectification behavior and minimizing degradation.

7.4 Summary and Conclusions

In this paper, we demonstrate that low cost metals such as Cr and Ti may be substituted for Au without compromising device performance of CdTe solar cells contacted using a ZnTe:Cu buffer layers. The optimal Cu loading decreased from 15 to 10 to 5 nm for Au, Ti and Cr, respectively. Both the order and the amounts are consistent with the solubility of Cu in these metals. Degradation during dark ALT is related to oxidation of the back contact, inducing rollover and loss of FF, and was independent of the metal choice. In contrast, ALT under illumination revealed that it shows the Cu-metal interaction is important. Among the three metals Ti is the most robust, displaying low sheet resistance and highest FF while exhibiting the best durability under all conditions examined.

CHAPTER 8

CDTE SOLAR CELLS EMPLOYING $\text{CdS}_{1-y}\text{Te}_y$ WINDOW LAYERS

This chapter is an adoption and extension of a previously published paper on IEEE Photovoltaic Specialist Conference 2016.

8.1 Introduction

CdS is widely used as the n-type heterojunction partner for CdTe because of their compatibility. Like CdTe, it may be deposited using many methods including chemical bath deposition, thermal evaporation, and sputtering. However, CdS is not an ideal window layer for CdTe solar cells. It is not photoactive, causing absorptive loss of photons with energy higher than its band gap (2.4 eV). Chu [183] showed that with 100 nm CdS, 63% of the incident radiation with energy greater than the bandgap will be absorbed. Moreover, the bandgap mismatch between CdS and CdTe is about 10% which can cause defects at the interface that may serve as recombination centers. The thickness of CdS can be reduced to some extent but eventually leads to shunting and loss of open circuit voltage and FF [184]. This is due to the formation of pinholes that lead to the formation of TCO/CdTe weak diodes [6].

To address these problems, researchers have long been looking for alternative window layer materials. Also, alternative n-type semiconductors with larger bandgap and smaller lattice mismatch are also under study, such as CdZnS [185], $\text{CdS}_x\text{Se}_{1-x}$ [186], and CdS:O [187]. Among these, CdS:O has been deployed by several group to achieve high efficiency (>15%) devices [162, 188-190]. Improvements result from gains in current without detrimental impacts to FF or V_{OC} . As-deposited CdS:O used for optimal devices is amorphous with significant oxygen content (up to 40 at.%) which is present predominantly in the form of sulfate groups [27, 191]. It has been suggested the presence of oxygen suppress Te interdiffusion [188], but the mechanism for observed improvements has not been fully explained.

It is expected that CdS:O undergoes significant changes during the high temperature processes used in device fabrication [190, 192]. Recently developed techniques to isolate the window layer in completed devices [193] coupled to a suite of complementary characterization techniques were used to examine the transformation of this layer during high temperature device processing. It was found that extensive interdiffusion occurs, transforming the window layer into a nanocrystalline $\text{CdS}_{1-y}\text{Te}_y$ alloy, whose composition approaches solubility limits ($y \sim 0.1$). Moreover significant oxygen is retained in the form of CdSO_4 clusters that are dispersed throughout the alloy layer [194]. Observed improvements in blue response are attributed to an effective reduction in the window layer thickness and improved transparency as the sulfate clusters are transparent to visible radiation.

The high efficiency suggests that these sulfate clusters are relatively benign, but it motivated us to explore the use of pre-formed $\text{CdS}_{1-y}\text{Te}_y$ alloy window layers without oxygen present. It is well known that during the device fabrication $\text{CdS}_{1-y}\text{Te}_y$ alloy will be formed because of the interdiffusion of CdS and CdTe [29, 195] which causes a reduction in the lattice mismatch at CdS/CdTe junction [29] and a reduction of recombination [30]. In fact the buried p-n junction interface is expected to be found in this interdiffused region [196]. While a degree of interdiffusion is regarded to be beneficial, excessive interdiffusion is detrimental, and it is generally thought that it is critical to maintain an intrinsic CdS layer adjacent to the tin oxide contact [197, 198]. As such the direct use of $\text{CdS}_{1-y}\text{Te}_y$ alloys as a window is somewhat counter intuitive. Tellurium incorporation further reduces the band gap [199], which might be expected to additionally attenuate the blue response. $\text{CdS}_{1-y}\text{Te}_y$ alloys have been explored as absorbers [200] and used as an interlayer between CdS and CdTe to reduce the degree of interdiffusion [201], but to the best of our knowledge they have not been used directly as a substitute for the CdS window layer. Alloys were deposited by co-evaporation. We evaluate the intrinsic properties of these layers and then incorporate them into device fabrication for comparison with standard CdS-based devices. Analysis of the resulting J-V and QE are used to better understand the role of these materials.

8.2 Materials and Methods

$\text{CdS}_{1-y}\text{Te}_y$ alloys were deposited by co-evaporation of CdS and CdTe on TEC-15 glass

from Pilkington at 150 °C. The change of band gap and formation of $\text{CdS}_{1-y}\text{Te}_y$ alloys were measured by UV-Vis spectroscopy and X-ray diffraction (XRD). These windows layers were then incorporated into standard device processing. A 3.5 micron CdTe absorber layer was grown by vapor transport deposition at $T = 450$ °C. CdCl_2 treatment was applied at 400 °C for 30 min by using a close spaced sublimation geometry in a tube furnace under a 50-50% O_2/N_2 ambient. The back surface was etched in a 0.05 vol.% bromine methanol solution for 10 s and rinsed with methanol. A ZnTe:Cu buffer layer was deposited by thermal co-evaporation, followed by evaporation of a 100 nm Au layer. Device activation employed a 30 s RTP treatments under flowing Ar as described previously [65]. The solar cell performance was measured under simulated AM1.5 radiation using a commercial tool that is calibrated using a certified silicon standard (PV Measurements). Quantum efficiency (QE) was measured on a custom system with a grating monochromator and lock-in amplifier detection.

8.3 Results and Discussion

$\text{CdS}_{1-y}\text{Te}_y$ alloy films were deposited by co-evaporation. Figure 8-1 shows photographs of the as-deposited alloys explored in this work. The total thickness was fixed at 150 nm and the nominal CdTe content varied from 0-15 nm. The flux of CdTe and CdS were controlled by independent quartz crystal microbalances (QCM) and the value of y in Figure 8-1 indicates the individual alloy composition assuming equivalent incorporation of both species after accounting for their densities. This range was chosen to span the range of alloy solubility at our processing temperature (450 °C). This figure shows that with the increase of CdTe content, the color changes from the characteristic yellow hue of CdS to orange and brown with increasing Te content.

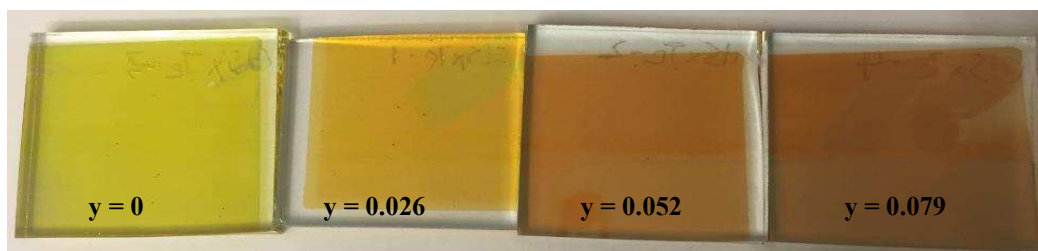


Figure 8-1: Photographs of as-deposited $\text{CdS}_{1-y}\text{Te}_y$ alloys.

The transmission of these films was quantified by UV-Vis spectroscopy as shown in Figure 8-2. Consistent with the photographs of Figure 8-1 it is observed that the band edge is shifted to higher wavelengths with increasing Te content, but interestingly there is also a marked improvement in sub-band gap transmission. This may reflect improved quality of the alloys relative to CdS through a reduction in optically-active defect states.

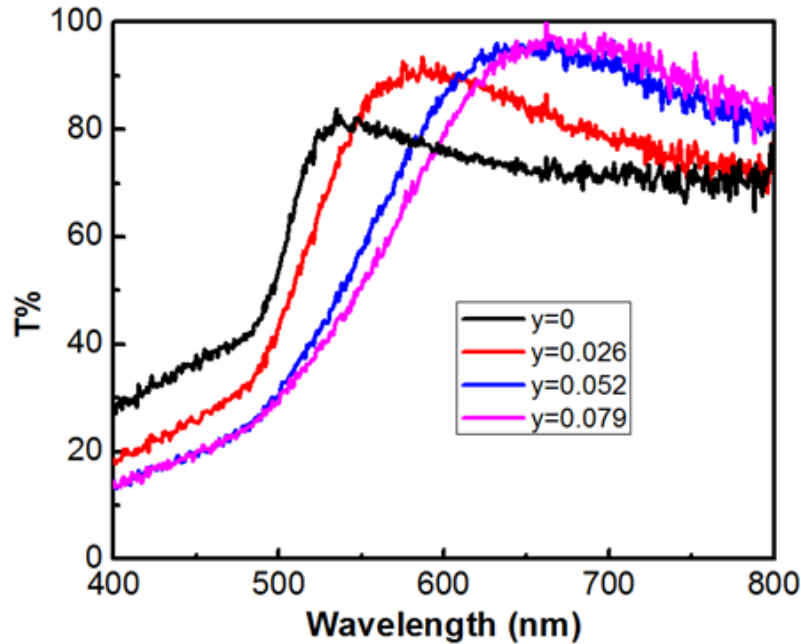


Figure 8-2: The transmission of CdS_{1-y}Te_y films with different y values.

The bandgaps of these films can be interpreted from their transmission spectra by using Tauc relation: plot $(\alpha h\nu)^n$ vs $h\nu$, where $\alpha = 2.303 \log (T/d)$, d is the thickness of the film and $n=2$ for direct bandgap semiconductors. The values of the optical band gap (E_g) can be estimated by taking the intercept of the extrapolation to zero absorption with photon energy axis. Then, the value of y can be calculated by using the well-established relationships for CdS-CdTe alloys: $E_g(y) = E_2 + (E_1 - E_2 - b)y + by^2$, where E_1 and E_2 are the bandgaps of CdS and CdTe respectively and b is 1.8 eV [199]. We assumed the bandgap of CdS is 2.4 eV and CdTe is 1.51 eV and got the values of y to compare with the values we got from the thickness. Figure 8-3 compares the alloy composition based on QCM with those extracted from the Tauc analysis. It is observed that the alloy composition based on band gap is systematically greater than the value expected based on QCM measurements. This suggests that CdTe is

incorporated into the alloy films with greater probability than CdS, which is somewhat surprising as you might expect the opposite based on their vapor pressure. XRD analysis shown in Figure 8-4 confirms that all films display the polycrystalline, wurtzite structure of intrinsic CdS. Over the range explored there is no significant change in structure with the addition of Te.

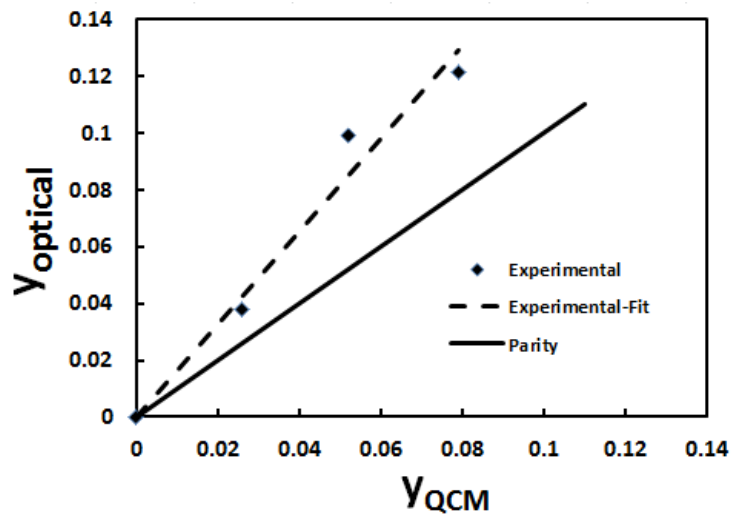


Figure 8-3: Parity plot comparing CdS_{1-y}Te_y alloy composition derived from QCM measurements with those based on measurement of the optical band gap.

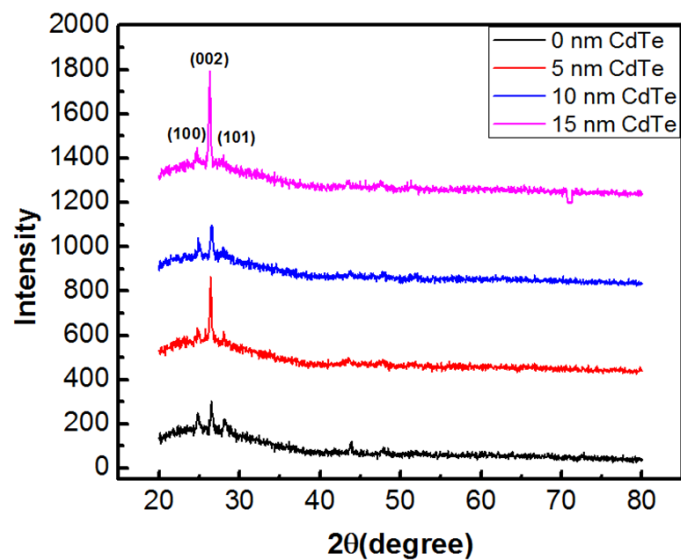


Figure 8-4: XRD analysis of the as-deposited alloy films.

Devices were then completed using these window layers. In each case the thickness of the as-deposited window layer was fixed at 150 nm. With the exception of Te content all

other parameters were held constant. Figure 8-5 displays box plots of the resulting efficiency and secondary device parameters (J_{SC} , V_{OC} , FF) based on measurements of 5-8 devices from each sample. Here again the alloy composition is based on QCM measurements. Interestingly there is no change in device efficiency until the highest alloy composition at $y = 0.079$. Note that the highest level may exceed Te solubility limits and may undergo some level of phase segregation during device processing. Even more interesting is the variation in the secondary parameters. Despite the reduction in band gap, there are significant increases in J_{SC} with increasing Te content. However this improvement is offset by modest decreases in both V_{OC} and FF. The QE analysis is quite consistent with the changes in J_{SC} , as both improve monotonically with higher Te content. The improvement in the sub-bandgap region is in agreement with the optical transmission measurements shown in Figure 8-2, but the improvement in the blue region is surprising. With the reduced band gap one would expect a decrease in blue QE, but the opposite is observed. This suggests that the alloy itself may be contributing to the generation of photocurrent. Another odd feature in the QE is the response at the band edge. There is a small but systematic red-shift in the band edge as Te is added to the window. This observation is also counter intuitive. Sulfur diffusion into the CdTe absorber would reduce its band gap, due to bowing effects [199].

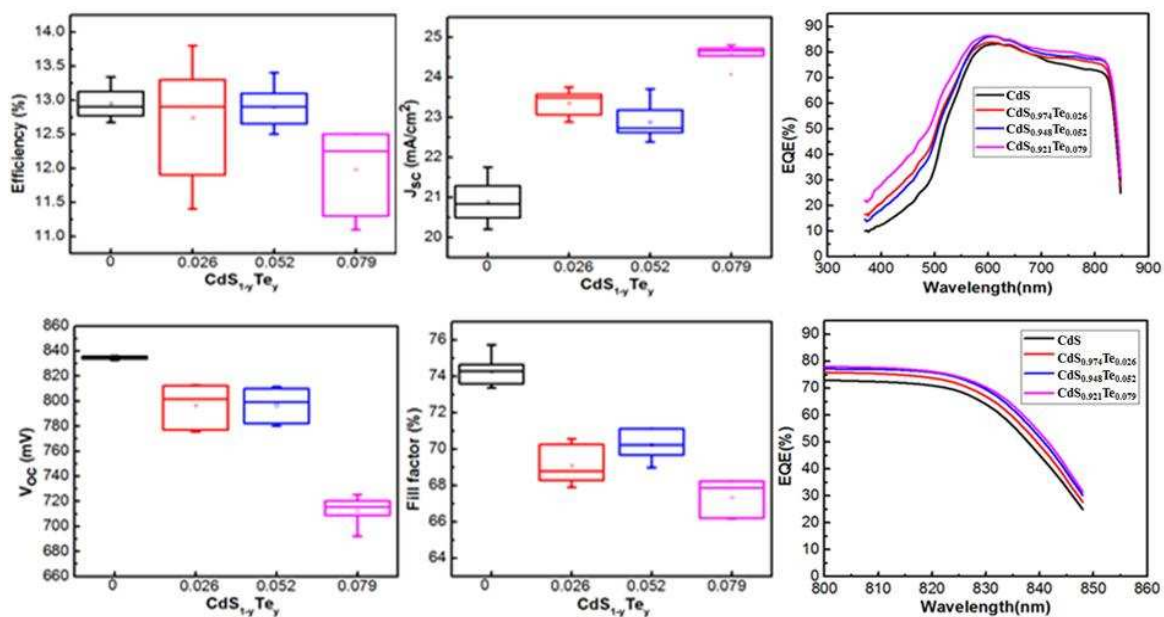


Figure 8-5: Box plots of J-V parameters and QE spectra of devices made with $CdS_{1-y}Te_y$ alloys.

However, the degree of sulfur diffusion is expected to be reduced in the case of alloy window layers relative to CdS. So the opposite trend would be expected.

To examine the degree of interdiffusion with CdTe in more detail we used X-ray diffraction (XRD). To provide access to the window layer region in completed devices we made use of a recently developed liftoff technique developed by Meysing and co-workers [193]. This technique cleanly separates the devices at the tin oxide|CdS interface, as shown in Figure 8-6, facilitating access for characterization of this region. Figure 8-6 compares high resolution XRD scans of the CdTe (411) peak from a standard CdS device and an alloy-based devices ($\text{CdS}_{0.948}\text{Te}_{0.052}$). This figure captures reflections from the CdTe absorber beneath the thin window layer. In the case of the baseline Cd device, two distinct peaks are observed. One is from the intrinsic CdTe film and the shoulder at higher 2θ is due to the presence of a $\text{CdS}_{1-y}\text{Te}_y$ alloy formed by diffusion S into the CdTe lattice as well documented [198]. In contrast, in the pattern from the alloy-based device only the intrinsic CdTe reflection is observed, showing that interdiffusion has largely been suppressed as one might expect. Again this does not explain the red shift observed in the band edge of alloy-based devices. Additional studies will need to be done to better understand this behavior.

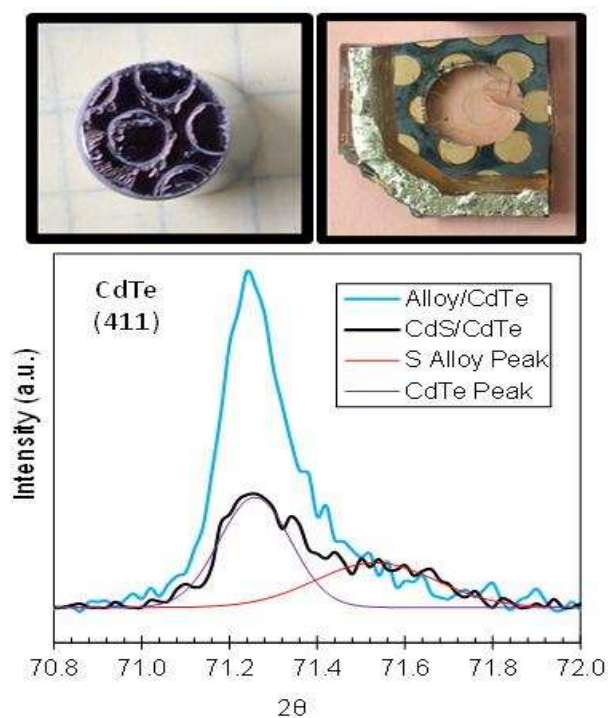


Figure 8-6: Liftoff method and XRD of liftoff samples.

8.4 Summary and Conclusions

CdS_{1-y}Te_y alloys with different compositions were deposited by co-evaporation and substituted for CdS as window layers for device fabrication. Despite the expected reduction in band gap alloy-based devices display markedly improved J_{SC} that overcomes losses in V_{OC} and FF. The blue response improves in alloy-based devices, suggesting that the alloy may contribute to photogeneration of carriers. The gains in J_{SC} are consistent with transmission spectra of the as-deposited films. CdS_{1-y}Te_y alloy formation has generally been viewed as detrimental. However these results show that this is not necessarily the case and that as additional opto-electronic property considerations are critical as well. In addition XRD analysis of interdiffusion with CdTe shows that this is largely suppressed in alloy-based devices. This suggests opportunities to design and fabricate new CdTe architectures through judicious use of pre-formed alloys and composition gradients.

CHAPTER 9

SUMMARY OF RESULTS AND RECOMMENDATIONS FOR FUTURE WORK

This chapter presents major results from Chapters 3–8 and recommendations for future work.

9.1 Summary of Results

This work mainly focuses on improving and understanding the processing and performance of cadmium telluride solar cells coated with copper doped zinc telluride buffer layer.

9.1.1 Development of the RTP Treatments

We developed an RTP-based process for back contact preparation that de-couples Cu deposition from its re-distribution and significantly reduces the process time. The ZnTe:Cu buffer layer is co-evaporated at low temperature, with little or no interdiffusion. After physical vapor deposition of gold metallization layer, the sample is then subjected to short RTP treatment(s) (30 s) to activate the junction. The buffer layer composition, thickness, and RTP parameters were optimized and substantial improvements in both FF (>73%) and V_{OC} (>850 mV) were obtained. To further prove that our back contact process is robust, reliable, and transferrable, we applied our back contact on the CdTe provided by different groups including NREL, Reel Solar Inc. and EPI Solar and made by different methods. Significant improvements were obtained with each sample including an NREL certified flexible CdTe solar cell with 16.4% efficiency. This process was demonstrated to be beneficial on multiple device structures, as the low thermal budget of RTP facilitates its adoption without impacting the optimization of upstream processing. Our work showed that the fraction of Cu in the ZnTe buffer was critical, but its initial distribution or the thickness of the buffer layer was not critical. We have demonstrated that thermal evaporation combined with RTP processing is an effective approach for fabricating back contacts for CdTe solar cells.

9.1.2 Study of the Back Contact

To understand the materials science related to the RTP treated ZnTe:Cu back contact process, a lot of characterization techniques were used. The changes of optoelectronic properties during RTP treatments were characterized by QE, C-V, and TRPL, while compositional changes were studied by using SIMS and APT. The results showed that the dramatic improvements after optimal RTP treatments in V_{OC} and τ are attributed to the elimination of barriers and mitigation of surface recombination in the back contact region. Analysis of SIMS profiles suggest that the Au metallization layer serves as a sink for much of the Cu supplied in the buffer, and that the degree of copper migration into the CdTe is substantially reduced relative to conventional thermal activation. APT reveals that the nanoscale heterogeneity of this back contact and the dramatic elemental redistribution occurs during brief RTP treatments. Further characterizations including HR-TEM and APT were used and found that core-shell nanostructures consisting of $Cu_{1.4}Te$ clusters encased in Zn were formed after optimal RTP treatments. Formation of such structures may effectively sequester copper and limit its migration into CdTe, accounting for improved stability. With its low thermal budget the RTP process has been successfully applied to multiple device architectures, including devices with certified efficiencies in excess of 16%.

9.1.3 Metallization Materials and Reliability Tests

Au is commonly used as the metallization layer in research labs because of its high work function (5.2 eV), stability in air and, ease of deposition. But Au is not compatible with industrial manufacturing because of its high price. So, we explored two low cost metals, Cr and Ti, as the potential alternatives for Au. 150 nm of different metallization layers were applied at room temperature. Au and Cr were deposited by thermal evaporation while magnetron sputtering was employed for Ti. The Cu content in the ZnTe buffer layer was optimized with different metals. The optimal Cu loading decreased from 15 to 10 to 5 nm for Au, Ti and Cr, respectively. Both the order and amounts are consistent with the solubility Cu in these metals. Reliability tests were taken using optimized devices under different stressing conditions. Losses under light soaking condition are primarily due to V_{OC} while losses in dark are similar among metals which are primarily due to FF, and J_{SC} is generally unchanged.

Good cells stabilize after 5 hours, poor cells after 50 hours. Ti appears to be most promising. Although the optimal Cu content for the sample with Ti is 10 nm which is higher than the sample with Cr, it has the best stability among three samples. The reliability test shows the Cu-Metal interaction is important. In this work we explore chromium and titanium as more practical alternatives. It was found that comparable performance could be obtained with each metal, but that the optimal Cu loading scaled as one would expect based on solubility. Comparisons of current-voltage and quantum efficiency behavior among devices produced with insufficient, optimal, and excess Cu dosing are used to provide insight into the role(s) of this critical impurity for device performance.

9.1.4 CdS_{1-y}Te_y Alloy Window Layers

My colleague Daniel Meysing studied the evolution of CdS:O after device fabrication showed that extensive interdiffusion occurs and CdS_{1-y}Te_y alloys, whose composition approaches solubility limits, are formed. Moreover significant oxygen is retained in the form of CdSO₄ clusters dispersed throughout the alloy layer. So, instead of relying on interdiffusion, we explored the use of pre-formed CdS_{1-y}Te_y alloy window layers without oxygen present. Alloys with different CdS and CdTe compositions were deposited by co-evaporation. We evaluate the intrinsic properties of these layers and then incorporate them into device fabrication for comparison with standard CdS-based devices. Transmission curves showed that with the increase of Te content, the band gap of as-deposited films was decreased. But, the alloy-based devices display markedly improved J_{SC} that overcomes losses in V_{OC} and FF. Liftoff technique was used to provide direct access to CdS/CdTe interface after device fabrication. XRD analysis of interdiffusion with CdTe showed that it is largely suppressed in alloy-based devices. This work suggested opportunities to design and fabricate new CdTe architectures through judicious use of preformed alloys and composition gradients.

9.2 Recommendations for Future Work

The following subsections outline future work areas that would provide an extension of this work and/or are suggested by results from this work.

9.2.1 HRT with Alloy Window Layers

HRT is always employed with thinner CdS, because weak TCO/CdTe diodes form with thin and non-uniform CdS. Those diodes are connected in parallel with the CdS/CdTe diodes and cause low V_{OC} . Theoretical calculations show that an inhomogeneous device modeled by a parallel connection of solar cells with a distribution of diode parameters can benefit from an additional series resistance [28]. This problem is critical since we are using $CdS_{1-y}Te_y$ alloys as the window layer. An HRT layer is an effective way to use thinner window layer and prevent the formation of TCO/CdTe diodes. First, we need to make samples with different CdS thicknesses on HRT to find the optimized thickness. Then we can apply HRT to devices with alloy window layers and find the best conditions. These devices can be characterized with J-V, QE, C-V, XRD and so on to compare.

9.2.2 MgZnO as the Window Layer

First Solar's QE shows that they are using an alternative to CdS, whose bandgap is not high enough which causes the largest J_{SC} loss in a conventional CdTe device [81]. In addition to that, CdS is also the reason for delamination at high $CdCl_2$ treatment temperature which is necessary for defects passivation, better carrier lifetime and higher V_{OC} . Recently, the group at CSU has successfully used high bandgap magnesium zinc oxide (MZO) as the alternative window layer to CdS [83]. Based on this paper, we will make a target with a composition of 11 wt.% MgO with 89% ZnO. MgZnO films will be deposited using RF planar sputter deposition process. The gas pressure will be kept at 5 mTorr with a composition of 1% oxygen in argon. [83]. Firstly, a 500 nm MZO film will be sputtered on glass. UV-vis can be used to determine the bandgap, while EDX can be used to measure the composition of the film. Then, different thicknesses of MZO films, such as 50, 75, 100, 125, 150 nm, can be sputtered on HRT coated FTO glasses and fabricate to devices. JV and QE can be used to characterize if the J_{SC} and the blue QE is increased. After the thickness is optimized, we should try higher $CdCl_2$ treatment temperatures, such as 425, 450, 475 and 500 °C, to see if devices with MZO as the window layer can stand higher $CdCl_2$ treatment temperature without delamination. TRPL and JV can be used to see if the carrier lifetime is increased and so is the V_{OC} .

9.2.3 Ternary Alloys as the Absorber

With CdS_{1-y}Te_y alloy window layers, we showed opportunities to design and fabricate new CdTe architectures through judicious use of preformed alloys and composition gradients. Recently First Solar announced that they are using graded CdSe_{1-y}Te_y as their absorber to get enhanced red absorption [80]. They substituted tellurium with selenide to build a ternary compound with lower bandgap. Because of the bandgap of CdTe is 1.45 eV, red photons above 860 nanometers in wavelength are inaccessible to CdTe. With a reduction of the material bandgap toward the front of the device, those red photons can be absorbed and converted contribution to the short circuit current. They also showed that using graded CdSe_{1-y}Te_y increased their carrier lifetime by enhancing absorber quality [80]. Better than CdS_{1-y}Te_y, CdSe_{1-y}Te_y has smaller miscible gap, which allows the film has a homogeneous predominant wurtzite structure for $0.7 \leq y \leq 1$ regions and lower bandgap with the addition of some Se [202, 203]. Based on this idea, we can gradually control and increase the value of y, from about 0.7 to 1, during the deposition. As-deposited film can be characterized with XRD, SEM, SIMS and UV-vis to characterize the crystal structure, morphology, composition and bandgap. The composition, deposition rate, substrate temperature and the film thickness will be optimized. Devices can be characterized with JV, QE, TRPL to see if the J_{SC}, the blue QE, the carrier lifetime and the V_{OC} are increased.

9.2.4 Back Contact without Cu

Even though ZnTe helps to restrain Cu in the buffer layer and improve the reliability, Cu is still a potential adverse factor for CdTe devices. The ultimate way to solve this problem is to eliminate Cu. The function of Cu in ZnTe is to degenerately dope ZnTe to p-type, which can be done by other elements, such as Cl, N [204, 205] and P [206, 207]. The success of NREL in doping single crystalline CdTe with P and getting over 900 mV V_{OC} [208] gives us the idea of doping ZnTe with P. Instead of co-evaporating ZnTe and Cu, which we are currently doing, we can co-evaporate ZnTe and Zn₃P₂. Zn₃P₂ is tetragonal at a room temperature and has similar melting point (1160 °C) with ZnTe. We can still keep the thickness of ZnTe at 150 nm and control the thickness Zn₃P₂ to get ZnTe:P films with different P concentrations, such as 5, 10, 15, 20, 25 nm of Zn₃P₂. XRD, HALL, four-point

probe and ICP and be used to characterize the crystal structure, carrier concentration, sheet resistance and P concentration of the film. Then these films can be integrated into devices. JV and QE can be used to measure the performance of the devices. After optimizing P concentration, the substrate temperature and the film thickness can also be optimized. The performance will be compared to the device with Cu and explain the deference. Stability tests will be carried out with both devices with P and Cu and the JV performance during the test will be compared.

REFERENCES CITED

- [1] <http://www.whitehorse.vic.gov.au/IgnitionSuite/uploads/docs/Sustainable Living Guide Energy.pdf>
- [2] All fossil fuel reserve and consumption data from CIA World Factbook.
- [3] <https://www.ecotricity.co.uk/our-green-energy/energy-independence/the-end-of-fossil-fuel>.
- [4] S. Solomon, G.-K. Plattner, R. Knutti, and P. Friedlingstein, "Irreversible climate change due to carbon dioxide emissions," *Proceedings of the national academy of sciences*, p. pnas. 0812721106, 2009.
- [5] <http://org.ntnu.no/solarcells/pages/generations.php>
- [6] R. R. Lunt, T. P. Osedach, P. R. Brown, J. A. Rowehl, and V. Bulović, "Practical roadmap and limits to nanostructured photovoltaics," *Advanced Materials*, vol. 23, pp. 5712-5727, 2011.
- [7] F. Solar, "FIRST SOLAR ACHIEVES YET ANOTHER CELL CONVERSION EFFICIENCY WORLD RECORD," ed, 2016.
- [8] http://www.nrel.gov/ncpv/images/efficiency_chart.jpg
- [9] L. M. Peter, "Towards sustainable photovoltaics: the search for new materials," *Philosophical Transactions of the Royal Society a-Mathematical Physical and Engineering Sciences*, vol. 369, pp. 1840-1856, May 13 2011.
- [10] <http://www.hirschmann-inc.com/en-US/Wissen/Qualitaetsmanagement/GlasArten.aspx>
- [11] A. Morales-Acevedo, "Thin film CdS/CdTe solar cells: research perspectives," *Solar Energy*, vol. 80, pp. 675-681, 2006.
- [12] E. Fortunato, D. Ginley, H. Hosono, and D. C. Paine, "Transparent conducting oxides for photovoltaics," *MRS bulletin*, vol. 32, pp. 242-247, 2007.
- [13] D. S. Ginley and C. Bright, "Transparent conducting oxides," *Mrs Bulletin*, vol. 25, pp. 15-18, 2000.
- [14] X. Wu, W. Mulligan, and T. Coutts, "Recent developments in RF sputtered cadmium stannate films," *Thin Solid Films*, vol. 286, pp. 274-276, 1996.
- [15] X. Li, T. A. Gessert, and T. Coutts, "The properties of cadmium tin oxide thin-film compounds prepared by linear combinatorial synthesis," *Applied Surface Science*, vol. 223, pp. 138-143, 2004.
- [16] X. Li, R. Ribelin, Y. Mahathongdy, D. Albin, R. Dhere, D. Rose, *et al.*, "The Effect of High-Resistance SnO₂ on CdS/CdTe Device Performance," in *AIP Conference Proceedings*, 1998, pp. 230-235.
- [17] T. Minami, H. Sonohara, S. Takata, and H. Sato, "Highly transparent and conductive

- zinc-stannate thin films prepared by RF magnetron sputtering," *Japanese journal of applied physics*, vol. 33, p. L1693, 1994.
- [18] J. Britt and C. Ferekides, "THIN-FILM CDS/CDTE SOLAR-CELL WITH 15.8-PERCENT EFFICIENCY," *Applied Physics Letters*, vol. 62, pp. 2851-2852, May 31 1993.
- [19] A. D. Compaan, A. Gupta, S. Lee, S. Wang, and J. Drayton, "High efficiency, magnetron sputtered CdS/CdTe solar cells," *Solar Energy*, vol. 77, pp. 815-822, 2004.
- [20] J. Li, J. D. Beach, C. A. Wolden, and Ieee, "Rapid Thermal Processing of ZnTe:Cu Contacted CdTe Solar Cells," *2014 Ieee 40th Photovoltaic Specialist Conference (Pvsc)*, pp. 2360-2365, 2014 2014.
- [21] T. Aramoto, S. Kumazawa, H. Higuchi, T. Arita, S. Shibutani, T. Nishio, *et al.*, "16.0% efficient thin-film CdS/CdTe solar cells," *Japanese Journal of Applied Physics*, vol. 36, p. 6304, 1997.
- [22] N. Romeo, A. Bosio, V. Canevari, and A. Podesta, "Recent progress on CdTe/CdS thin film solar cells," *Solar Energy*, vol. 77, pp. 795-801, 2004.
- [23] S. Galloway, P. R. Edwards, and K. Durose, "Characterisation of thin film CdS/CdTe solar cells using electron and optical beam induced current," *Solar Energy Materials and Solar Cells*, vol. 57, pp. 61-74, 1999.
- [24] M. Tashkandi and W. Sampath, "Morphology of CdS thin films: Pinholes and their effect on open circuit Voltage in CdS/CdTe solar cells," in *Photovoltaic Specialists Conference (PVSC), 2011 37th IEEE*, 2011, pp. 001700-001704.
- [25] S. G. Kumar and K. S. R. K. Rao, "Physics and chemistry of CdTe/CdS thin film heterojunction photovoltaic devices: fundamental and critical aspects," *Energy & Environmental Science*, vol. 7, pp. 45-102, Jan 2014.
- [26] X. Wu, "High-efficiency polycrystalline CdTe thin-film solar cells," *Solar energy*, vol. 77, pp. 803-814, 2004.
- [27] D. M. Meysing, C. A. Wolden, M. M. Griffith, H. Mahabaduge, J. Pankow, M. O. Reese, *et al.*, "Properties of reactively sputtered oxygenated cadmium sulfide (CdS:O) and their impact on CdTe solar cell performance," *Journal of Vacuum Science & Technology A*, vol. 33, Mar 2015.
- [28] P. Grabitz, U. Rau, and J. Werner, "A multi-diode model for spatially inhomogeneous solar cells," *Thin Solid Films*, vol. 487, pp. 14-18, 2005.
- [29] D. Lane, J. Painter, M. Cousins, G. Conibeer, and K. Rogers, "Sulfur diffusion in cadmium telluride thin films: Part 1: the grain boundary diffusion coefficient," *Thin Solid Films*, vol. 431, pp. 73-77, 2003.
- [30] D. Oman, K. Dugan, J. Killian, V. Ceekala, C. Ferekides, and D. Morel, "Reduction of recombination current in CdTe/CdS solar cells," *Applied physics letters*, vol. 67, pp. 1896-1898, 1995.
- [31] R. Radojcic, A. Hill, and M. Hampshire, "Preparation and properties of mixed CdS x

- Ter 1– x thin films," *Solar Cells*, vol. 4, pp. 101-107, 1981.
- [32] W. A. Pinheiro, V. D. Falcão, L. R. d. O. Cruz, and C. L. Ferreira, "Comparative study of CdTe sources used for deposition of CdTe thin films by close spaced sublimation technique," *Materials Research*, vol. 9, pp. 47-49, 2006-03 2006.
- [33] C. S. Ferekides, D. Mariniski, V. Viswanathan, B. Tetali, V. Palekis, P. Selvaraj, *et al.*, "High efficiency CSSCdTe solar cells," *Thin Solid Films*, vol. 361, pp. 520-526, Feb 21 2000.
- [34] J. M. Kestner, S. McElvain, S. Kelly, T. R. Ohno, L. M. Woods, and C. A. Wolden, "An experimental and modeling analysis of vapor transport deposition of cadmium telluride," *Solar Energy Materials and Solar Cells*, vol. 83, pp. 55-65, Jun 1 2004.
- [35] G. Fulop, M. Doty, P. Meyers, J. Betz, and C. Liu, "High-efficiency electrodeposited cadmium telluride solar cells," *Applied Physics Letters*, vol. 40, pp. 327-328, 1982.
- [36] A. Romeo, A. Terheggen, D. Abou-Ras, D. L. Batzner, F. J. Haug, M. Kalin, *et al.*, "Development of thin-film Cu(In,Ga)Se-2 and CdTe solar cells," *Progress in Photovoltaics*, vol. 12, pp. 93-111, Mar-May 2004.
- [37] H. Moutinho, M. Al-Jassim, D. Levi, P. Dippo, and L. Kazmerski, "Effects of CdCl₂ treatment on the recrystallization and electro-optical properties of CdTe thin films," *Journal of Vacuum Science & Technology A*, vol. 16, pp. 1251-1257, 1998.
- [38] C. Li, Y. Wu, J. Poplawsky, T. J. Pennycook, N. Paudel, W. Yin, *et al.*, "Grain-boundary-enhanced carrier collection in CdTe solar cells," *Physical review letters*, vol. 112, p. 156103, 2014.
- [39] T. C. Anthony, A. L. Fahrenbruch, and R. H. Bube, "LOW RESISTANCE CONTACTS TO P-TYPE CADMIUM TELLURIDE," *Journal of Electronic Materials*, vol. 11, pp. 89-109, 1982 1982.
- [40] D. H. Rose, F. S. Hasoon, R. G. Dhere, D. S. Albin, R. M. Ribelin, X. S. Li, *et al.*, "Fabrication procedures and process sensitivities for CdS/CdTe solar cells," *Progress in Photovoltaics*, vol. 7, pp. 331-340, Sep-Oct 1999.
- [41] J. P. Ponpon, "A REVIEW OF OHMIC AND RECTIFYING CONTACTS ON CADMIUM TELLURIDE," *Solid-State Electronics*, vol. 28, pp. 689-706, 1985 1985.
- [42] T. A. Gessert, A. R. Mason, P. Sheldon, A. B. Swartzlander, D. Niles, and T. J. Coutts, "Development of Cu-doped ZnTe as a back-contact interface layer for thin-film CdS/CdTe solar cells," *Journal of Vacuum Science & Technology a-Vacuum Surfaces and Films*, vol. 14, pp. 806-812, May-Jun 1996.
- [43] A. Mondal, B. E. McCandless, and R. W. Birkmire, "ELECTROCHEMICAL DEPOSITION OF THIN ZNTE FILMS AS A CONTACT FOR CDTE SOLAR-CELLS," *Solar Energy Materials and Solar Cells*, vol. 26, pp. 181-187, Apr 1992.
- [44] D. Rioux, D. W. Niles, and H. Hochst, "ZNTE - A POTENTIAL INTERLAYER TO FORM LOW-RESISTANCE BACK CONTACTS IN CDS/CDTE SOLAR-CELLS,"

Journal of Applied Physics, vol. 73, pp. 8381-8385, Jun 15 1993.

- [45] B. E. McCandless and K. D. Dobson, "Processing options for CdTe thin film solar cells," *Solar Energy*, vol. 77, pp. 839-856, 2004 2004.
- [46] J.-q. Zhang, L.-h. Feng, W. Cai, J.-g. Zheng, Y.-p. Cai, B. Li, *et al.*, "The structural phase transition and mechanism of abnormal temperature dependence of conductivity in ZnTe: Cu polycrystalline thin films," *Thin Solid Films*, vol. 414, pp. 113-118, 2002.
- [47] X. Feng, K. Singh, S. Bhavanam, V. Palekis, D. L. Morel, and C. Ferekides, "Preparation and characterization of ZnTe as an interlayer for CdS/CdTe substrate thin film solar cells on flexible substrates," *Thin Solid Films*, vol. 535, pp. 202-205, 2013.
- [48] C. Narayanswamy, T. Gessert, and S. Asher, "Analysis of Cu diffusion in ZnTe-based contacts for thin-film CdS/CdTe solar cells," in *AIP Conference Proceedings*, 1998, pp. 248-253.
- [49] S. H. Kim, J. H. Ahn, H. S. Kim, H. M. Lee, and D. H. Kim, "The formation of ZnTe: Cu and Cu_xTe double layer back contacts for CdTe solar cells," *Current Applied Physics*, vol. 10, pp. S484-S487, 2010.
- [50] L. Feng, D. Mao, J. Tang, R. Collins, and J. Trefny, "The structural, optical, and electrical properties of vacuum evaporated Cu-doped ZnTe polycrystalline thin films," *Journal of electronic materials*, vol. 25, pp. 1422-1427, 1996.
- [51] H. Chou, A. Rohatgi, E. Thomas, S. Kamra, and A. Bhat, "Effects of Cu on CdTe/CdS heterojunction solar cells with Au/Cu contacts," *Journal of The Electrochemical Society*, vol. 142, pp. 254-259, 1995.
- [52] S. H. Demtsu, D. S. Albin, J. R. Sites, W. K. Metzger, and A. Duda, "Cu-related recombination in CdS/CdTe solar cells," *Thin Solid Films*, vol. 516, pp. 2251-2254, Feb 29 2008.
- [53] K. D. Dobson, I. Visoly-Fisher, G. Hodes, and D. Cahen, "Stability of CdTe/CdS thin-film solar cells," *Solar Energy Materials and Solar Cells*, vol. 62, pp. 295-325, 2000.
- [54] S. H. Wei and S. B. Zhang, "Chemical trends of defect formation and doping limit in II-VI semiconductors: The case of CdTe," *Physical Review B*, vol. 66, Oct 15 2002.
- [55] J. Laurenti, G. Bastide, M. Rouzeyre, and R. Triboulet, "Localized defects in p-CdTe: Cu doped by copper incorporation during Bridgman growth," *Solid state communications*, vol. 67, pp. 1127-1130, 1988.
- [56] D. Krasikov, A. Knizhnik, B. Potapkin, S. Selezneva, and T. Sommerer, "First-principles-based analysis of the influence of Cu on CdTe electronic properties," *Thin Solid Films*, vol. 535, pp. 322-325, 2013.
- [57] F. H. Seymour, V. Kaydanov, T. R. Ohno, and D. Albin, "Cu and CdCl₂ influence on defects detected in CdTe solar cells with admittance spectroscopy," *Applied Physics Letters*, vol. 87, p. 153507, 2005.
- [58] A. Balcioglu, R. K. Ahrenkiel, and F. Hasoon, "Deep-level impurities in CdTe/CdS

- thin-film solar cells," *Journal of Applied Physics*, vol. 88, pp. 7175-7178, Dec 15 2000.
- [59] S.-H. Wei, S. Zhang, and A. Zunger, "First-principles calculation of band offsets, optical bowings, and defects in CdS, CdSe, CdTe, and their alloys," *Journal of applied Physics*, vol. 87, pp. 1304-1311, 2000.
- [60] J. Zhou, X. Wu, A. Duda, G. Teeter, and S. H. Demtsu, "The formation of different phases of Cu_xTe and their effects on CdTe/CdS solar cells," *Thin Solid Films*, vol. 515, pp. 7364-7369, Jun 25 2007.
- [61] T. Gessert, A. Mason, P. Sheldon, A. Swartzlander, D. Niles, and T. Coutts, "Development of Cu-doped ZnTe as a back-contact interface layer for thin-film CdS/CdTe solar cells," *Journal of Vacuum Science & Technology A*, vol. 14, pp. 806-812, 1996.
- [62] P.V. Meyers, M.M. Al-Jassim, S. Asher, in: D. Ginley, A. Catalano, H.W. Schock, C. Eberspacher, T.M. Peterson, T. Wada, (Eds.), *Proceedings of the Symposium on Thin Films for Photovoltaic and Related devices – MRS Spring Meeting, San Francisco, CA, 1996*.
- [63] D. H. Levi, L. Woods, D. Albin, T. Gessert, R. Reedy, and R. Ahrenkiel, *The influence of grain boundary diffusion on the electro-optical properties of CdTe/CdS solar cells: National Renewable Energy Laboratory, 1998*.
- [64] V. Singh, O. Erickson, and J. Chao, "Analysis of contact degradation at the CdTe-electrode interface in thin film CdTe-CdS solar cells," *Journal of applied physics*, vol. 78, pp. 4538-4542, 1995.
- [65] J. Li, D. R. Diercks, T. R. Ohno, C. W. Warren, M. C. Lonergan, J. D. Beach, *et al.*, "Controlled activation of ZnTe:Cu contacted CdTe solar cells using rapid thermal processing," *Solar Energy Materials and Solar Cells*, vol. 133, pp. 208-215, Feb 2015.
- [66] S. H. Demtsu, D. S. Albin, J. W. Pankow, and A. Davies, "Stability study of CdS/CdTe solar cells made with Ag and Ni back-contacts," *Solar Energy Materials and Solar Cells*, vol. 90, pp. 2934-2943, Nov 6 2006.
- [67] T. A. Gessert and T. J. Coutts, "DEVELOPMENT AND ANALYSIS OF CU-DOPED ZNTE FOR USE AS A BACK CONTACT INTERFACE FOR CDS/CDTE SOLAR-CELLS," in *12th Nrel Photovoltaic Program Review*, R. Noufi and H. S. Ullal, Eds., ed, 1994, pp. 345-353.
- [68] N. Romeo, A. Bosio, R. Tedeschi, A. Romeo, and V. Canevari, "A highly efficient and stable CdTe CdS thin film solar cell," *Solar Energy Materials and Solar Cells*, vol. 58, pp. 209-218, Jun 1999.
- [69] T. Gessert, S. Asher, S. Johnston, M. Young, P. Diplo, and C. Corwine, "Analysis of CdS/CdTe devices incorporating a ZnTe: Cu/Ti Contact," *Thin Solid Films*, vol. 515, pp. 6103-6106, 2007.
- [70] M. A. Green, K. Emery, Y. Hishikawa, and W. Warta, "Solar Cell Efficiency Tables

- (Version 33)," *Progress in Photovoltaics*, vol. 17, pp. 85-94, Jan 2009.
- [71] M. A. Green, K. Emery, Y. Hishikawa, W. Warta, and E. D. Dunlop, "Solar cell efficiency tables (version 40)," *Progress in Photovoltaics*, vol. 20, pp. 606-614, Aug 2012.
- [72] M. A. Green, K. Emery, Y. Hishikawa, W. Warta, and E. D. Dunlop, "Solar cell efficiency tables (version 41)," *Progress in Photovoltaics*, vol. 21, pp. 1-11, Jan 2013.
- [73] M. A. Green, K. Emery, Y. Hishikawa, W. Warta, and E. D. Dunlop, "Solar cell efficiency tables (version 42)," *Progress in Photovoltaics*, vol. 21, pp. 827-837, Aug 2013.
- [74] M. A. Green, K. Emery, Y. Hishikawa, W. Warta, and E. D. Dunlop, "Solar cell efficiency tables (Version 45)," *Progress in Photovoltaics*, vol. 23, pp. 1-9, Jan 2015.
- [75] M. A. Green, K. Emery, Y. Hishikawa, W. Warta, and E. D. Dunlop, "Solar cell efficiency tables (version 46)," *Progress in Photovoltaics*, vol. 23, pp. 805-812, Jul 2015.
- [76] S. H. Demtsu, J. R. Sites, and Ieee, "Quantification of losses in thin-film CdS/CdTe solar cells," in *Conference Record of the Thirty-First IEEE Photovoltaic Specialists Conference - 2005*, ed, 2005, pp. 347-350.
- [77] First Solar, Key Quarterly Financial Data, Q3, 2013
- [78] C. A. Wolden, J. Kurtin, J. B. Baxter, I. Repins, S. E. Shaheen, J. T. Torvik, *et al.*, "Photovoltaic manufacturing: Present status, future prospects, and research needs," *Journal of Vacuum Science & Technology A*, vol. 29, May 2011.
- [79] X. Wu, J. Keane, R. Dhere, C. DeHart, D. Albin, A. Duda, *et al.*, "16.5%-efficient CdS/CdTe polycrystalline thin-film solar cell," in *Proceedings of the 17th European photovoltaic solar energy conference*, 2001.
- [80] F. Solar, "Realization of the Potential of CdTe Thin-Film PV," in *43rd IEEE Photovoltaic Specialist Conference*, Portland, Oregon, 2016.
- [81] M. Gloeckler, I. Sankin, and Z. Zhao, "CdTe Solar Cells at the Threshold to 20% Efficiency," *Ieee Journal of Photovoltaics*, vol. 3, pp. 1389-1393, Oct 2013.
- [82] J. R. Sites, "Quantification of losses in thin-film polycrystalline solar cells," *Solar energy materials and solar cells*, vol. 75, pp. 243-251, 2003.
- [83] J. M. K. A. H. Munshi, A. Abbas, K. L. Barth, J. M. Walls and W. S. Sampath, "Effect of varying deposition source and substrate temperature on CSS CdTe thin-film photovoltaics," *43rd IEEE Photovoltaic Specialists Conference*, p. 5, 2016.
- [84] N. Strevel, L. Trippel, C. Kotarba, and I. Khan, "Improvements in CdTe module reliability and long-term degradation through advances in construction and device innovation," *Photovoltaic international*, 2014.
- [85] J. Sites and J. Pan, "Strategies to increase CdTe solar-cell voltage," *Thin Solid Films*, vol. 515, pp. 6099-6102, 2007.

- [86] T. Gessert, S.-H. Wei, J. Ma, D. Albin, R. Dhere, J. Duenow, *et al.*, "Research strategies toward improving thin-film CdTe photovoltaic devices beyond 20% conversion efficiency," *Solar Energy Materials and Solar Cells*, vol. 119, pp. 149-155, 2013.
- [87] J. M. Burst, W. L. Rance, T. M. Barnes, M. O. Reese, J. V. Li, D. Kuciauskas, *et al.*, "The Effect of CdTe Growth Temperature and ZnTe:Cu Contacting Conditions on CdTe Device Performance," *2012 38th Ieee Photovoltaic Specialists Conference (Pvsc)*, 2012 2012.
- [88] J. N. Duenow, R. G. Dhere, J. V. Li, M. R. Young, and T. A. Gessert, "Effects of back-contacting method and temperature on CdTe/CdS solar cells," in *Photovoltaic Specialists Conference (PVSC), 2010 35th IEEE*, 2010, pp. 001001-001005.
- [89] <http://www.greentechmedia.com/articles/read/Exclusive-First-Solars-CTO-Discusses-Record-18.6-Efficient-Thin-Film-Mod>
- [90] B. M. Kayes, N. Hui, R. Twist, S. G. Spruytte, F. Reinhardt, I. C. Kizilyalli, *et al.*, "27.6% Conversion efficiency, a new record for single-junction solar cells under 1 sun illumination," in *37th IEEE Photovoltaic Specialists Conference (PVSC)*, 2011, pp. 000004-000008.
- [91] SUBLIMATION Pavlyukevich, N. V., Polezhaev, Yury V. DOI: 10.1615/AtoZ.s.sublimation
- [92] Basics of a Quartz Crystal Microbalance. Gamry. <http://www.gamry.com>. Deakin, M.R.; Buttry, D.A. *Anal. Chem.* 1989, 61(20), 1147-1154.
- [93] Diffusion pump. https://en.wikipedia.org/wiki/Diffusion_pump.
- [94] B. N. Chapman, *Glow discharge processes*: Wiley, 1980.
- [95] J. Horzel, C. Allebe, J. Szlufcik, and S. Sivoththaman, "Development of RTP for industrial solar cell processing," *Solar energy materials and solar cells*, vol. 72, pp. 263-269, 2002.
- [96] R. Singh, S. Sinha, R. Thakur, and P. Chou, "Some photoeffect roles in rapid isothermal processing," *Applied physics letters*, vol. 58, pp. 1217-1219, 1991.
- [97] B. Hartiti, R. Schindler, A. Slaoui, B. Wagner, J. Muller, I. Reis, *et al.*, "Towards high-efficiency silicon solar cells by rapid thermal processing," *Progress in Photovoltaics: Research and Applications*, vol. 2, pp. 129-142, 1994.
- [98] W. Metzger, D. Albin, M. Romero, P. Dippo, and M. Young, "CdCl₂ treatment, S diffusion, and recombination in polycrystalline CdTe," *Journal of applied physics*, vol. 99, 2006.
- [99] Newport. *Introduction to Solar Radiation*.
- [100] ASTM, "Standard Tables for References Solar Spectral Irradiance at Air Mass 1.5: Direct Normal and Hemispherical for a 37° Tilted Surface (Withdrawn 2005)," ed. <http://www.astm.org/Standards/G159>, 2005.

- [101] <http://www.pveducation.org/pvcdrom/properties-of-sunlight/air-mass>
- [102] https://en.wikipedia.org/wiki/Solar_simulator
- [103] A. Al-Azzawi, *Photonics: principles and practices*: CRC Press, 2006.
- [104] http://users.uj.edu.pl/~ufpostaw/2_Pracownia/S2/monochromator_en.htm
- [105] [https://assets.newport.com/webDocuments-EN/images/Oriel Cornerstone 260 Datasheet.pdf](https://assets.newport.com/webDocuments-EN/images/Oriel_Cornerstone_260_Datasheet.pdf)
- [106] Time Resolved Photoluminescence Spectroscopy (TRPL).
http://www.mpip-mainz.mpg.de/65134/Time_Resolved_Photoluminescence_Spectroscopy
- [107] W. Metzger, R. Ahrenkiel, P. Dippo, J. Geisz, M. Wanlass, and S. Kurtz, "Time-resolved photoluminescence and photovoltaics," in *Department of Energy Solar Energy Technologies Program Review Meeting, Denver, Colorado*, 2004.
- [108] J. Ma, D. Kuciauskas, D. Albin, R. Bhattacharya, M. Reese, T. Barnes, *et al.*, "Dependence of the Minority-Carrier Lifetime on the Stoichiometry of CdTe Using Time-Resolved Photoluminescence and First-Principles Calculations," *Physical Review Letters*, vol. 111, Aug 7 2013.
- [109] J. P. Hofmann, M. Rohnke, and B. M. Weckhuysen, "Recent advances in secondary ion mass spectrometry of solid acid catalysts: large zeolite crystals under bombardment," *Physical Chemistry Chemical Physics*, vol. 16, pp. 5465-5474, 2014 2014.
- [110] D. R. Diercks, J. Li, J. D. Beach, C. A. Wolden, B. P. Gorman, and Ieee, "Atom Probe Tomography for Nanoscale Characterization of CdTe Device Absorber Layers and Interfaces," *2014 Ieee 40th Photovoltaic Specialist Conference (Pvsc)*, pp. 85-89, 2014 2014.
- [111] <http://teaching.shu.ac.uk/hwb/chemistry/tutorials/molspec/lumin3.htm>
- [112] P. Majumder, *Fundamental studies of diffusion for Cu metallization and atomic layer deposited high-k films*, 2008.
- [113] N. K. S. Kumbhat, *Essentials in Nanoscience and Nanotechnology*: John Wiley & Sons, Inc, 2016.
- [114] P. S. M. P. Rani, *Metal and Alloy Bonding: An Experimental Analysis* Springer, 2012.
- [115] <http://pd.chem.ucl.ac.uk/pdnn/inst1/optics1.htm>
- [116] V. K. P. Rutberg, *Pulsed Electrical Discharges for Medicine and Biology: Techniques, Process, Applications*. Springer, 2015.
- [117] <http://emicroscope.blogspot.com/2011/03/scanning-electron-microscope-sem-how-it.html>
- [118] S. Hashmi, *Comprehensive Materials Processing*: Elsevier Science & Technology Books, 2014.

- [119] A. Morte and A. Varma, *Root Engineering: Basic and Applied Concepts*: Springer Berlin Heidelberg, 2014.
- [120] <http://www.mee-inc.com/hamm/scanning-electron-microscopy-sem/>
- [121] First Solar, Key Quarterly Financial Data, Q3, (2013).
- [122] R. Garabedian, First Solar Technology Update, 2014.
- [123] R. Chakrabarti, S. Ghosh, S. Chaudhuri, and A. K. Pal, "Rapid thermal processing for the preparation of CdTe film," *Journal of Physics D-Applied Physics*, vol. 32, pp. 1258-1262, Jun 7 1999.
- [124] T. A. Gessert, W. K. Metzger, P. Dippo, S. E. Asher, R. G. Dhere, and M. R. Young, "Dependence of carrier lifetime on Cu-contacting temperature and ZnTe:Cu thickness in CdS/CdTe thin film solar cells," *Thin Solid Films*, vol. 517, pp. 2370-2373, Feb 2 2009.
- [125] L. Kranz, C. Gretener, J. Perrenoud, R. Schmitt, F. Pianezzi, F. La Mattina, *et al.*, "Doping of polycrystalline CdTe for high-efficiency solar cells on flexible metal foil," *Nature Communications*, vol. 4, Aug 2013.
- [126] V. Komin, V. Viswanathan, B. Tetali, D. L. Morel, C. S. Ferekides, and I. Ieee, *Identification of defect levels in CdTe/CdS solar cells using deep level transient spectroscopy*, 2002.
- [127] F. H. Seymour, V. Kaydanov, T. R. Ohno, and D. Albin, "Cu and CdCl₂ influence on defects detected in CdTe solar cells with admittance spectroscopy," *Applied Physics Letters*, vol. 87, Oct 10 2005.
- [128] C. R. Corwine, A. O. Pudov, M. Gloeckler, S. H. Demtsu, and J. R. Sites, "Copper inclusion and migration from the back contact in CdTe solar cells," *Solar Energy Materials and Solar Cells*, vol. 82, pp. 481-489, May 30 2004.
- [129] J. V. Li, J. N. Duenow, D. Kuciauskas, A. Kanevce, R. G. Dhere, M. R. Young, *et al.*, "Electrical Characterization of Cu Composition Effects in CdS/CdTe Thin-Film Solar Cells with a ZnTe:Cu Back Contact," in *2012 Ieee 38th Photovoltaic Specialists Conference*, ed, 2013.
- [130] W. L. Rance, J. M. Burst, D. M. Meysing, C. A. Wolden, M. O. Reese, T. A. Gessert, *et al.*, "14%-efficient flexible CdTe solar cells on ultra-thin glass substrates," *Applied Physics Letters*, vol. 104, Apr 7 2014.
- [131] J. Perrenoud, B. Schaffner, S. Buecheler, and A. N. Tiwari, "Fabrication of flexible CdTe solar modules with monolithic cell interconnection," *Solar Energy Materials and Solar Cells*, vol. 95, pp. S8-S12, May 2011.
- [132] A. L. Fahrenbruch, "Exploring back contact technology to increase CdS/CdTe solar cell efficiency," in *Thin-Film Compound Semiconductor Photovoltaics - 2007*. vol. 1012, T. Gessert, K. Durose, C. Heske, S. Marsillac, and T. Wada, Eds., ed, 2007, pp. 283-290.
- [133] M. Burgelman, K. Decock, S. Khelifi, and A. Abass, "Advanced electrical simulation

- of thin film solar cells," *Thin Solid Films*, vol. 535, pp. 296-301, May 15 2013.
- [134] A. Kanevce and T. A. Gessert, "Optimizing CdTe Solar Cell Performance: Impact of Variations in Minority-Carrier Lifetime and Carrier Density Profile," *Ieee Journal of Photovoltaics*, vol. 1, pp. 99-103, Jul 2011.
- [135] W. K. Metzger, M. J. Romero, P. Dippo, M. Young, and Ieee, *Characterizing recombination in CdTe solar cells with time-resolved photoluminescence*, 2006.
- [136] J. M. Burst, W. L. Rance, D. M. Meysing, C. A. Wolden, W. K. Metzger, S. M. Garner, *et al.*, "Performance of Transparent Conductors on Flexible Glass and Plastic Substrates for Thin Film Photovoltaics," *2014 Ieee 40th Photovoltaic Specialist Conference (Pvsc)*, pp. 1589-1592, 2014 2014.
- [137] See supplementary material at <http://dx.doi.org/10.1063/1.4916634> for stability data.
- [138] B. J. Simonds, V. Palekis, B. Van Devener, C. Ferekides, and M. A. Scarpulla, "Pulsed laser induced ohmic back contact in CdTe solar cells," *Applied Physics Letters*, vol. 104, Apr 7 2014.
- [139] A. Niemegeers and M. Burgelman, "Effects of the Au/CdTe back contact on IV and CV characteristics of Au/CdTe/CdS/TCO solar cells," *Journal of Applied Physics*, vol. 81, pp. 2881-2886, Mar 15 1997.
- [140] H. C. Chou, A. Rohatgi, N. M. Jokerst, E. W. Thomas, and S. Kamra, "Copper migration in CdTe heterojunction solar cells," *Journal of Electronic Materials*, vol. 25, pp. 1093-1098, Jul 1996.
- [141] T. A. Gessert, A. R. Mason, R. C. Reedy, R. Matson, T. J. Coutts, and P. Sheldon, "DEVELOPMENT OF RF-SPUTTERED, CU-DOPED ZNTE FOR USE AS A CONTACT INTERFACE LAYER TO P-CDTE," *Journal of Electronic Materials*, vol. 24, pp. 1443-1449, Oct 1995.
- [142] N. Strevel, L. Trippel, C. Kotarba, I. Khan, Improvements in CdTe module reliability and long-term degradation through advances in construction and device innovation, *Photovoltaics International* 22 (2014), 66-74.
- [143] H. H. Woodbury, M. Aven, Some diffusion and solubility measurements of Cu in CdTe, *J. Appl. Phys.* 39 (1968), 5485-5487.
- [144] E. D. Jones, N. M. Stewart, and J. B. Mullin, "THE DIFFUSION OF COPPER IN CADMIUM TELLURIDE," *Journal of Crystal Growth*, vol. 117, pp. 244-248, Feb 1992.
- [145] J. D. Poplawsky, N. R. Paudel, C. Li, C. M. Parish, D. Leonard, Y. Yan, *et al.*, "Direct Imaging of Cl- and Cu-Induced Short-Circuit Efficiency Changes in CdTe Solar Cells," *Advanced Energy Materials*, vol. 4, Oct 28 2014.
- [146] H. H. Woodbury, M. Aven, Some diffusion and solubility measurements of Cu in CdTe, *J. Appl. Phys.* 39 (1968), 5485-5487.
- [147] G. Teeter, S. Asher, and Ieee, "MODELING Cu MIGRATION IN CdTe SOLAR CELLS UNDER DEVICE-PROCESSING AND LONG-TERM STABILITY

- CONDITIONS," in *Pvsc: 2008 33rd Ieee Photovoltaic Specialists Conference, Vols 1-4*, ed, 2008, pp. 302-307.
- [148] D. M. Meysing, M. M. Griffith, W. L. Rance, M. O. Reese, J. M. Burst, C. A. Wolden, *et al.*, "Properties of Oxygenated Cadmium Sulfide (CdS:O) and Their Impact on CdTe Device Performance," *2014 Ieee 40th Photovoltaic Specialist Conference (Pvsc)*, pp. 964-967, 2014 2014.
- [149] B. Gorman, D. Diercks, N. Salmon, E. Stach, G. Amador, and C. Hartfield, "Hardware and techniques for cross-correlative TEM and atom probe analysis," *Microscopy Today*, vol. 16, pp. 42-47, 2008.
- [150] X. Wu, J. Zhou, A. Duda, Y. Yan, G. Teeter, S. Asher, *et al.*, "Phase control of CuxTe film and its effects on CdS/CdTe solar cell," *Thin Solid Films*, vol. 515, pp. 5798-5803, May 31 2007.
- [151] J. V. Li, A. F. Halverson, O. V. Sulima, S. Bansal, J. M. Burst, T. M. Barnes, *et al.*, "Theoretical analysis of effects of deep level, back contact, and absorber thickness on capacitance-voltage profiling of CdTe thin-film solar cells," *Solar Energy Materials and Solar Cells*, vol. 100, pp. 126-131, May 2012.
- [152] W. K. Metzger, D. Albin, D. Levi, P. Sheldon, X. Li, B. M. Keyes, *et al.*, "Time-resolved photoluminescence studies of CdTe solar cells," *Journal of Applied Physics*, vol. 94, pp. 3549-3555, Sep 1 2003.
- [153] D. Kuciauskas, A. Kanevce, J. M. Burst, J. N. Duenow, R. Dhere, D. S. Albin, *et al.*, "Minority Carrier Lifetime Analysis in the Bulk of Thin-Film Absorbers Using Subbandgap (Two-Photon) Excitation," *Ieee Journal of Photovoltaics*, vol. 3, pp. 1319-1324, Oct 2013.
- [154] H. Woodbury and M. Aven, "Some diffusion and solubility measurements of Cu in CdTe," *Journal of Applied Physics*, vol. 39, pp. 5485-5488, 1968.
- [155] N. Strevel, L. Trippel, C. Kotarba, I. Khan, "Improvements in CdTe module reliability and long-term degradation through advances in construction and device innovation," *Photovoltaics International* 22 (2014), 66-74.
- [156] P.-P. Choi, O. Cojocar-Mirédin, D. Abou-Ras, R. Caballero, D. Raabe, V. S. Smentkowski, *et al.*, "Atom probe tomography of compound semiconductors for photovoltaic and light-emitting device applications," *Microscopy Today*, vol. 20, pp. 18-24, 2012.
- [157] L. Kranz, C. Gretener, J. Perrenoud, D. Jaeger, S. S. A. Gerstl, R. Schmitt, *et al.*, "Tailoring Impurity Distribution in Polycrystalline CdTe Solar Cells for Enhanced Minority Carrier Lifetime," *Advanced Energy Materials*, vol. 4, May 2014.
- [158] B. Spath, J. Fritsche, F. Sauberlich, A. Klein, and W. Jaegermann, "Studies of sputtered ZnTe films as interlayer for the CdTe thin film solar cell," *Thin Solid Films*, vol. 480, pp. 204-207, Jun 1 2005.
- [159] T. M. Barnes, W. L. Rance, J. M. Burst, M. O. Reese, D. M. Meysing, C. A. Wolden, *et al.*, "High-Efficiency Flexible CdTe Superstrate Devices," *2014 Ieee 40th*

- Photovoltaic Specialist Conference (Pvsc)*, pp. 2289-2292, 2014 2014.
- [160] C. W. Warren, J. Li, C. A. Wolden, D. M. Meysing, T. M. Barnes, D. W. Miller, *et al.*, "The effect of copper on the sub-bandgap density of states of CdTe solar cells," *Applied Physics Letters*, vol. 106, May 18 2015.
- [161] N. Strevel, L. Trippel, C. Kotarba, I. Khan, Improvements in CdTe module reliability and long-term degradation through advances in construction and device innovation, *Photovoltaics International* 22 (2014), 66-74.
- [162] H. P. Mahabaduge, W. L. Rance, J. M. Burst, M. O. Reese, D. M. Meysing, C. A. Wolden, *et al.*, "High-efficiency, flexible CdTe solar cells on ultra-thin glass substrates," *Applied Physics Letters*, vol. 106, Mar 30 2015.
- [163] S. S. Hegedus and B. E. McCandless, "CdTe contacts for CdTe/CdS solar cells: effect of Cu thickness, surface preparation and recontacting on device performance and stability," *Solar Energy Materials and Solar Cells*, vol. 88, pp. 75-95, Jun 15 2005.
- [164] Y. Yan, D. Albin, and M. M. Al-Jassim, "Do grain boundaries assist S diffusion in polycrystalline CdS/CdTe heterojunctions?," *Applied Physics Letters*, vol. 78, pp. 171-173, Jan 8 2001.
- [165] D. S. Albin, Y. Yan, and M. M. Al-Jassim, "The effect of oxygen on interface microstructure evolution in the CdS/CdTe solar cells," *Progress in Photovoltaics*, vol. 10, pp. 309-322, Aug 2002.
- [166] A. Abbas, G. D. West, J. W. Bowers, P. M. Kaminski, B. Maniscalco, J. M. Walls, *et al.*, "Cadmium Chloride Assisted Re-Crystallization of CdTe: The effect of annealing over-treatment," *2014 Ieee 40th Photovoltaic Specialist Conference (Pvsc)*, pp. 701-706, 2014 2014.
- [167] A. Abbas, D. Meysing, J. Li, J. Beach, T. Barnes, J. Walls, *et al.*, "Structural and chemical characterization of the back contact region in high efficiency CdTe solar cells," in *Photovoltaic Specialist Conference (PVSC), 2015 IEEE 42nd*, 2015, pp. 1-6.
- [168] G. Teeter, "Cu₂Te synthesis and in-vacuum thermal decomposition: Chemical-kinetics analysis and comparison to equilibrium vapor-pressure measurements," *Thin Solid Films*, vol. 515, pp. 7886-7891, Jul 31 2007.
- [169] G. Luo, B. Lv, W. Li, L. Feng, J. Zhang, L. Wu, *et al.*, "Characterization of Cu_{1.4}Te Thin Films for CdTe Solar Cells," *International Journal of Photoenergy*, 2014 2014.
- [170] B. E. McCandless, S. S. Hegedus, R. W. Birkmire, and D. Cunningham, "Correlation of surface phases with electrical behavior in thin-film CdTe devices," *Thin Solid Films*, vol. 431, pp. 249-256, May 1 2003.
- [171] A. S. Pashinkin and V. A. Fedorov, "Phase equilibria in the Cu-Te system," *Inorganic Materials*, vol. 39, pp. 539-554, Jun 2003.
- [172] D. Bonnet, "THE CdTe THIN FILM SOLAR CELL - AN OVERVIEW," *International Journal of Solar Energy*, vol. 12, pp. 1-14, Jan 1 1992.
- [173] J. H. Yun, K. H. Kim, D. Y. Lee, and B. T. Ahn, "Back contact formation

- using Cu(2)Te as a Cu-doping source and as an electrode in CdTe solar cells," *Solar Energy Materials and Solar Cells*, vol. 75, pp. 203-210, Jan 2003.
- [174] N. Strevel et al., "Improvements in CdTe module reliability and long-term degradation through advances in construction and device innovation," *Photovoltaic international*, vol. 22, 2014.
- [175] C. A. Wolden, A. Abbas, J. Li, D. R. Diercks, D. M. Meysing, T. R. Ohno, *et al.*, "The roles of ZnTe buffer layers on CdTe solar cell performance," *Solar Energy Materials and Solar Cells*, vol. 147, pp. 203-210, 2016.
- [176] D. L. Batzner, A. Romeo, H. Zogg, R. Wendt, and A. N. Tiwari, "Development of efficient and stable back contacts on CdTe/CdS solar cells," *Thin Solid Films*, vol. 387, pp. 151-154, May 29 2001.
- [177] K. Tu and B. Berry, "X-ray study of interdiffusion in bimetallic Cu–Au films," *Journal of Applied Physics*, vol. 43, pp. 3283-3290, 1972.
- [178] J. Murray, "The Cu– Ti (Copper-Titanium) system," *Bulletin of alloy phase diagrams*, vol. 4, pp. 81-95, 1983.
- [179] J. F. Hiltner and J. R. Sites, "Stability of CdTe solar cells at elevated temperatures: Bias, temperature, and Cu dependence," in *Ncpv Photovoltaics Program Review: Proceedings of the 15th Conference*. vol. 462, M. AlJassim and J. P. Thornton, Eds., ed, 1999, pp. 170-175.
- [180] I. Visoly-Fisher, K. D. Dobson, J. Nair, E. Bezael, G. Hodes, and D. Cahen, "Factors affecting the stability of CdTe/CdS solar cells deduced from stress tests at elevated temperature," *Advanced Functional Materials*, vol. 13, pp. 289-299, 2003.
- [181] X. Wu, J. Zhou, A. Duda, Y. Yan, G. Teeter, S. Asher, *et al.*, "Phase control of Cu_xTe film and its effects on CdS/CdTe solar cell," *Thin Solid Films*, vol. 515, pp. 5798-5803, 2007.
- [182] S. S. Hegedus, B. E. McCandless, and R. W. Birkmire, "Analysis of stress-induced degradation in CdS/CdTe solar cells," in *Photovoltaic Specialists Conference, 2000. Conference Record of the Twenty-Eighth IEEE, 2000*, pp. 535-538.
- [183] T. L. Chu and S. S. Chu, "Recent progress in thin-film cadmium telluride solar cells," *Progress in photovoltaics: Research and Applications*, vol. 1, pp. 31-42, 1993.
- [184] B. McCandless and S. Hegedus, "Influence of CdS window layers on thin film CdS/CdTe solar cell performance," in *Photovoltaic Specialists Conference, 1991., Conference Record of the Twenty Second IEEE, 1991*, pp. 967-972.
- [185] E. Jones, V. Barrioz, S. Irvine, and D. Lamb, "Towards ultra-thin CdTe solar cells using MOCVD," *Thin Solid Films*, vol. 517, pp. 2226-2230, 2009.
- [186] K. Premaratne, S. Akuranthilaka, I. Dharmadasa, and A. Samantilleka, "Electrodeposition using non-aqueous solutions at 170° C and characterisation of CdS, CdS x Se (1– x) and CdSe compounds for use in graded band gap solar cells," *Renewable energy*, vol. 29, pp. 549-557, 2004.

- [187] X. Wu, R. Dhere, Y. Yan, M. Romero, Y. Zhang, J. Zhou, *et al.*, "High-efficiency polycrystalline CdTe thin-film solar cells with an oxygenated amorphous CdS (a-CdS:O) window layer," in *Photovoltaic Specialists Conference, 2002. Conference Record of the Twenty-Ninth IEEE*, 2002, pp. 531-534.
- [188] X. Wu, Y. Yan, R. Dhere, Y. Zhang, J. Zhou, C. Perkins, *et al.*, "Nanostructured CdS:O film: preparation, properties, and application," *physica status solidi (c)*, vol. 1, pp. 1062-1066, 2004.
- [189] N. R. Paudel and Y. Yan, "Fabrication and characterization of high-efficiency CdTe-based thin-film solar cells on commercial SnO₂:F-coated soda-lime glass substrates," *Thin Solid Films*, vol. 549, pp. 30-35, 2013.
- [190] J. M. Kephart, R. M. Geisthardt, and W. Sampath, "Optimization of CdTe thin-film solar cell efficiency using a sputtered, oxygenated CdS window layer," *Progress in Photovoltaics: Research and Applications*, vol. 23, pp. 1484-1492, 2015.
- [191] D. A. Duncan, J. M. Kephart, K. Horsley, M. Blum, M. Mezher, L. Weinhardt, *et al.*, "Characterization of sulfur bonding in CdS:O buffer layers for CdTe-based thin-film solar cells," *ACS applied materials & interfaces*, vol. 7, pp. 16382-16386, 2015.
- [192] N. R. Paudel, C. R. Grice, C. Xiao, and Y. Yan, "The effects of high temperature processing on the structural and optical properties of oxygenated CdS window layers in CdTe solar cells," *Journal of Applied Physics*, vol. 116, p. 044506, 2014.
- [193] D. Meysing, M. Reese, H. Mahabaduge, W. Metzger, J. Burst, J. Duenow, *et al.*, "Chemical and mechanical techniques enabling direct characterization of the CdS/CdTe heterojunction region in completed devices," in *Photovoltaic Specialist Conference (PVSC), 2015 IEEE 42nd*, 2015, pp. 1-6.
- [194] D. M. Meysing, "Development of ternary oxides for use in advanced front contacts in cadmium telluride solar cells by magnetron sputtering," Colorado School of Mines, 2015.
- [195] M. Herndon, A. Gupta, V. Kaydanov, and R. Collins, "Evidence for grain-boundary-assisted diffusion of sulfur in polycrystalline CdS/CdTe heterojunctions," *Applied physics letters*, vol. 75, pp. 3503-3505, 1999.
- [196] R. Dhere, Y. Zhang, M. Romero, S. Asher, M. Young, B. To, *et al.*, "Investigation of junction properties of CdS/CdTe solar cells and their correlation to device properties," in *Photovoltaic Specialists Conference, 2008. PVSC'08. 33rd IEEE*, 2008, pp. 1-5.
- [197] R. Dhere, D. Albin, D. Rose, S. Asher, K. Jones, M. Al-Jassim, *et al.*, "Intermixing at the CdS/CdTe interface and its effect on device performance," in *MRS Proceedings*, 1996, p. 361.
- [198] B. McCandless, L. Moulton, and R. Birkmire, "Recrystallization and sulfur diffusion in CdCl₂-treated CdTe/CdS thin films," *Progress in photovoltaics: Research and Applications*, vol. 5, pp. 249-260, 1997.
- [199] D. Lane, "A review of the optical band gap of thin film CdS_xTe 1-x," *Solar energy materials and solar cells*, vol. 90, pp. 1169-1175, 2006.

- [200] B. E. McCandless and R. W. Birkmire, "CdTe 1-x S x absorber layers for thin-film CdTe/CdS solar cells," in *Photovoltaic Specialists Conference, 1997., Conference Record of the Twenty-Sixth IEEE, 1997*, pp. 307-312.
- [201] J. N. Duenow, R. G. Dhere, H. R. Moutinho, B. To, J. W. Pankow, D. Kuciauskas, *et al.*, "CdS/CdTe solar cells containing directly-deposited CdS x Te 1- x alloy layers," in *Photovoltaic Specialists Conference (PVSC), 2011 37th IEEE, 2011*, pp. 000348-000353.
- [202] J. Mangalhara, R. Thangaraj, and O. Agnihotri, "Structural, optical and photoluminescence properties of electron beam evaporated CdSe1- xTex films," *Solar energy materials*, vol. 19, pp. 157-165, 1989.
- [203] P. More, G. Shahane, L. Deshmukh, and P. Bhosale, "Spectro-structural characterisation of CdSe 1- x Te x alloyed thin films," *Materials chemistry and physics*, vol. 80, pp. 48-54, 2003.
- [204] I. Tao, M. Jurkovic, and W. Wang, "Doping of ZnTe by molecular beam epitaxy," *Applied physics letters*, vol. 64, pp. 1848-1849, 1994.
- [205] B. Späth, J. Fritsche, A. Klein, and W. Jaegermann, "Nitrogen doping of ZnTe and its influence on CdTe/ZnTe interfaces," *Applied physics letters*, vol. 90, p. 2112, 2007.
- [206] B. L. Crowder and W. N. Hammer, "Shallow acceptor states in ZnTe and CdTe," *Physical Review*, vol. 150, p. 541, 1966.
- [207] Y. Hishida, H. Ishii, T. Toda, and T. Niina, "Growth and characterization of MBE-grown ZnTe: P," *Journal of Crystal Growth*, vol. 95, pp. 517-521, 1989.
- [208] J. N. D. James M Burst, Jeff A Aguiar, Helio Moutinho, Chun-Sheng Jiang, Mowafak Al Jassim, Matthew O Reese, David S Albin, Eric Colegrove, Tursun Ablekim, Santosh K Swain, Kelvin G Lynn, Darius Kuciauskas, Wyatt K Metzger, "Interface Characterization of Single-Crystal CdTe Solar Cells with VOC > 900mV," *43rd IEEE Photovoltaic Specialists Conference, 2016*.

APPENDIX A
SECONDARY AUTHOR CONTRIBUTIONS

I was a co-author on the following peer-reviewed journal articles. Here I provide the citations and a brief description of my contribution to these efforts.

- 1) David R. Diercks, **Jiaojiao Li**, Joseph D. Beach, Colin A. Wolden, and Brian P. Gorman. "Atom probe tomography for nanoscale characterization of CdTe device absorber layers and interfaces." In Photovoltaic Specialist Conference (PVSC), 2014 IEEE 40th, pp. 0085-0089. IEEE, 2014.

This article showcases using APT technique to characterize the nanoscale structure of CdTe devices. . My contribution was to fabricate the devices used in the study.

- 2) Charles W Warren, **Jiaojiao Li**, Colin A. Wolden, Daniel M. Meysing, Teresa M. Barnes, D. Westley Miller, Jennifer T. Heath, and Mark C. Lonergan. "The effect of copper on the sub-bandgap density of states of CdTe solar cells." Applied Physics Letters 106, no. 20 (2015): 203903.

This article reports the optical transitions in CdTe devices using photocapacitance and photocurrent techniques. My contribution was to provide the devices used in the study.

- 3) A. Abbas, D. M. Meysing, **Jiaojiao. Li**, J. D. Beach, T. M. Barnes, J. M. Walls, and C. A. Wolden. "Structural and chemical characterization of the back contact region in high efficiency CdTe solar cells." In Photovoltaic Specialist Conference (PVSC), 2015 IEEE 42nd, pp. 1-6. IEEE, 2015.

This article reports the characterization of the ZnTe:Cu back contact of CdTe devices using HRTEM techniques. My contribution was to provide the devices used in the study.

APPENDIX B

PERMISSIONS

This appendix contains permissions from publishers and co-authors to use previously published material in this thesis.

B.1 Permission from Elsevier

This is a License Agreement between Jiaojiao Li ("You") and Elsevier ("Elsevier") provided by Copyright Clearance Center ("CCC"). The license consists of your order details, the terms and conditions provided by Elsevier, and the payment terms and conditions.

Supplier	Elsevier Limited The Boulevard, Langford Lane Kidlington, Oxford, OX5 1GB, UK
Registered Company Number	1982084
Customer name	Jiaojiao Li
Customer address	1408 Ulysses St. Apt 4 GOLDEN, CO 80401
License number	3692670738342
License date	Aug 19, 2015
Licensed content publisher	Elsevier
Licensed content publication	Solar Energy Materials and Solar Cells
Licensed content title	Controlled activation of ZnTe:Cu contacted CdTe solar cells using rapid thermal processing
Licensed content author	Jiaojiao Li, David R. Diercks, Timothy R. Ohno, Charles W. Warren, Mark C. Lonergan, Joseph D. Beach, Colin A. Wolden
Licensed content date	February 2015
Licensed content volume number	133
Licensed content issue number	n/a
Number of pages	8
Start Page	208
End Page	215
Type of Use	reuse in a thesis/dissertation
Intended publisher of new work	other
Portion	full article
Format	both print and electronic
Are you the author of this Elsevier article?	Yes

Will you be translating?	No
Title of your thesis/dissertation	Development of ZnTe:Cu contacted CdTe solar cells.
Expected completion date	April 2016
Estimated size (number of pages)	140
Elsevier VAT number	GB 494 6272 12
Permissions price	0.00 USD
VAT/Local Sales Tax	0.00 USD / 0.00 GBP
Total	0.00 USD

B.2 Permission from Elsevier

Supplier	Elsevier Limited The Boulevard, Langford Lane Kidlington, Oxford, OX5 1GB, UK
Registered Company Number	1982084
Customer name	Jiaojiao Li
Customer address	1408 Ulysses St. Apt 4 GOLDEN, CO 80401
License number	3692670738342
License date	Aug 19, 2015
Licensed content publisher	Elsevier
Licensed content publication	Solar Energy Materials and Solar Cells
Licensed content title	The roles of ZnTe buffer layers on CdTe solar cell performance
Licensed content author	Colin A. Wolden, Ali Abbas, Jiaojiao Li, David R. Diercks, Daniel M. Meysing, Timothy R. Ohno, Joseph D. Beach, Teresa M. Barnes, John M. Walls
Licensed content date	April 2016
Licensed content volume number	147
Licensed content issue number	n/a
Number of pages	8
Start Page	203
End Page	210
Type of Use	reuse in a thesis/dissertation
Intended publisher of new work	other
Portion	full article
Format	both print and electronic
Are you the author of this Elsevier article?	Yes
Will you be translating?	No
Title of your thesis/dissertation	Development of ZnTe:Cu contacted CdTe solar cells.
Expected completion date	April 2016
Estimated size (number of pages)	140
Elsevier VAT number	GB 494 6272 12

Permissions price	0.00 USD
VAT/Local Sales Tax	0.00 USD / 0.00 GBP
Total	0.00 USD

B.3 Permission from IEEE

The IEEE does not require individuals working on a thesis to obtain a formal reuse license, however, you may print out this statement to be used as a permission grant:

Requirements to be followed when using any portion (e.g., figure, graph, table, or textual material) of an IEEE copyrighted paper in a thesis:

- 1) In the case of textual material (e.g., using short quotes or referring to the work within these papers) users must give full credit to the original source (author, paper, publication) followed by the IEEE copyright line © 2011 IEEE.
- 2) In the case of illustrations or tabular material, we require that the copyright line © [Year of original publication] IEEE appear prominently with each reprinted figure and/or table.
- 3) If a substantial portion of the original paper is to be used, and if you are not the senior author, also obtain the senior author's approval.

Requirements to be followed when using an entire IEEE copyrighted paper in a thesis:

- 1) The following IEEE copyright/ credit notice should be placed prominently in the references: © [year of original publication] IEEE. Reprinted, with permission, from [author names, paper title, IEEE publication title, and month/year of publication]
- 2) Only the accepted version of an IEEE copyrighted paper can be used when posting the paper or your thesis on-line.
- 3) In placing the thesis on the author's university website, please display the following message in a prominent place on the website: In reference to IEEE copyrighted material which is used with permission in this thesis, the IEEE does not endorse any of [university/educational entity's name goes here]'s products or services. Internal or personal use of this material is permitted. If interested in reprinting/republishing IEEE copyrighted

material for advertising or promotional purposes or for creating new collective works for resale or redistribution, please go to http://www.ieee.org/publications_standards/publications/rights/rights_link.html to learn how to obtain a License from RightsLink.

If applicable, University Microfilms and/or ProQuest Library, or the Archives of Canada may supply single copies of the dissertation.